# Study for the physical properties of active galactic nucleus jets by radio imaging analyses of jet structure from Schwarzschild-radius to galactic scales

NAKAHARA SATOMI

Doctor of Philosophy

Department of Space and Astronautical Science
School of Physical Sciences
SOKENDAI (The Graduate University for Advanced Studies)

# Study for the physical properties of active galactic nucleus jets by radio imaging analyses of jet structure from Schwarzschild-radius to galactic scales

Satomi Nakahara

Department of Space and Astronautical Science,
The Graduate University for Advanced Studies

# Abstract

Relativistic jets are ubiquitous in mass accreting black hole systems, including active galactic nuclei (AGNs) having supermassive black holes at the center of galaxy. However, its collimation and acceleration mechanisms are big challenges that have not been solved for many years in the research field of astrophysical jets. The present study approaches the unsolved problem by imaging analysis techniques to measure the radial profiles of jet width throughout the physical scales beyond the sphere of gravitational influence of the central black holes (typically $\sim 10^5$ Schwarzschild radii ($R_{\rm S}$) as Bondi radii) from the Schwarzschild scale for several AGNs. Recently, the evidence for the relationship between the bulk acceleration and geometrical collimation in the M87 jet has been observationally obtained (Asada et al. 2014); the region at which the jet acceleration is observed coincides with that at the jet is collimated into a parabolic streamline up to the Bondi radius from the central black hole (Asada & Nakamura 2012). The transition from the parabolic to the conical expansions in the jet occurs at $\sim 10^5$ times the $R_{\rm S}$. Subsequently, the similar radial profile of jet width has been found in the NGC 6251 jet (Tseng et al. 2016). Such a phenomenon is successfully explained by theoretical studies via general relativistic magnetohydrodynamics (MHD) simulations (e.g., McKinney 2006); In order to maintain a parabolic shape, a transverse pressure from the external medium with relatively shallow radial dependence (e.g., Komissarov et al. 2009) is required. However, there have been only two observational examples for established parabolic-to-conical profiles in jet width (M87 and NGC 6251).

The present study provides three more AGNs whose jet widths have been measured throughout physical scales comparable with those of the two AGNs by the previous studies. NGC 4261, NGC 1052, and Cygnus A are newly investigated at very wide scale in radial distance from the central engine. These radio galaxies are located at relatively nearby universe, and have very high-mass black hole. Therefore, geometrical investigations in a unit of $R_{\rm S}$ can be advantageously promoted in these radio galaxies. They have characteristics that differ from the M87 and NGC 6251; NGC 4261, NGC 1052, and Cygnus A have two-sided jets due to highly inclined jets with large inclination angles. These three contribute to expand the parameter space by adding

the variety of inclination angle and symmetry. Furthermore, a Fanaroff–Riley Class II (FR-II) radio galaxy was investigated for the first time with Cygnus A.

I performed a pixel-based analysis on the total intensity maps of interferometric images at many frequencies and various angular scales, to measure the jet width in the both approaching and counter sides of the three AGNs. The intensity of jets was sliced transversely at a sampling rate of one-fifth of the synthesized beam size, and then, a Gaussian fitting to derive a deconvolved width of the jet is performed. Furthermore, the present study will attempt a pixel-based analysis along the jet axis for one AGN on the single side (NGC 4261 on the approaching side). In this context, the measurement of jet width has an implication to obtain the volume of jets; at the same time the analyzing of intensity along jets is to obtain the intensity of radiation emitted from the volume. Combining the two above observables is to estimate synchrotron luminosity related to internal energy, magnetic field, and jet pressure in jets.

I illustrate here comprehensive picture of jet evolution over $10^1$–$10^9 R_{\rm S}$ on the basis of the three nearby AGNs (NGC 4261, NGC 1052, and Cygnus A) that were investigated by the present study in addition to M87 and NGC 6251 that were reported by the previous studies by the other authors.

Transitions from parabolic to conical streamlines of jets were found in all the four FR I. This discovery suggests that the jet acceleration mechanism by collimation plays a universal role in FR-I AGNs. However, note that the transition in the NGC 4261 jet was found at $\sim 10^4 R_{\rm S}$, which does not coincide with the Bondi radius, unlike the cases of M87 and NGC 6251. To establish the theoretical picture for magnetized jets collimated by external pressure, the radial profile of pressure distribution in the core region of host galaxy should be estimated more precisely on the basis of higher angular resolutions in X-rays.

One FR-II AGN was included in the sample, and showed a unique property in the jet width profile. No transition was found throughout the radial distances ranging from $\sim 10^3$ to $10^9 R_{\rm S}$. A parabolic shape maintains up to this large scale. It is noteworthy that an apparent discontinuity in jet width, showing a jump roughly one order of magnitude. The location of the discontinuity coincides with the boundary of VLBI observational scale and VLA one. This surprising property can be explained by the combination of Doppler-debeaming effect and the limited sensitivities of telescopes in the framework of the multi-layered structure in a stratified jet scenario for this highly inclined AGN.

The framework of the stratified jet can also understand another discovery that the scale factor of jet width among AGNs is apparently correlated with inclination angle. Doppler-beaming/debeaming effect can explain well this phenomenon if the high-brightness inner layers are accelerated in streamlines and dominated by outer layer flows, which are slower and not so deboosted. Degree of this effect is primarily determined by viewing angle of jets. I consider it is a reason why the jet widths of NGC 4261, NGC 1052, and Cygnus A are globally wider than those of M87 and NGC 6251.

The present study additionally focused on counter jets by adding AGNs with two-sided jets to the sample for the first time. Almost perfect symmetry in terms of the radial profiles of jet width has been confirmed for all the two-sided AGN sample, which consists of NGC 4261, NGC 1052, and Cygnus A. This property suggests a universal mechanism in which the collimation and expansion of the magnetized jet is globally regulated by the pressure profile in the host galaxies and intragalactic medium (the intragalactic medium is the hot, X-ray emitting gas that spreads through the space between galaxies). To verify the universality, a larger number of sample is required to investigate.

As a new attempt in this field of research, in this PhD thesis I estimated the development of physical parameters over a very wide range in the NGC 4261 jet. This estimation was made possible by combining the measurement of radiation profile with that of jet width profile. The radial profile of radiation along the jet shows two transitions at $\sim 10^6 R_\mathrm{S}$ and $10^4 R_\mathrm{S}$; the former one coincides with the transition found in the jet-width profile. Under the assumption of equipartition condition in synchrotron plasma, I showed the physical jet conditions in terms of synchrotron luminosity per unit volume (synchrotron emissivity), synchrotron luminosity per unit length, strength of magnetic field, jet pressure, and magnetic energy per unit length. I found that the magnetic energy in the jet was consumed through parabolic and conical streamlines (in which the magnetic energy is probably used for jet bulk acceleration); subsequently, the kinetic energy of the accelerated jet was converted again to the magnetic and particle energies (presumably by deceleration in the jet flow) at the kpc scale and dissipated as synchrotron radiation. The jet's magnetic pressure is eventually consistent with the ambient pressure of intragalactic medium at a large scale. The detailed investigation for the NGC 4261 jet provides us more comprehensive understanding of the physical evolution of jets throughout from the Schwartzschild scale to the intragalactic scale.

Through this research, two important findings have also been obtained as bi-products. From the measurement of jet-width radial profile in NGC 1052, interstellar broadening that is frequency-dependent effect due to radio scattering by ionized gas intervening our line of sight was discovered as the first example of a phenomenon associated with a supermassive black hole system other than the our Galactic center Sgr A*. Moreover, an over-collation on jets is found at the innermost region of NGC 1052. A relatively flat profile is reminiscent of that observed in the jet-width radial profile of very young radio galaxy 3C 84 (Nagai et al. 2014), although the measurement for 3C 84 was limited to the range of $\sim 10^4$–$10^5 R_\mathrm{S}$. The common property of NGC 1052 and 3C 84 as AGNs is that the nucleus is surrounded by the pc-scale plasma torus/disk causing strong free–free absorption. The over-collimations in NGC 1052 could be responsible for the ambient pressure gradient with a significantly shallower profile.

# Contents

# List of Figures

# List of Tables

# Chapter 1

# Introduction: Studies for the collimation and acceleration of astrophysical Jets

## 1.1 The general properties of observed AGN jets

At the center of galaxy, there is a compact area of high activity that can not be explained even considering the celestial activities of all the stars in the galaxy. This central region is called Active Galactic Nuclei (AGN), and galaxies with such a central nuclei is called active galaxies. Active galaxies are considered to be the most active stage in the galaxy's lifecycle, and the central nucleus is from a region smaller than 1 pc from the center of the galaxy in a relatively short period ($\sim 10^8$ years) It radiates enormous energy of $10^{38}$–$10^{48}$ erg sec$^{-1}$. The huge radiation from AGN, which is continuous wave from radio to $\gamma$-ray, is considered to be due to the release of the gravitational energy of the gas descending to the central super massive black hole (SMBH, $\sim 10^8$–$10^9$ $M_\odot$); the accretion matters are forming accretion disk around the central SMBH; while, there is a structure called a jet which is formed by a plasma gas escaping into outer space from the central black hole with relativistic velocity; and some jets also forms a radio lobe at the downstream. AGN Jet has been kept on attention since its existence was discovered, and actively studied from both viewpoints of observation and theory. However, there are still some opening questions that have not been resolved yet. This section introduces the unresolved issues of the AGN jet and what has been studied so far to solve them.

### 1.1.1 Unresolved issues on AGN jet formation

The first unresolved problem on AGN jets is the bulk acceleration. From the many radio imaging observations, collimated jet is formed near central black holes and accelerates up to Lorentz factors of $\Gamma \sim 50$ at maximum. This is a big challenge from the theoretical point of view, because most of energy remains in Poynting energy (magnetic energy) and bulk acceleration need take longer time due to slow acceleration efficiency. Therefore rapid energy conversion, i.e., dissipation, should be required.

The second unresolved problem on AGN jets is the jet collimation. The opening angle derived for the well-collimated jets in Cygnus A is only $\sim 1.6$ deg at kpc-scales (Carilli & Barthel 1996). However, how the jets produce the observed emission and maintain the propagation for many orders of magnitude in distance without being disrupted are not theoretically understood. Some support mechanism is required to maintain such a converged structure.

The third unresolved problem on AGN jets is the jet driving source. The controversy as to whether the driving source of the jet is a black hole (spin) or an accretion disk has been opened. Observational evidence for the jet production mechanisms in AGNs is still unclear. The Blandford–Znajek (BZ) mechanism (Blandford & Znajek 1977) is one of the plausible explanations for the powerful jet launch; jets are launched and powered by rotating black holes immersed in externally supported magnetic fields in this theory.

### 1.1.2 Acceleration of jet

It has been found that nearly half the blobs and 3/4 of the jets exhibit significant changes in speed and/or direction, on the basis of the acceleration properties of 329 features in 95 blazar jets from the Monitoring Of Jets in Active galactic nuclei with VLBA Experiments (the MOJAVE project). The accelerations tend to increase the speed near the cores at the distances of $\sim$ 10–20 pc or less in projection, and decrease their speed at longer distances (Homan et al. 2015). Thus, the bulk acceleration of the jet is commonly seen in blazers.

On the other hand, in nearby radio galaxies the detections of jet proper motion showing acceleration profile along jets have been reported by very intensive VLBI monitoring observations. For Cygnus A, the evolution of bulk acceleration depending on radial distances from the nucleus has been observed by Krichbaum et al. (1998); Bach et al. (2002) from proper motion measurements; counter jets also shows a possible gradual acceleration depending on the radial distance. An emergence of new component associated with $\gamma$-ray event in 3C 84 exhibited the apparent speed with a moderate acceleration from $0.10c$ to $0.47c$, which was still sub-relativistic (Suzuki et al. 2012). For M87, Asada et al. (2014) demonstrated the velocity field with a function of radial distance from the nucleus; the bulk acceleration of the jet (Nakamura & Asada 2013; Mertens et al. 2016; Hada et al. 2017) is occurring up to the order of 100 pc and deceleration has subsequently been shown in the downstream (Biretta et al. 1999; Meyer et al. 2013). However, the acceleration mechanism of relativistic jets in AGNs has still been an unresolved problem in astrophysics. With regard to nearby galaxies, although there is an advantage that very detailed research can be carried out by accumulating observation data with highly resolved images, there is a disadvantage that the number of targets is small.

### 1.1.3 Relation between acceleration and structure of jet

There have been some progresses from recent observational studies on nearby AGN jets. In the radio galaxy M87, Asada & Nakamura (2012) discovered an enduring parabolic jet structure between a few hundred and $10^5$ Schwarzschild radii ($R_{\rm S}$) from the central engine as well as a transition into a conical streamline above $\sim 10^6$ $R_{\rm S}$. Because the transition site is found near the Bondi radius[1] of M87, the possibility of a physical relation between jet confinement and a change radial profile of the ambient pressure has been discussed. Hada et al. (2013) found a possible change in the jet collimation shape in the vicinity of the central black hole of M87, that is potentially related to a magnetic collimation process and/or interactions with the surrounding gas at the jet base. It has subsequently been confirmed that the site at which the bulk acceleration of the jet (Mertens et al. 2016) is occurring corresponds to the region in which the jet width evolves into a parabolic shape, and deceleration (Biretta et al. 1999; Meyer et al. 2013) has been found in the conical downstream (Asada et al. 2014, see also Nakamura & Asada 2013; Hada et al. 2017). The observational evidence for the direct relation between the collimation and the bulk acceleration of jets was made possible by: (i) intensive monitoring of jet proper motion; (ii) spatial resolving in the direction of jet width over a wide range of physical scales in both the parabolic and conical regions, in conjunction with; (iii) precise determination of the central engine location from very-long-baseline interferometry (VLBI) observations toward M87, which is one of the nearest radio galaxies. The position of the central engine of M87 has been successfully determined by measuring frequency-dependent shifts of the core position (Konigl 1981; Lobanov 1998) using multi-frequency phase-referencing VLBI observations (Hada et al. 2011).

To determine whether the transition from parabolic (accelerating) to conical (decelerating) regions is universal phenomena among AGN jets, more objects need to be investigated over sub-pc to kpc scales. The jet structure of NGC 6251 has also been investigated across the Bondi radius (Tseng et al. 2016), who found parabolic to coni-

---

[1] Bondi radius is an effective area of spherical accretion onto a black hole (Bondi 1952).

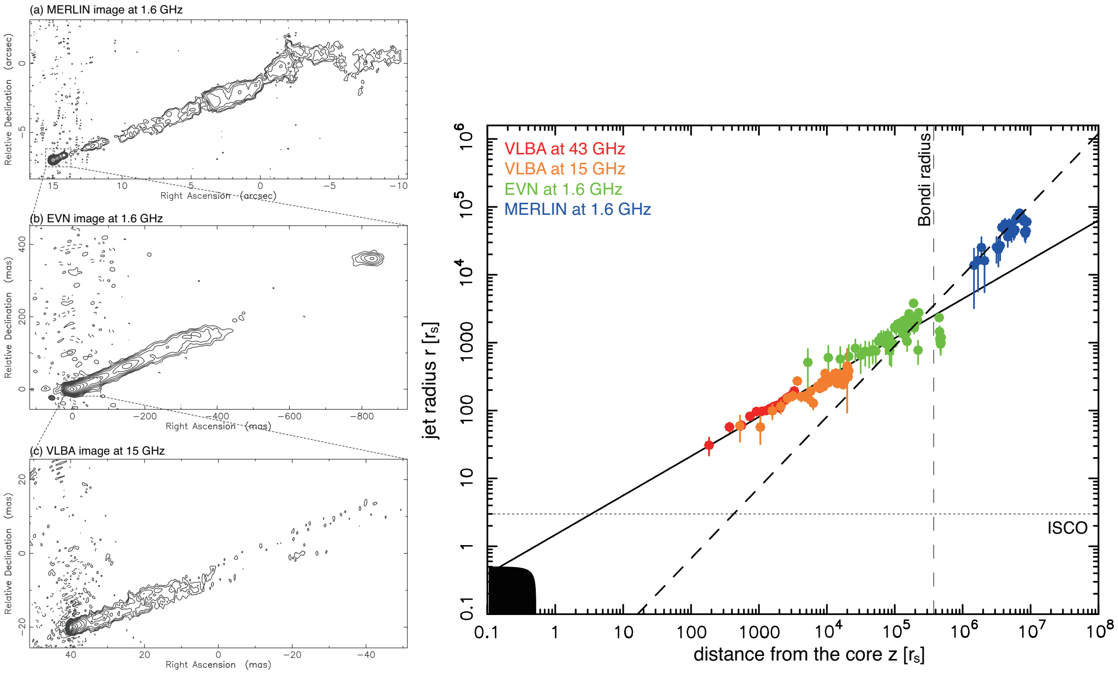

**Figure 1.1:** Discovery of a transition in jet-width profile on M87 jets (Asada & Nakamura 2012). The gray and black area represent surfaces (event horizons) for non-spinning and maximally spinning black holes, respectively.

cal jet structure transitions at the same order of position as the sphere of gravitational influence (SGI[2]). However, unlike M87, the black hole position of NGC 6251 has not been determined using core-shift measurement. Furthermore, the jet velocity profile remains unknown for NGC 6251. The jet width radial profiles of a few other radio galaxies have been investigated, including 3C 84 (Nagai et al. 2014) and Cygnus A (Boccardi et al. 2016b,a). However, no structural transition was confirmed as the investigations focused solely on the inner regions of their respective Bondi radii.

### 1.1.4 Jet driving source

The launching mechanism of a collimated relativistic jet from a black hole system is a long-standing problem in astrophysics. The jet production mechanism is possibly related to mass accretion, because the fraction of the material infalling onto the central black holes is ejected as the jet outflow. Alternatively, the Blandford–Znajek (BZ)

---

[2] Consequently, the Bondi radius is expected to be close to the SGI. See descriptions in Tseng et al. (2016)

mechanism (Blandford & Znajek 1977) is one of the plausible explanations for the powerful jet launch; jets are launched and powered by rotating black holes immersed in externally supported magnetic fields in this theory.

Observational evidence for the jet production mechanisms in AGNs is still unclear. The jet power of luminous blazars is slightly larger than the estimated energy extraction from the rest energy of accreted masses in recent systematic spectral analyses (Ghisellini et al. 2014), although the results depend on the assumptions on the pair fraction and the minimum energy of electrons (e.g., Inoue & Tanaka 2016; Pjanka et al. 2017). This study based on observations supports the BZ mechanism, i.e., a black hole spin-powered jet production. On the other hand, on the basis of the Sloan Digital Sky Survey data release 7 (SDSS DR7) quasar catalog (Schneider et al. 2010) and the NRAO VLA Sky Survey (NVSS), the jet powers correlate with the bolometric disk luminosities as a jet production efficiency of only $\sim 0.01$, implying low black hole spin parameters for radio-loud quasars samples (Inoue et al. 2017). This study suggests accretion-powered jet production; the BZ mechanism is not necessary. Thus, the question of whether the jet drive source is black holes or the accretion disks is under debate.

The observational approach from the investigations of jet-width radial profile potentially provide us crucial evidence of the jet driving source. An extrapolation toward the upperstream on the jet width profile of M87 (Hada et al. 2013) suggest that the converging point of jet width coincides with the Schwarzschild radius approximately (Figure 1.2). This result might an indication of black hole-driven jets. On the other hand, an extrapolation toward the upperstream on the jet width profile of Cygnus A had also been attempted by Krichbaum et al. (1998) and Boccardi et al. (2016a). The minimum measured width of $\sim (227 \pm 98)\mathrm{R_S}$ is significantly larger than the radius of the innermost stable circular orbit (ISCO). They argued that the outer accretion disk is contributing to the jet launching. For the case of NGC 6251, because more than three orders of magnitude extrapolation toward the Schwarzschild scale was required (Tseng et al. 2016), the jet driving source is still inconclusive for this source.

## 1.2 Consideration by MagnetoHydroDinamic (MHD) theoretical study

### 1.2.1 Magnetic driven jet model

It is widely accepted that astrophysical jets are powered electromagnetically, by the magnetised rotation of a central engine. However, how the jets produce the observed emission and maintain the propagation for many orders of magnitude in distance

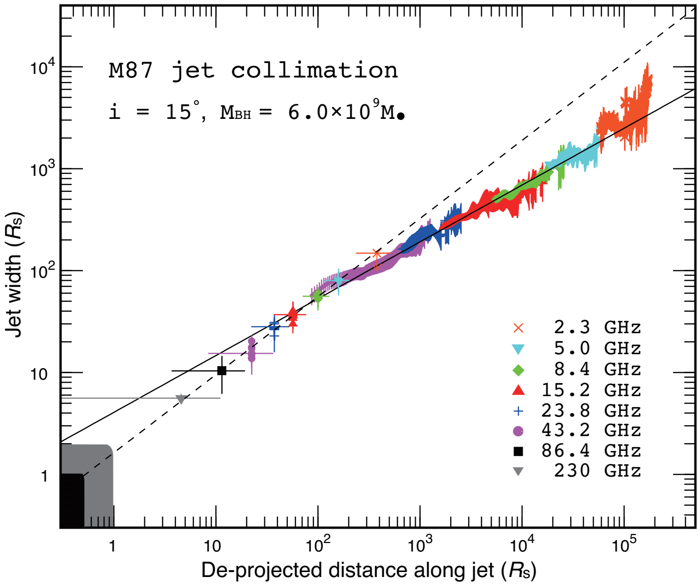

**Figure 1.2:** Extrapolation toward the upperstream on the jet width profile of M87 (Hada et al. 2013), suggesting a possibility of black hole-driven jet formation.

without being disrupted are not theoretically understood.

Collimation is intimately related to the dynamics of Poynting dominated flows (e.g., Komissarov et al. 2009) and conceivably to the dissipation of magnetic energy into kinetic energy. Magnetic self-collimation is a fundamental property of rotating magnetized flows (Heyvaerts & Norman 1989), since they gradually build-up toroidal magnetic field up to large scales, with its hoop stresses that makes itselves collimated. At the same time, the jet plasma acceleration is driven by the gradient of the magnetic pressure. As a consequence, the jet is accelerated and collimated into a parabolic jet until it roughly reaches equipartition that the kinetic energy becomes comparable with the magnetic one (Komissarov et al. 2009).

### 1.2.2 The role of external pressure on jet structure

General relativistic MHD simulations have produced parabolic collimation by external pressure and produced transitions from parabolic to conical streamlines at $\sim 10^2\ R_{\rm g}$ (McKinney 2006). Theoretical studies suggest that non-conical stream ($W(r) \propto r^a$, where $r$ and $W$ are the radial distance and the jet width, respectively) requires a transverse pressure that supports by the external medium with a radial dependence of $p_{\rm ism} \propto r^{-b}$ (e.g., Blandford & Rees 1974; Blandford & Königl 1979).

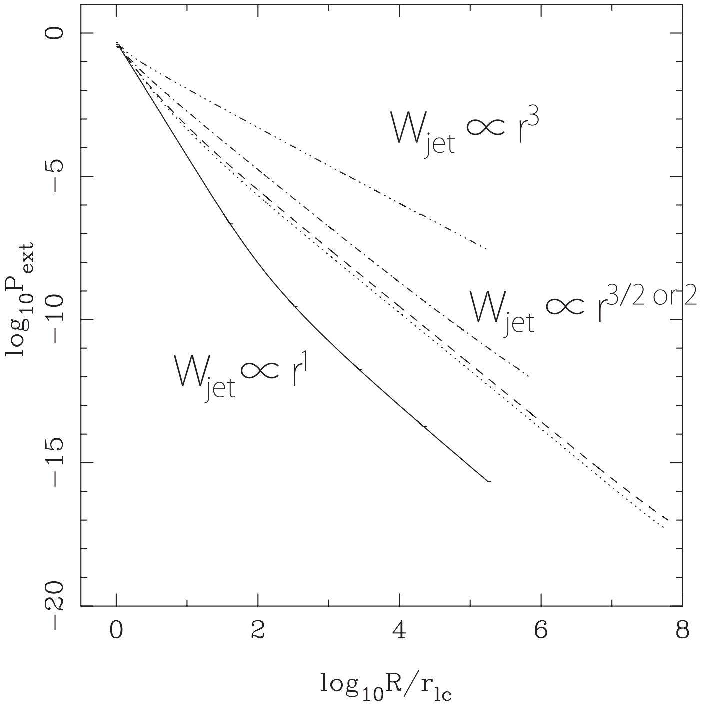

**Figure 1.3:** Evolution of total pressure along the jet boundary (Komissarov et al. 2009).

Komissarov et al. (2009) showed that when the external gas pressure follows $2 \leq b < 4$, the jet forms a parabolic shape with the dependence of $0.5 < a \leq 1$ and eventually becomes conical due to insufficient external pressure support. The conical stream showing $W(r) \propto r$ can be over-pressured against the interstellar medium. However, the physical origin and the distance where the conical expansion starts are not clearly known. This is the case observed in M87 and NGC 6251; their Bondi radii might be the distance where a transition from the parabolic shape to the conical shape occurs. On the other hand, for $b < 2$, the jet maintains a parabolic shape with an over-collimation of $a < 0.5$. The classical picture of conical phase can be provided with $b = 4$. Furthermore, a highly steep dependence of external pressure with $b > 4$ makes the jet shape hyperboloidal. The figure 1.3 shows the evolution of total pressure along the jet boundary in various models. Thus, it is suggested that the radial dependence of external pressure around the astrophysical jets plays a role to control the shape of jet width profile.

## 1.3 Aim of this study

The primary objective of this research is to reveal the evolution of the physical condition in AGN jets throughout the very broad range of physical scales, from the vicinity of the central black hole to the kilo-parsec scale downstream of the jet. The imaging analysis for the measurements of jet width is a powerful approach to obtain the physical volume directly, however, only two AGNs have been investigated over such a broad range so far. For further progress of this research field, (1) the number of AGN samples to be investigated should be increased, in order to evaluate the commonality of phenomena in AGN jets; (2) other parameters from different aspects should be introduced, in order to understand the dynamic energetics involving the jet formation and dissipation, for one AGN. In those previous studies, the range of the physical scale of the survey was very fragmented, or parameters to be measured was limited for each AGN. This PhD thesis provides comprehensive pictures that are derived from the increased number of AGN samples for the jet-width evolution and the continuous profile of physical conditions in an AGN jet over a unprecedentedly wider scale.

## 1.4 Approach of this research

To achieve the above objectives, I adopt the following approaches for the PhD thesis:

- The number of AGN samples whose jet width is measured is increased to five, in addition to two AGNs, M87 and NGC 6251, which are previously investigated by other research groups.
- Inclusion of highly-inclined AGNs, which has never been investigated in terms of the jet width.
- For one AGN, a detailed investigation over a wide range of linear scales by simultaneously obtaining of the jet width and another parameter, radiation profile along jets, is performed.

With these approaches, I expect the following outcomes:

- Correlations with other properties of physical quantities derived from comparison of the five AGNs. The relations between, such as, (1) the transition distance and the Bondi radius, (2) the type of radio galaxy (FR-I/FR-II) and the derived characteristics, (3) known AGN properties and the power-law index of jet width profile, (4) the type of jet driving source and the observed jet properties, (5) the inclination and the other derived characteristics, and so on.

- Verification of expected properties that predicted from theoretical jet models, in terms of the physical connections between the jet width profile and the ambient pressure, the jet width profile and the evolution of magnetic energy, the radial distance and the locations of particle acceleration/dissipation, and so on.

### 1.4.1 Sample selection

For the sample selection, the spatial scale is important in order to investigate the jet structure as finely as possible; thus, it is desirable to have as large black hole as possible and as close as possible. In addition, it is necessary to cover the scale where the jet had changed structure in previous research ($\sim 10^5 R_{\rm S}$). Furthermore, it added on selection criteria that the bipolar jet can be continuously resolved. Then, I chose three objects for target, NGC 4261, NGC 1052, and Cygnus A. These objects can be clearly seen the twin-jet with VLBI image; and they have a large inclination angle compared to two objects in the previous study. If a structural transition is also found in my targets, it will be the first discovery for the counter-jet. When the structural transition of M87 was discovered, there was an opinion that it was not a common feature of the AGN jet, but a phenomenon caused by the local conditions of the jet. If the structural transition is found in either approaching and counter jet, It can be proved that the structural transition of AGN jet is not due to the local condition of the jet. The variation of inclination angle is also noteworthy; the both previous studies objects (M87 and NGC 6251) have small inclination angle ($\sim 15^\circ$). The scale and inclination angle of targets are listed in table 1.1. I can increase the number of samples from two to five objects.

**Table 1.1:** AGN sample with jet-width measurements studied in this thesis.

| Source | $r$ | Ref. | Scale | | $M_{\mathrm{BH}}$ | Ref. | $D$ | Symmetry | $i$ | Ref. |
|---|---|---|---|---|---|---|---|---|---|---|
| | ($\mathrm{R_S}$) | | ($\mathrm{R_S}$ mas$^{-1}$) | (pc mas$^{-1}$) | ($M_\odot$) | | (Mpc) | | (deg) | |
| (1) | (2) | (3) | (4) | (5) | (6) | (7) | (8) | (9) | (10) | (11) |
| M87 | $10^0$–$10^7$ | a, b | 140 | 0.082 | $3$–$6 \times 10^9$ | g, h, i | 16.7 | N | 15 | n, o |
| NGC 4261 | $10^2$–$10^9$ | c | 3200 | 0.15 | $(4.9 \pm 1.0) \times 10^8$ | j | 31.6 | Y | 63 | p |
| Cygnus A | $10^{2.5}$–$10^9$ | c, d, e | 4500 | 1.08 | $7.5 \times 10^9$ | k | 249 | Y | 74.5 | q |
| NGC 1052 | $10^2$–$10^9$ | c | 6400 | 0.095 | $1.5 \times 10^8$ | l | 20.6 | Y | 86 | r |
| NGC 6251 | $10^3$–$10^9$ | f | 8700 | 0.5 | $(6 \pm 2) \times 10^8$ | m | 102 | N | 19 | s |

Columns: (1): source, (2): range of radial distance, where jet width measurement has been done, (3): references for jet width measurements, (4): physical scale in the unit of $\mathrm{R_S}$, corresponding to 1 mas, (5): physical scale in the unit of pc, corresponding to 1 mas, (6): black hole mass in the unit of solar mass (7): references for black hole mass estimates, (8): distance to source, (9): symmetry of apparent jet, (10): inclination, (11): references for inclination.
a: Asada & Nakamura (2012), b: Hada et al. (2013), c: This work, d: Boccardi et al. (2016b), e: Bach (2004), f: Tseng et al. (2016), g: Macchetto et al. (1997), h: Gebhardt & Thomas (2009), i: Walsh et al. (2013), j: Ferrarese et al. (1996), k: Tadhunter et al. (2003), l: Woo & Urry (2002), m: Ferrarese & Ford (1999), n: Biretta et al. (1999), o: Perlman et al. (2011), p: Piner et al. (2001), q: Boccardi et al. (2016b) as an upper limit, r: Baczko et al. (2016), s: Sudou et al. (2000)

### 1.4.2 Method

The present study performs a pixel-based analysis on the total intensity maps of interferometric images at many frequencies and various angular scales, to measure the jet width in the both approaching and counter sides of NGC 4261, NGC 1052, and Cygnus A. The intensity of jets is sliced transversely at a sampling rate of one-fifth of the synthesized beam, and then, a Gaussian fitting to derive a deconvolved width of the jet is performed. The scope of the measurement range in radial distance is physical scales beyond the influence sphere of the gravity of the central black hole (this will result in a kpc scale) from the subpc scales. Transitions in jet-width profiles are expected to appear around the Bondi radii on the basis of the previous studies for the two AGNs (M87 and NGC 6251). Therefore, we will use both VLBI images and VLA images at as wide a frequency range as possible.

Furthermore, the present study will attempt a pixel-based analysis along the jet axis for at least one AGN on the single side (NGC 4261 on the approaching side). In this context, the measurement of jet width has an implication to obtain the volume of jets; at the same time the analyzing of intensity along jets is to obtain the degree of radiation emitted from the volume. Combining the two above observables is to estimate synchrotron luminosity related to internal energy, magnetic field, and jet pressure in jets.

## 1.5 Impact and uniqueness of this thesis

My PhD thesis based on observational studies encompassed a lot of significance for the research field of astrophysical jets, as follows.

- The number of AGN samples whose jet-width profiles have been measured over a wide linear scale has significantly increased from two by previous studies to five. As a result, it enables us to discuss the commonality of evolution for the jet width profile for the first time.

- Highly inclined AGNs showing apparent two-sided jets are added in the survey for the first time in terms of the evolution of jet width profile. As a result, we are able to discuss the commonality about intrinsic symmetry of jets in surrounding medium for the first time.

- The interstellar broadening accompanying super-massive black hole is discovered in extra galaxies for the first time by this study. This was a coincidental outcome under investigation of NGC 1052.

- The galactic pressure distribution at inner 100-pc region which can not be observed at the angular resolution at X-ray regime is estimated for the first time, by combining the jet width profile and the radiation profile along the jet in NGC 4261.
- Jet energetics from acceleration through dissipation was investigated for the first time throughout the physical scales from the several hundred Schwarzschild radius to intergalactic distance in NGC 4261. Such a systematic investigation across telescopes with various spatial resolutions has not been conducted so far.

# Chapter 2

# NGC 4261

**Abstract** This chapter report new measurements of jet width and radiation profiles along jets over the range of $10^3$—$10^9$ Schwarzschild Radius ($R_{\mathrm{S}}$) in the nearby radio galaxy NGC 4261 using multi-frequency Very Long Baseline Array (VLBA) and Very Large Array (VLA) images. In the VLBA images, we found parabolic-to-conical transition signatures on both the approaching and counter jet width profiles at $\sim 10^4 R_{\mathrm{S}}$ from the central engine. A transition in the radiation profile along the approaching jet was also found at $\sim 10^4 R_{\mathrm{S}}$ clearly. Based on the consistency of the transition locations, we conclude that the physical conditions of the NGC 4261 jets change at this distance. Jet flows that change from accelerating to expanding regions, were previously found in M87 and NGC 6251, are presumably present in NGC 4261. Additionally, we found another transition in the radiation profile at $\sim 3 \times 10^6 R_{\mathrm{S}}$ in the conical region. NGC 4261 is the first case in which a jet structural transition is suggested in both the approaching and counter jets; this implies that the active galactic nucleus (AGN) jet collimation process is fundamentally characterized by the global distribution of ambient rather than the local interaction between the jet and the surrounding medium. We discuss the evolution of jet conditions in terms particle acceleration, cooling, dissipation, and jet pressure balance with the surrounding hot gas.

## 2.1 Introduction

The collimation mechanism of relativistic jets in active galactic nuclei (AGNs) is an unresolved problem in astrophysics. Nevertheless, there have been some progress from recent observational studies on nearby AGN jets. In the radio galaxy M87, Asada & Nakamura (2012) discovered an enduring parabolic jet structure between a few hundred and $10^5$ Schwarzschild radii ($R_{\mathrm{S}}$) from the central engine as well as a transition into a conical streamline above $\sim 10^6$ $R_{\mathrm{S}}$. Because the transition site is found near the Bondi radius of M87, the possibility of a physical relation between jet confinement and a change radial profile of the ambient pressure has been discussed. General relativistic magneto hydro dynamic simulations have produced parabolic collimation by external pressure and produced transitions from parabolic to conical streamlines at $\sim 10^2$ $R_{\mathrm{g}}$ (McKinney 2006). Hada et al. (2013) found a possible change in the jet collimation shape in the vicinity of the central black hole of M87, that is potentially related to a magnetic collimation process and/or interactions with the surrounding gas at the jet base. Asada et al. 2014 subsequently discovered that the site at which the bulk acceleration of the jet (Nakamura & Asada 2013; Mertens et al. 2016; Hada et al. 2017) is occurring corresponds to the region in which the jet width evolves into a parabolic shape, and deceleration has been found in the conical downstream (Biretta et al. 1999; Meyer et al. 2013). The observational evidence for the direct relation between the collimation and the bulk acceleration of jets was made possible by: (i) intensive monitoring of jet proper motion; (ii) spatial resolving in the direction of jet width over a wide range of physical scales in both the parabolic and conical regions, in conjunction with; (iii) precise determination of the central engine location from very-long-baseline interferometry (VLBI) observations toward M87, which is one of the nearest radio galaxies. The position of the central engine of M87 has been successfully determined by measuring frequency-dependent shifts of the core position (Konigl 1981; Lobanov 1998) using multi-frequency phase-referencing VLBI observations (Hada et al. 2011).

To determine whether transition from parabolic (accelerating) to conical (decelerating) regions is universal among AGN jets, more objects need to be investigated over sub-pc to kpc scales. The jet structure of NGC 6251 has also been investigated across the Bondi radius (Tseng et al. 2016), who found a parabolic-to-conical jet structure transition at the same order of position as the sphere of gravitational influence (SGI[1]). However, unlike M87, the black hole position of NGC 6251 has not been determined using core-shift measurement. Furthermore, the jet velocity profile remains unknown. The jet width radial profiles of a few other radio galaxies have been investigated, including 3C 84 (Nagai et al. 2014) and Cygnus A (Boccardi et al. 2016b,a). However,

---

[1] Consequently, the Bondi radius is expected to be close to the SGI. See descriptions in Tseng et al. (2016)

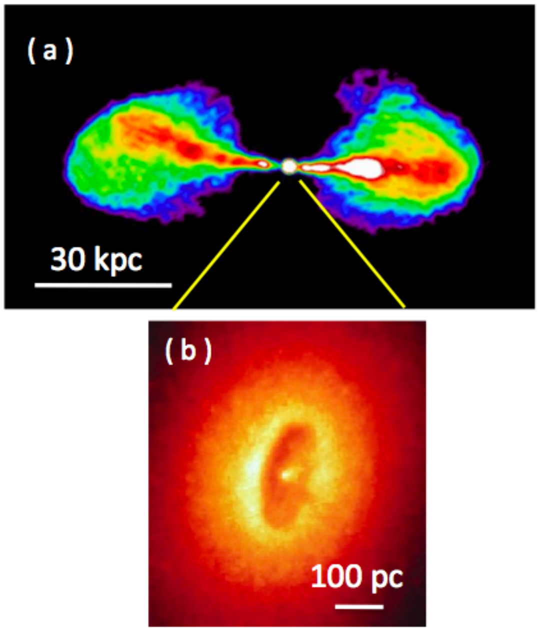

**Figure 2.1:** (a) Large-scale radio image of NGC 4261 obtained using the NRAO Very Large Array, and (b) Hubble-Space-Telescope image of NGC 4261.

no structural transition were confirmed as the investigations focused solely on the inner regions of their respective Bondi radii.

NGC 4261 (3C 270), a nearby (31.6 Mpc; Tonry et al. 2000) Fanaroff–Riley Class I (FR-I) radio galaxy, is another example of a galaxy with jets whose width profile has been measured in the range $10^3$–$10^9 \mathrm{R_S}$ (Nakahara et al. 2016). NGC 4261 has a central black hole with a mass of $(4.9 \pm 1.0) \times 10^8\ M_\odot$ (Ferrarese et al. 1996) and closely symmetric two-sided jets up to the kilo-parsec scale (Birkinshaw & Davies 1985). At the distance of NGC 4261, an angular resolution of 1 milliarcsecond (mas) is equivalent to a linear scale of $\sim$ 0.15 pc, which, given the mass of the central black hole, is equivalent to $\sim 3,200\ R_\mathrm{S}$; VLBI observations enable the study of jets in the region at less than 1 pc from the central engine. Furthermore, the position of the central engine of NGC 4261 has been accurately determined using the phase-referencing VLBI technique, allowing the location of the jet's origin at a distance of $82 \pm 16$ $\mu$as from the 43 GHz core, corresponding to a de-projected distance of $310 \pm 60\ R_\mathrm{S}$ (Haga et al. 2015). These measurements allow us to investigate the radial profile of NGC 4261's jet width as a function of the (de-projected) distance along the jets from the central engine with little ambiguity, as was done for M87. Moreover, the

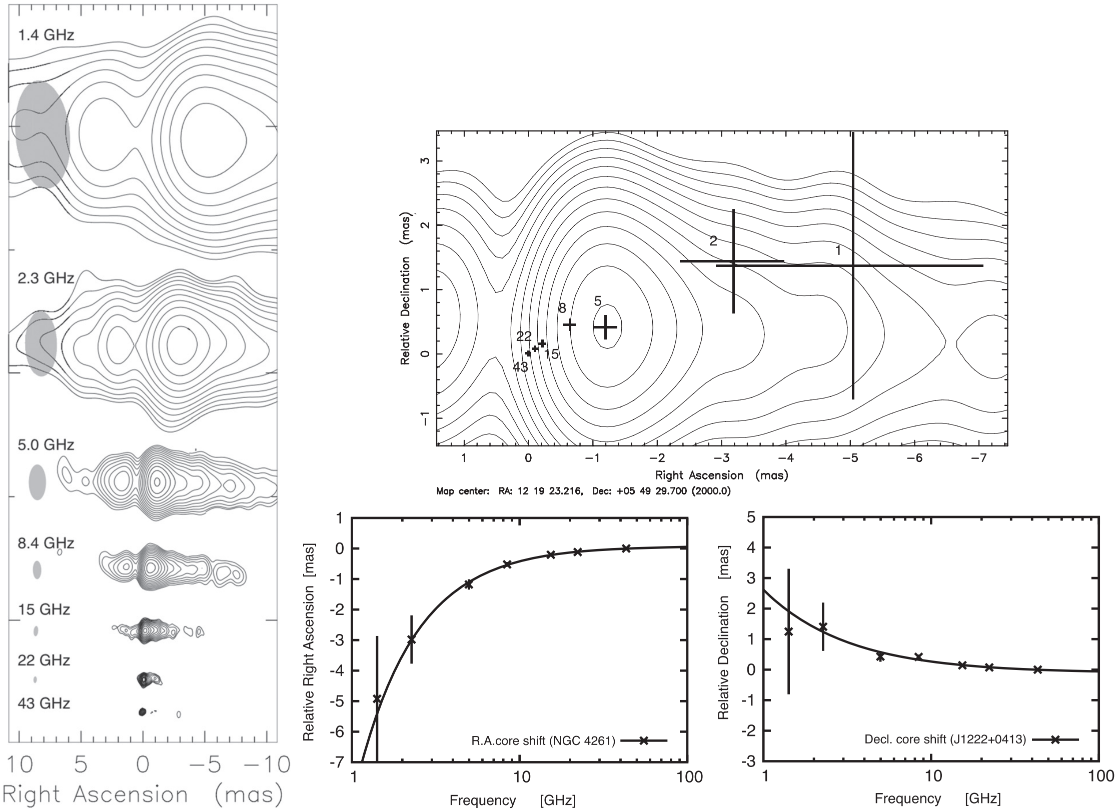

**Figure 2.2:** Core-shift measurements of NGC 4261 jets (Haga et al. 2015). The core shift phenomenon is apparent effect that the position of the jet's upperstream end moves along the jet axis depending on observing frequency due to an opacity effect.

large inclination angle ($i = 63°$; Piner et al. 2001) allows both the approaching and counter jets to be clearly imaged, a special property not seen in the previously studied sources. The dual-sidedness of jets is potentially crucial in discriminating whether the jet properties are influenced by a local condition or the global environment.

In this thesis, we present results based on a re-analysis of jet widths using Very Long Baseline Array (VLBA) and Very Large Array (VLA) data. Furthermore, new measurements of the radiation profile along the jets are reported. By contrasting the structural and radiation features of the two jet profiles, we investigate the evolution of the physical condition of the jets over a distance range of $10^3$–$10^9$ $R_{\mathrm{S}}$ from the central engine of NGC 4261.

The chapter is structured as follows. In Section 2.2.1, we present and describe the data used in this study. In Section 2.2.2, an improved method of measurement of jet width is introduced. In Section 2.3, we show the results of analyses of the jet width and radiation profiles along the jets. In Section 2.4, we discuss by comparing our result for the jet width profiles of NGC 4261 with those of the other AGNs that were previously investigated (The evolution of the physical conditions along the jets based on the calculated synchrotron luminosity, equipartition magnetic field strength, and jet pressure are discussed in Chapter 5 for comprehensive discussions). Finally, we summarize our findings in Section 2.5.

## 2.2 Image Analyses of Structures and Radiation Profiles along Jets of NGC 4261

### 2.2.1 Data

#### VLBA data

To investigate the innermost region of the jets in NGC 4261, we used the data sets that were previously presented by Haga et al. (2015), in which the frequency-dependent shifts of the core positions in the jets of NGC 4261 were measured using the phase-referencing technique. NGC 4261 was observed using the VLBA at four frequencies (1.4, 2.3, 5.0, and 8.4 GHz) on July 03, 2003 and at three frequencies (15, 22, and 43 GHz) on June 6, 2003. Further details of the observations and the data reduction processes are given in Haga et al. (2015). In the present study, we used the reduced data to remake the self-calibrated images of NGC 4261 using uniform, natural, and tapered weighting of the uv-data for image synthesis to obtain as many compact and extended emission components as possible.

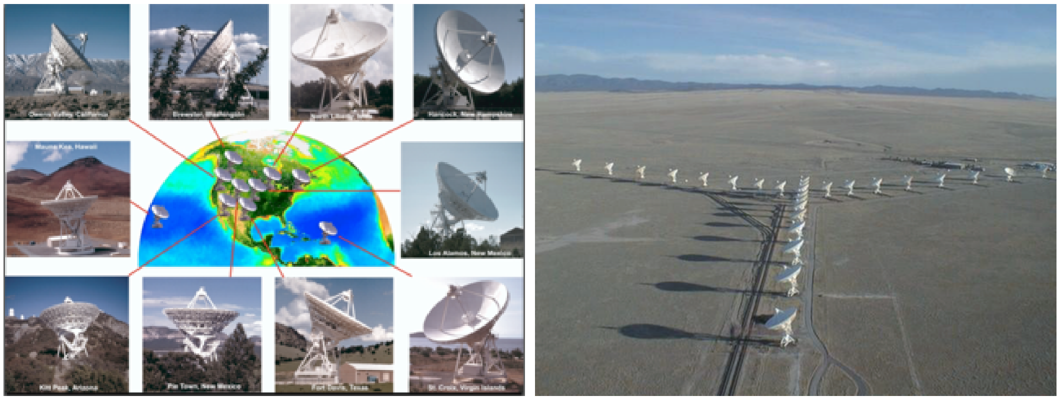

**Figure 2.3:** US NRAO's Very Long Baseline Array (VLBA) with the longest baseline of 8611 km and Very Large Array (VLA) with the longest baseline of 36.4 km. (Image courtesy of NRAO/AUI)

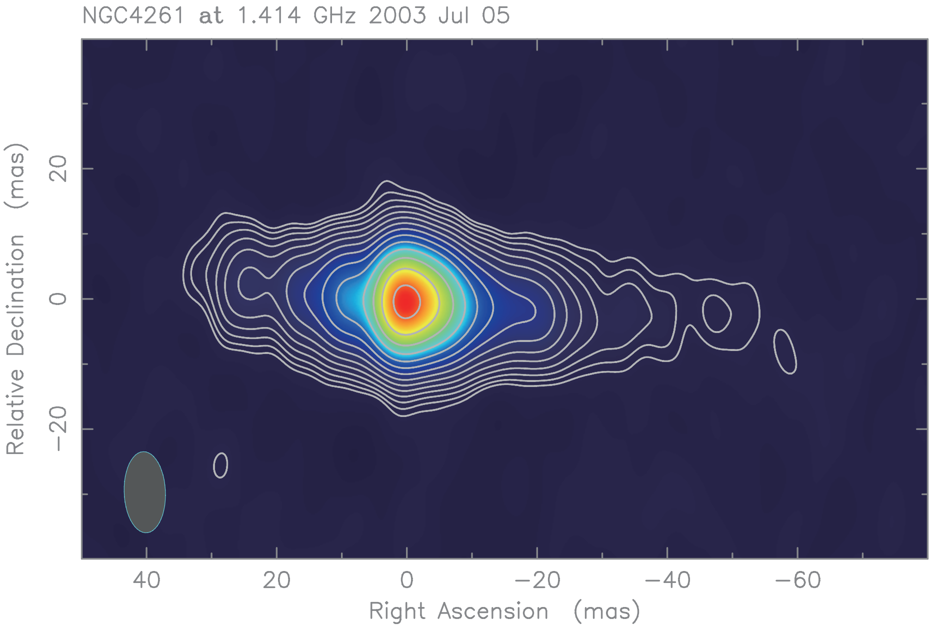

**Figure 2.4:** Radio image at 1 GHz VLBA. Contours start from the 3 sigma image RMS noise and increase by factors of $\sqrt{2}$.

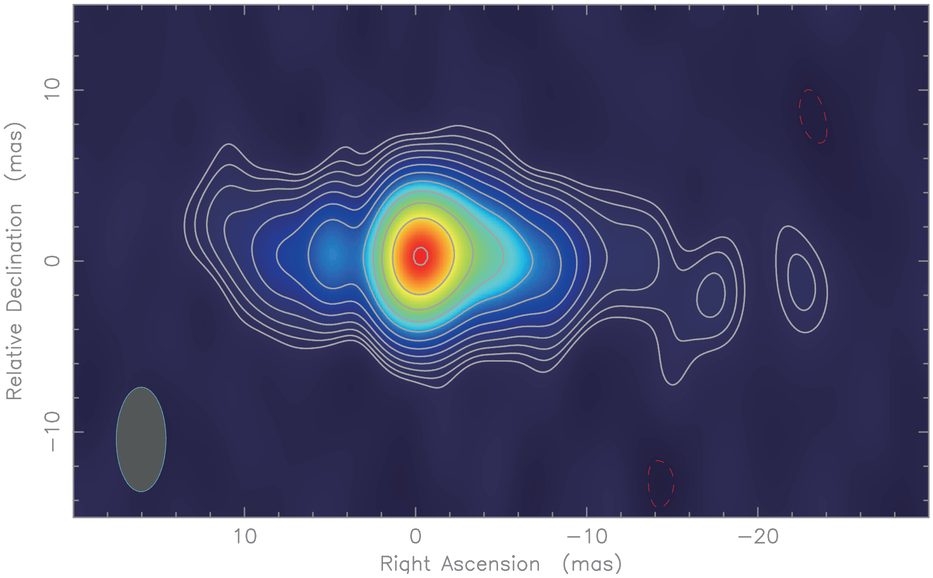

**Figure 2.5:** Radio image at 2 GHz VLBA. Contours start from the 3 sigma image RMS noise and increase by factors of $\sqrt{2}$.

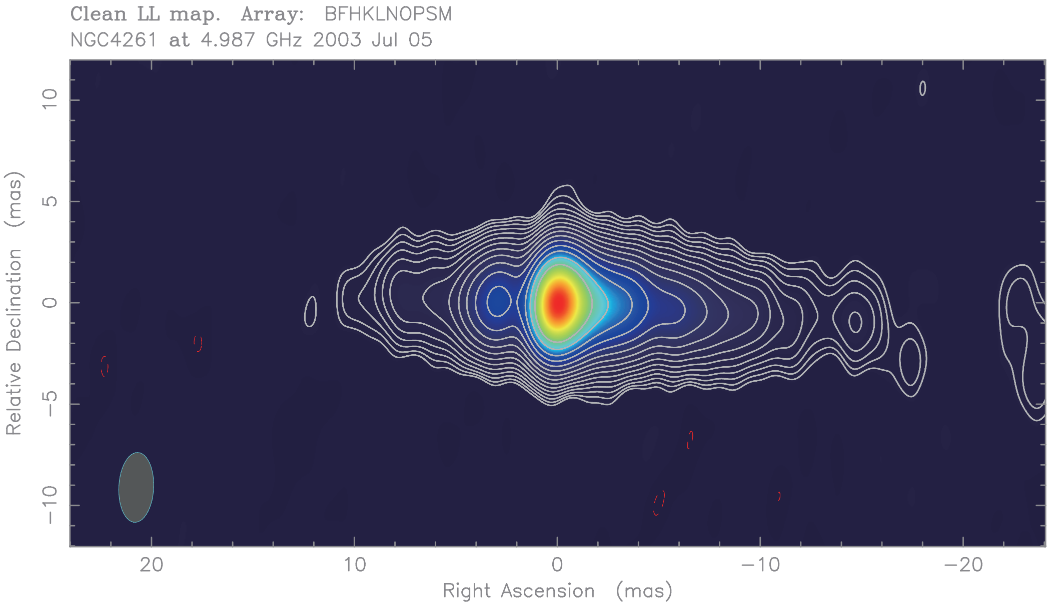

**Figure 2.6:** Radio image at 5 GHz VLBA. Contours start from the 3 sigma image RMS noise and increase by factors of $\sqrt{2}$.

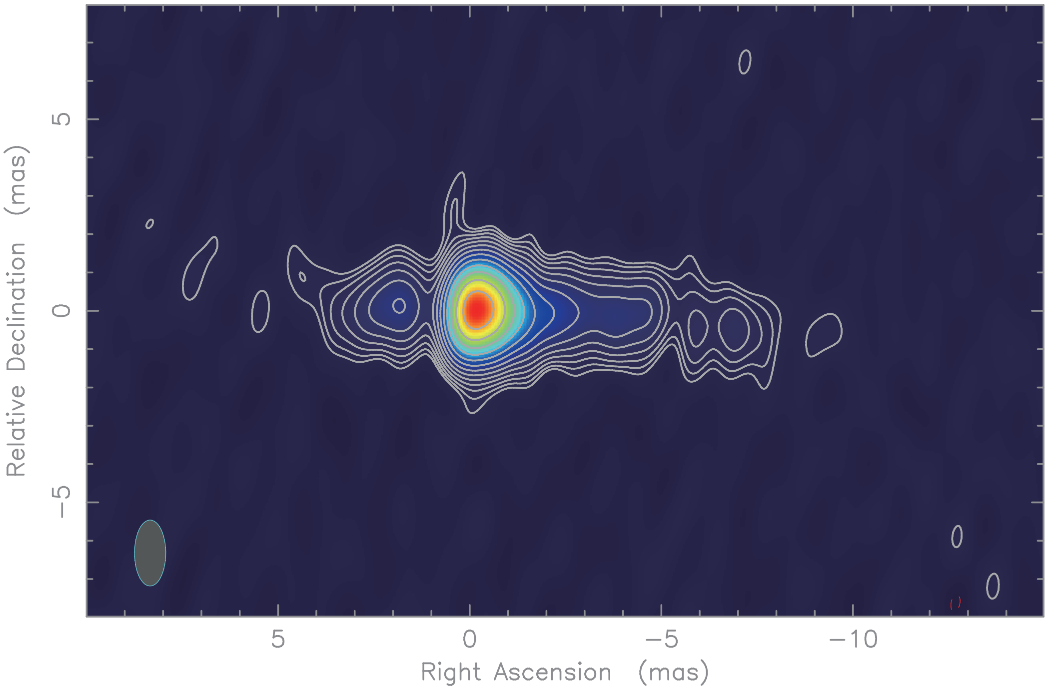

**Figure 2.7:** Radio image at 8 GHz VLBA. Contours start from the 3 sigma image RMS noise and increase by factors of $\sqrt{2}$.

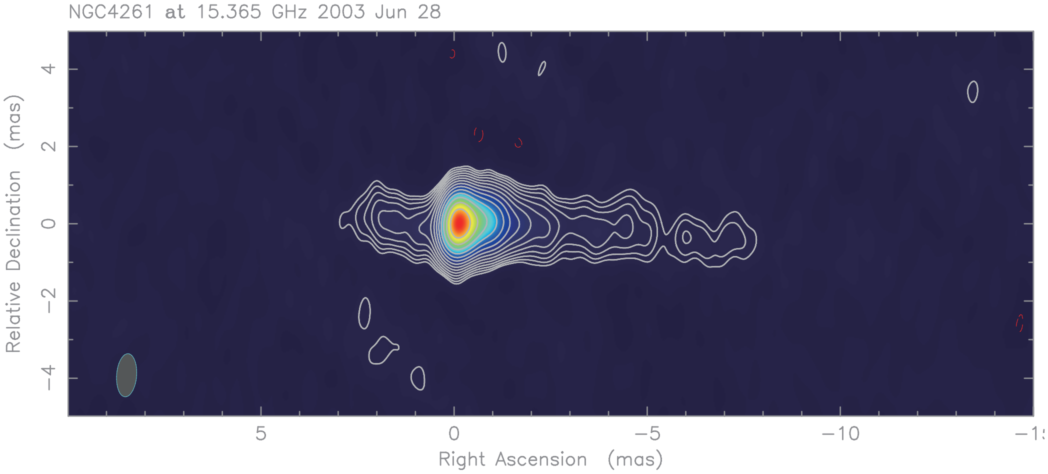

**Figure 2.8:** Radio image at 15 GHz VLBA. Contours start from the 3 sigma image RMS noise and increase by factors of $\sqrt{2}$.

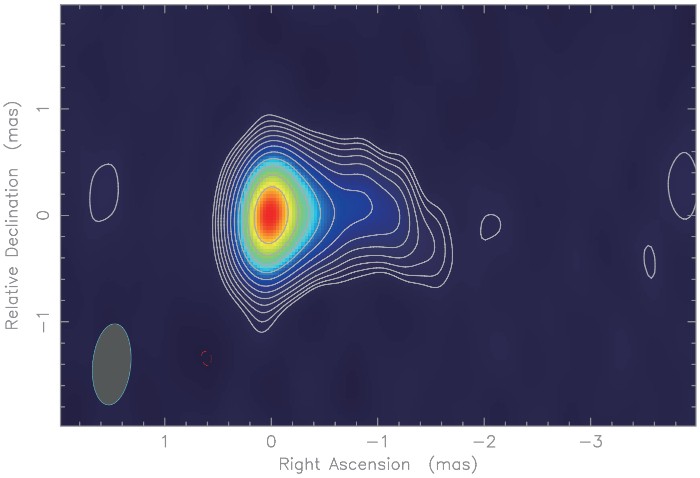

**Figure 2.9:** Radio image at 22 GHz VLBA. Contours start from the 3 sigma image RMS noise and increase by factors of $\sqrt{2}$.

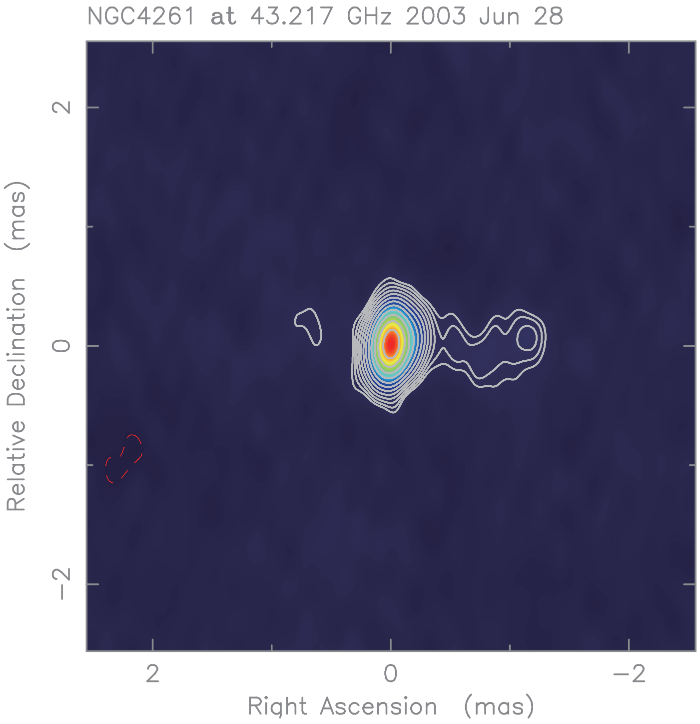

**Figure 2.10:** Radio image at 43 GHz VLBA. Contours start from the 3 sigma image RMS noise and increase by factors of $\sqrt{2}$.

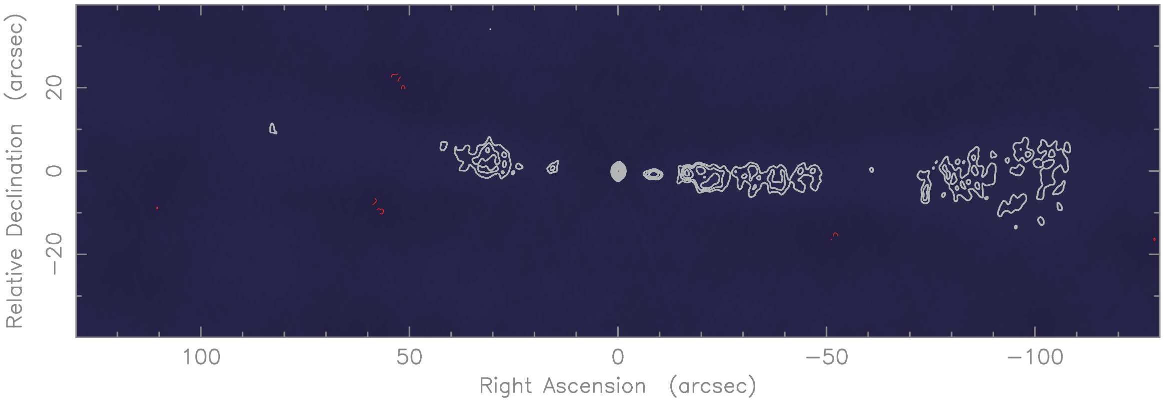

**Figure 2.11:** Radio image at 1 GHz VLA. Contours start from the 3 sigma image RMS noise and increase by factors of $\sqrt{2}$.

### VLA data

We also used VLA data sets (AJ229, AP77 and AB376) in this study. AJ229, which was retrieved from the data archive system of the National Radio Astronomy Observatory. The observations was conducted on April 15–16, 1994 at 1.4 GHz using the VLA's A-array configuration. The data include dual-circular polarization, measured at a bandwidth of 3 MHz. The data reduction procedures followed standard VLA data methodology for use of the Astronomical Image Processing System (AIPS). Using Difmap for imaging, we performed iterative deconvolution and self-calibration procedures. A final image produced from the AP77 data combined with data from AB376 is available online[2]. AP77 and AB376 were observed at 4.86 GHz on 23 April 1984 using the VLA C-configuration and on February 2, 1986 using the D-configuration. Dual-circular polarization was measured at a bandwidth of 100 MHz. The retrieved image was used in the present study.

## 2.2.2 Image Analyses

The NGC 4261 jet shows a single ridge structure extending roughly along the east-west direction (position angle $PA \approx -90$ deg), as shown in Figure 2.12 for example. To prepare the jet width measurements along the direction perpendicular to the jet axis, we remade each VLBA image using clean models and a restored elliptical Gaussian beam. The major- and minor-axis widths of the restored beam were specified by trun-

---

[2] http://www.slac.stanford.edu/~teddy/Atlas/

**Table 2.1:** Image performance

| Telescope<br><br>(1) | $\nu$<br>(GHz)<br>(2) | $I_{\rm peak}$<br>(mJy/beam)<br>(3) | $\sigma$<br>(mJy/beam)<br>(4) | $\theta_{\rm maj}$<br>(mas)<br>(5) | $\theta_{\rm min}$<br>(mas)<br>(6) |
|---|---|---|---|---|---|
| VLBA | 1.4 | 47.4 | 0.2 | 12.5 | 6.3 |
| | 2.3 | 70.1 | 0.5 | 6.1 | 2.9 |
| | 5.0 | 117.1 | 0.6 | 2.5 | 1.2 |
| | 8.4 | 101.6 | 0.6 | 1.5 | 0.7 |
| | 15 | 113.4 | 0.7 | 0.9 | 0.4 |
| | 22 | 123.2 | 1.2 | 0.6 | 0.3 |
| | 43 | 72.9 | 0.9 | 0.3 | 0.2 |
| VLA | 1.4 | 159.2 | 0.4 | $1.7 \times 10^3$ | $1.4 \times 10^3$ |
| | 4.9 | 300.5 | 0.5 | $8.0 \times 10^3$ | $8.0 \times 10^3$ |

The columns contain the following data: (1) telescope; (2) frequency; (3) peak intensity; (4) image RMS noise; (5) major axis size of the synthesized beam; (6) minor axis size of the synthesized beam

cating the original synthesized beam numbers beyond the third decimal point[3]. At the same time, the position angle was specified as PA= 0 deg. Using this convolution, we defined the spatial resolution precisely, with the full width at half maximum (FWHM) of the restored beam $\theta_{\rm res}$ in the direction of the slice (PA= 0 deg). Then, we obtained a pixel-based slice profile along PA= 0 deg, perpendicular to the jet axis in the region in which the peak intensity is stronger than three times the image noise, $3\sigma$, using the `AIPS SLICE` task. Following previous studies (Tseng et al. 2016; Boccardi et al. 2016b, see also a study of resolution limit by Lobanov 2005), the intensity slice at each distance was resampled over sets of pixels equivalent to approximately one-fifth of the FWHM of the synthesized beam as independent measurements. Finally, apparent jet widths on the images were measured by fitting to the resampled slice values using a Gaussian model of the FWHM, $\theta_{\rm fit}$, as a free parameter. An intrinsic jet width $\theta_{\rm jet}$ was determined by deconvolution using the defined resolution $\theta_{\rm res.}$, i.e., $\theta_{\rm jet}^2 = \theta_{\rm fit}^2 - \theta_{\rm res}^2$. We adopted fitting solutions that met the following three criteria: (1) the intensity exceeded $3\sigma$; (2) $\theta_{\rm fit} < \theta_{\rm res}$; and (3) the fitting error of the jet width did not exceed 100%.

Jet width measurements on the VLA images were carried out in essentially the same manner, except with slicing of the VLA images performed every 10 arcsec from the radio core. In addition, to avoid contamination from extended emissions in radio lobe regions in measuring jet width, we made fits to each component of the jet and

---

[3] In Nakahara et al. (2016), a restored beam was determined by slicing the synthesized beam, which potentially involved sidelobes and fitting errors. This is the reason why we improved the method in the present study.

lobe emissions using two-Gaussians over the range in which the peak intensity of the jet was stronger than that of the lobe.

Determining the distance from the central engine to each slice location was essential in constructing the radial profile of jet width for NGC 4261. We applied the results from Haga et al. (2015), in which the distance from the central engine to the radio core was measured precisely at each frequency using the phase-referencing technique. In that study, it was noted that in NGC 4261 the position of the radio core is affected by a frequency-dependent opacity effect— the so called core-shift effect.

In addition, we measured the radial profile of intensity along the jet, this is an another aspect to investigate jet structures that includes radiative processes depending on the distance from the black hole. As shown by the dashed line in Figre 2.12, we performed pixel-based analysis to slice the VLBA images along the jet axis (PA$\sim -90$ deg), using the `AIPS SLICE` task. From this process, we obtained intensity (mJy beam$^{-1}$) and position values. As the VLA images contain lobe emission contamination, we used the peak intensity of the deconvolved jet width function. We also applied the core-shift effect to correct the position.

## 2.3 Results

From the analysis described in Section 2.2.2 above, we obtained three types of information, jet width, intensity, and distance from the central engine along the jet, for both the approaching and counter jets in NGC 4261.

### 2.3.1 Profile of Jet Width

Radial profiles of jet width are shown in Figures 2.13 and 2.14 for the approaching and counter side jets, respectively. Figure 2.15 shows a comparison of the two radial profiles. In all three plots, the unit in the horizontal axis is physical distance in Schwarzschild radii ($R_{\mathrm{S}}$), converted from mas on projected jet images based on the assumed black hole mass ($(4.9 \pm 1.0) \times 10^8\ M_\odot$; Ferrarese et al. 1996), distance from NGC 4261 (31.6 Mpc; Tonry et al. 2000), and inclination angle ($i = 63°$; Piner et al. 2001).

These measurements provide a radial profile of jet width in NGC 4261 over the range $\sim 10^{2.5}$–$10^9\ R_{\mathrm{S}}$, although our measurements have a gap between $\sim 10^{5.5}$ and $10^{7.5} R_{\mathrm{S}}$. In most frequencies, the core and the jet near the core could not be resolved. Consequently, in the approaching jet results the most upstream plots are obtained from core slices at 8 and 15 GHz. In the counter jet results, there are significantly fewer measurements than in the approaching jet results owing to Doppler de-beaming. Moreover, there is dimming of the counter jet image caused by free–free absorption.

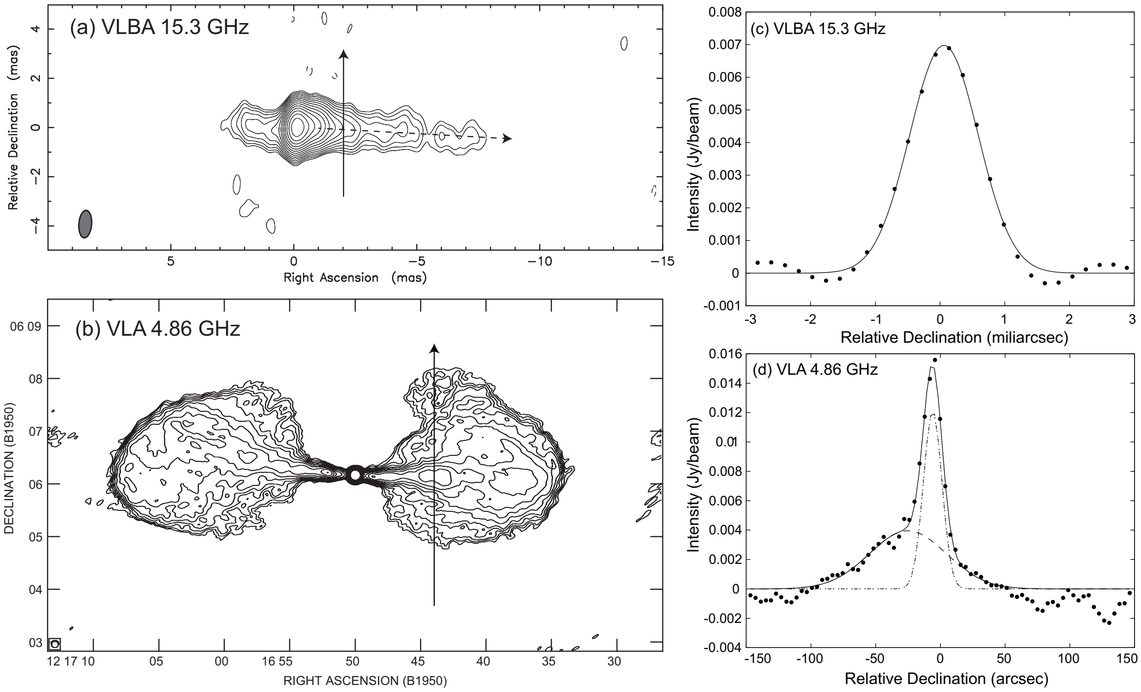

**Figure 2.12:** (a) 15 GHz VLBA image. Contours start from the 3-sigma image RMS noise and increase by factors of $\sqrt{2}$ ($1\sigma = 0.358$ mJy beam$^{-1}$). The vertical line on the image represents the location of a slice example (c), which separates 2.0 mas from the core. The dashed line indicates the location of the slice used for investigating the intensity profile (Figure 2.17). (b) 5 GHz VLA image. Contours start from the 3-sigma image RMS noise and increase by factors of $\sqrt{2}$ ($1\sigma = 0.395$ mJy beam$^{-1}$). The vertical line on the image represents the location of the slice example (d), which separates 90 arcsec from the core. (c) Intensity profile at the location of a slice in the 15 GHz VLBA image (a). The dots indicate the image intensity. The solid curve shows Gaussian fitting results. (d) Intensity profile at the location of a slice in the 4.86 GHz VLA image (b). The dots indicate the image intensity. The dot-dashed curve shows the fitting result of the jet component. The dashed curve shows the fitting result of the lobe component. The solid curve shows the fitting result of jet plus lobe components.

The existence of an accretion disk in NGC 4261 has been suggested (Jones et al. 2000). The innermost region of the counter jet is influenced by its absorption at 5–15 GHz (Haga et al. 2015), which may account for the lack of available 8–22 GHz measurements in our study.

We first fitted the measurements of jet width along the jet axis with a single power-law ($W_{\rm jet} \propto r^a$, where $W_{\rm jet}$ is the jet width, $r$ is the distance from the black hole in units of $R_{\rm S}$, and $a$ is the power-law index). This produced $a = 1.04 \pm 0.01$ and $a = 0.95 \pm 0.02$, for the approaching and counter sides, respectively. The respective reduced $\chi^2$ values are 0.53 and 0.68, suggesting that the fitting was robust or potentially affected over-sampling caused by superimposing the jet width profiles measured at multi-frequency.

Because previous studies of M87 (Asada & Nakamura 2012) and NGC 6251 (Tseng et al. 2016) found a transition in these jet width profiles, we then performed an additional fitting for NGC 4261 using a broken power-law function to probe a flatter tail signature in the upper stream side (Figure 2.13). The adopted fitting function is,

$$W_{\rm jet}(r) = W_0 \, 2^{\frac{a_{\rm u}-a_{\rm d}}{s}} \left(\frac{r}{r_{\rm b}}\right)^{a_{\rm u}} \left(1 + \left(\frac{r}{r_{\rm b}}\right)^{s}\right)^{\frac{a_{\rm d}-a_{\rm u}}{s}}, \tag{2.1}$$

where $W_0$ is the scale factor, $a_{\rm u}$ is the power-law index for the upstream jet, $a_{\rm d}$ is the power-law index for the downstream jet, $r_{\rm b}$ is the break location, and $s$ is the sharpness of the profile at the break (here, we use the fixed value $s = 10$). The fitting results are listed in Table 2.2. The reduced $\chi^2$ values are 0.464, 0.515, and 0.570 for the approaching jet, counter jet, and combined cases, respectively. The fit solutions indicate that the structures of the approaching and counter jets are consistent; the locations of the transition and power-law indices in the upperstream are in close agreement within error, and the downstream is conical with a power-law index of approximately unity. Note that this broken power law fit result is not statistically superior to the single power law fit; however, a transition was found in the radiation profile at nearly same location (as will be discussed later in Section 2.3.2). Therefore, the transition in the jet width profile can be supported by our joint analysis.

Figure 2.15 shows the fitting results of jet width radial profiles, which indicate that the jet structures are consistent between sides that there are transitions at approximately $10^4$ $R_{\rm S}$ on both sides. Correspondingly, we also obtained a fitting result using combined data from both sides. The power-law indices are approximately 0.5 and 1.0 in the upstream and the downstream regions, respectively (Table 2.2). These values suggest that both NGC 4261 jets transition from the parabolic to conical structures. Figure 2.16 shows the error estimate of the broken power-law fitting. The error calculation is described in Appendix B.

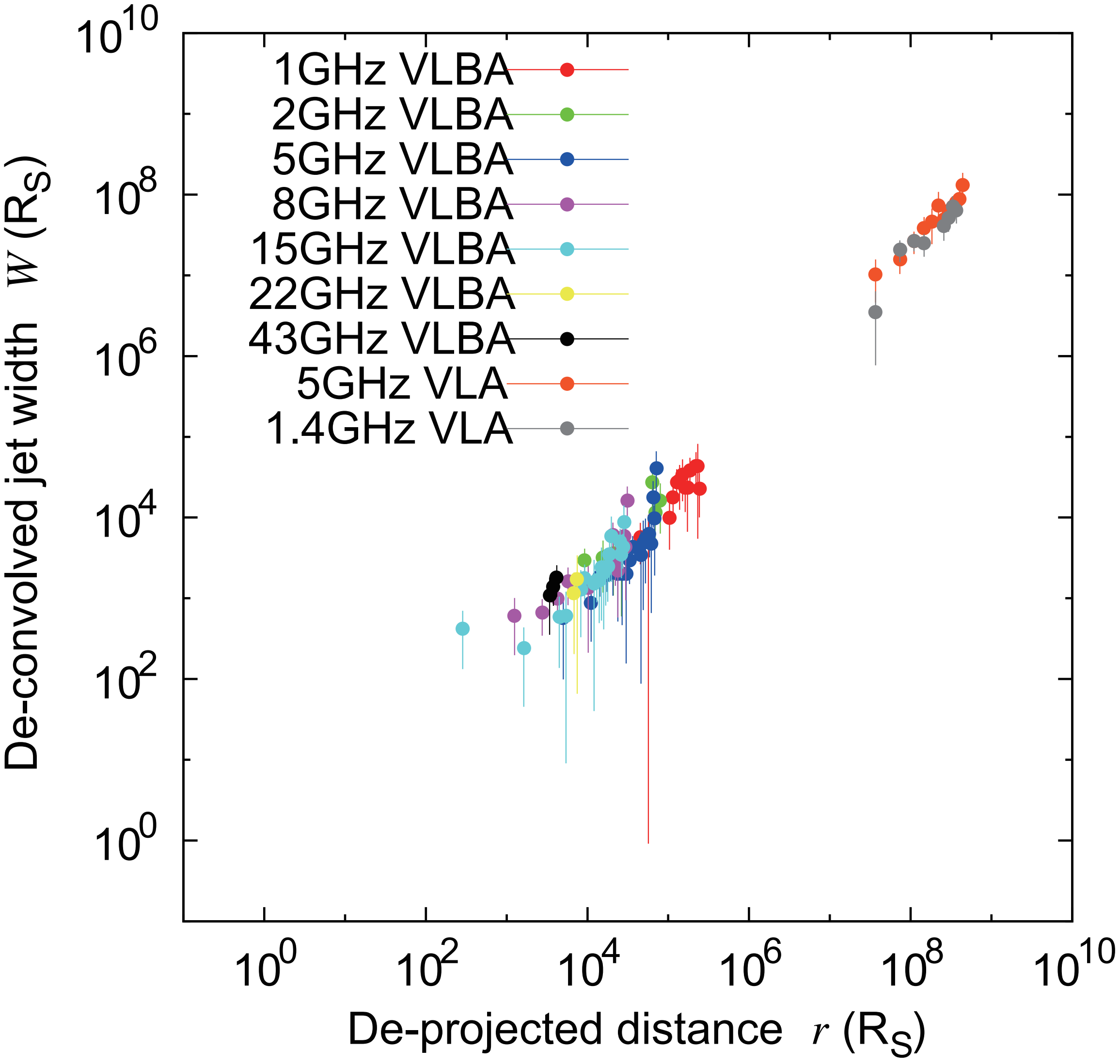

**Figure 2.13:** Radial profile of measured approaching side jet width. The horizontal axis shows distance from the central engine, which takes into account the core-shift effect. The vertical axis shows the deconvolved jet width. The color variation encodes the observed frequencies for the VLBA data, red: 1GHz, green: 2 GHz, blue: 5 GHz, purple: 8 GHz, light blue: 15 GHz, yellow: 22 GHz, black: 43 GHz; for the VLA data, orange: 5 GHz, gray: 1.4 GHz.

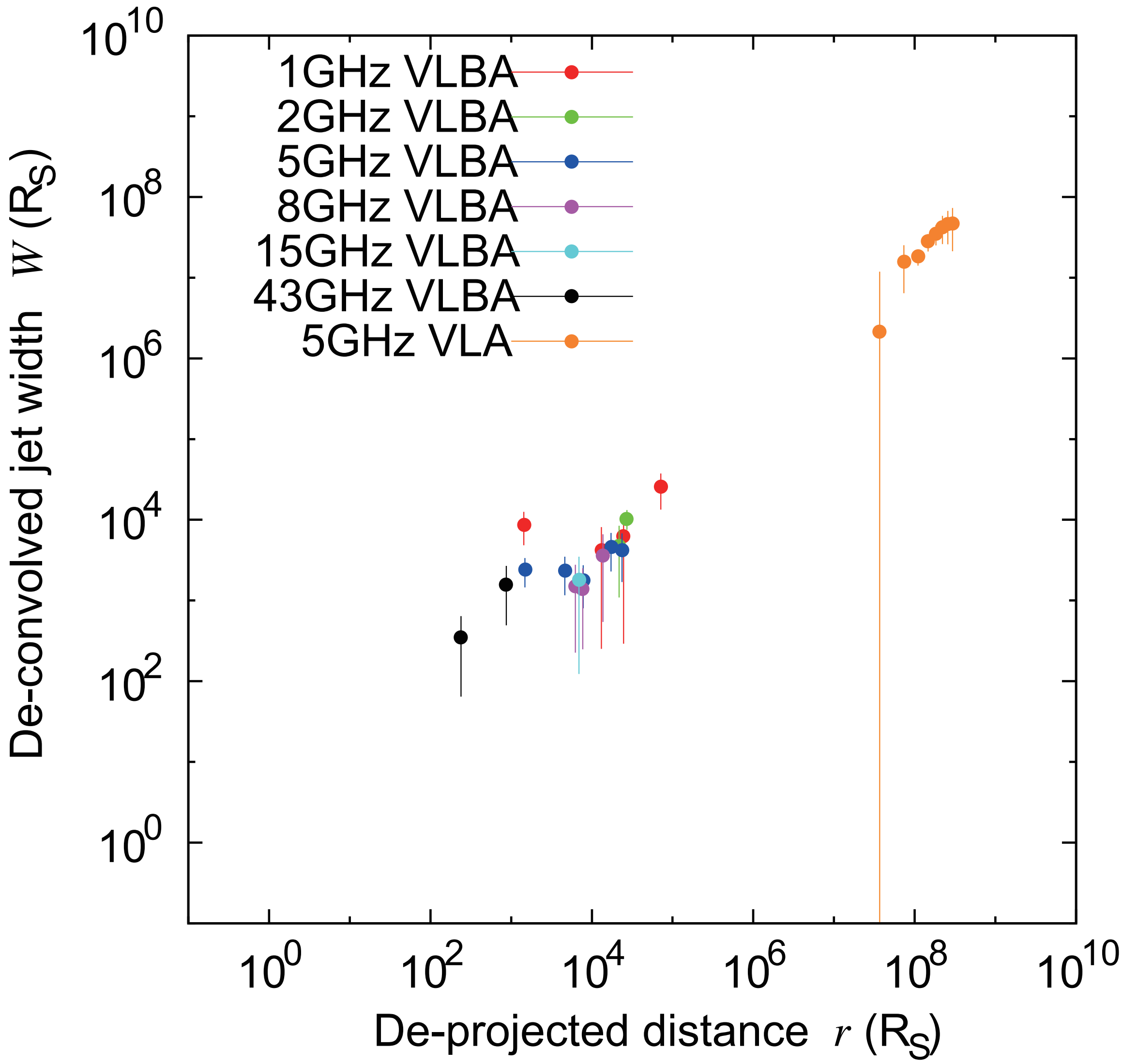

**Figure 2.14:** Radial profile of measured counter side jet width. The horizontal axis shows distance from the central engine, which takes into account the core-shift effect. The vertical axis shows the deconvolved jet width. The color variation encodes the observed frequencies for the VLBA data, red: 1GHz, green: 2 GHz, blue: 5 GHz, purple: 8 GHz, light blue: 15 GHz, yellow: 22 GHz, black: 43 GHz; for the VLA data, orange: 5 GHz. No good measurement was available for VLBA 22 GHz and VLA 1 GHz on the counter jet.

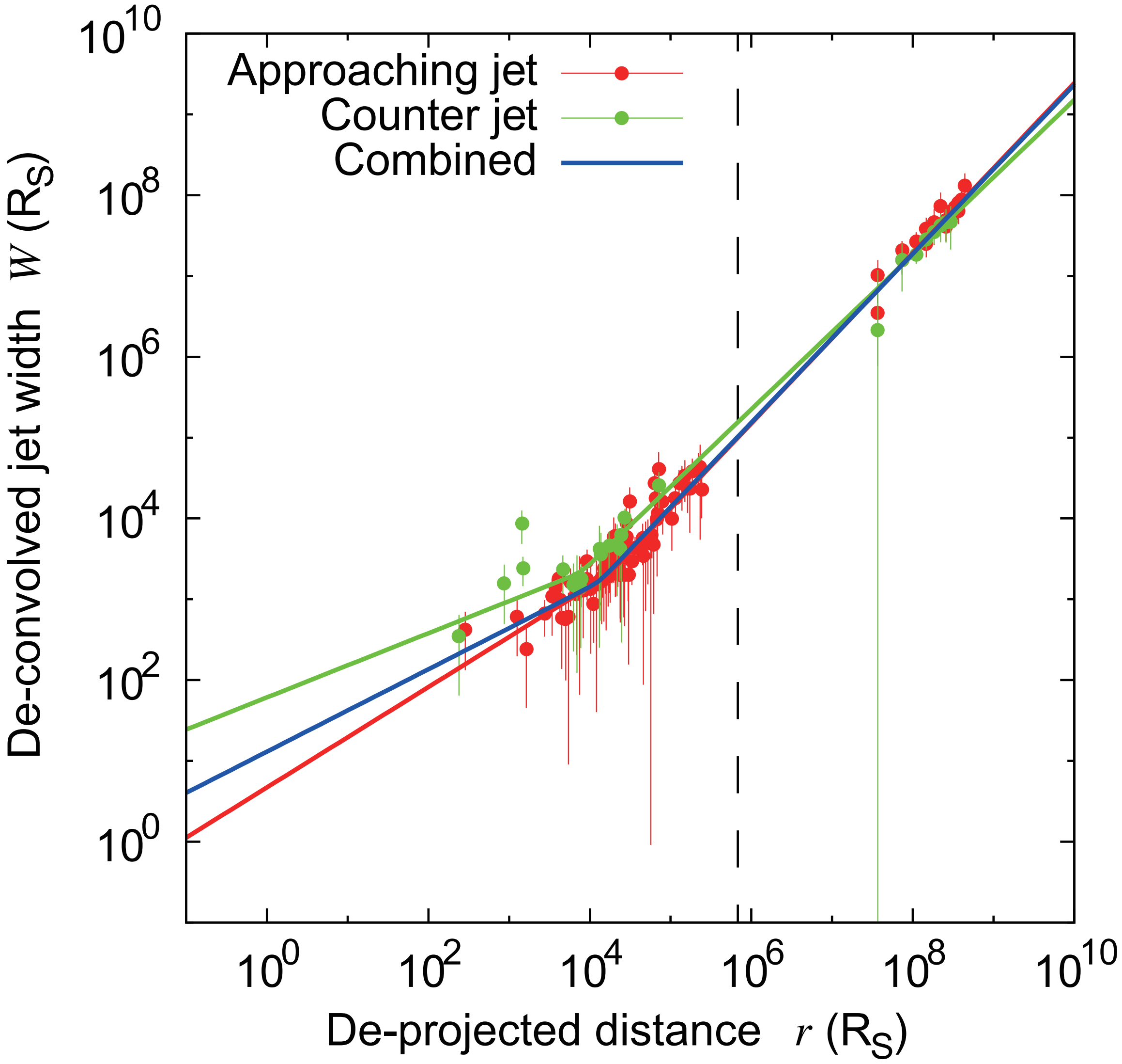

**Figure 2.15:** Comparison between approaching jet and counter jet. The red and green plots describe the measured jet width for approaching and counter sides, respectively. The red, green and blue lines are power-law fitting of the measured jet width profile for approaching side, counter side, and combined data, respectively. The dashed line represents the Bondi radius of NGC 4261.

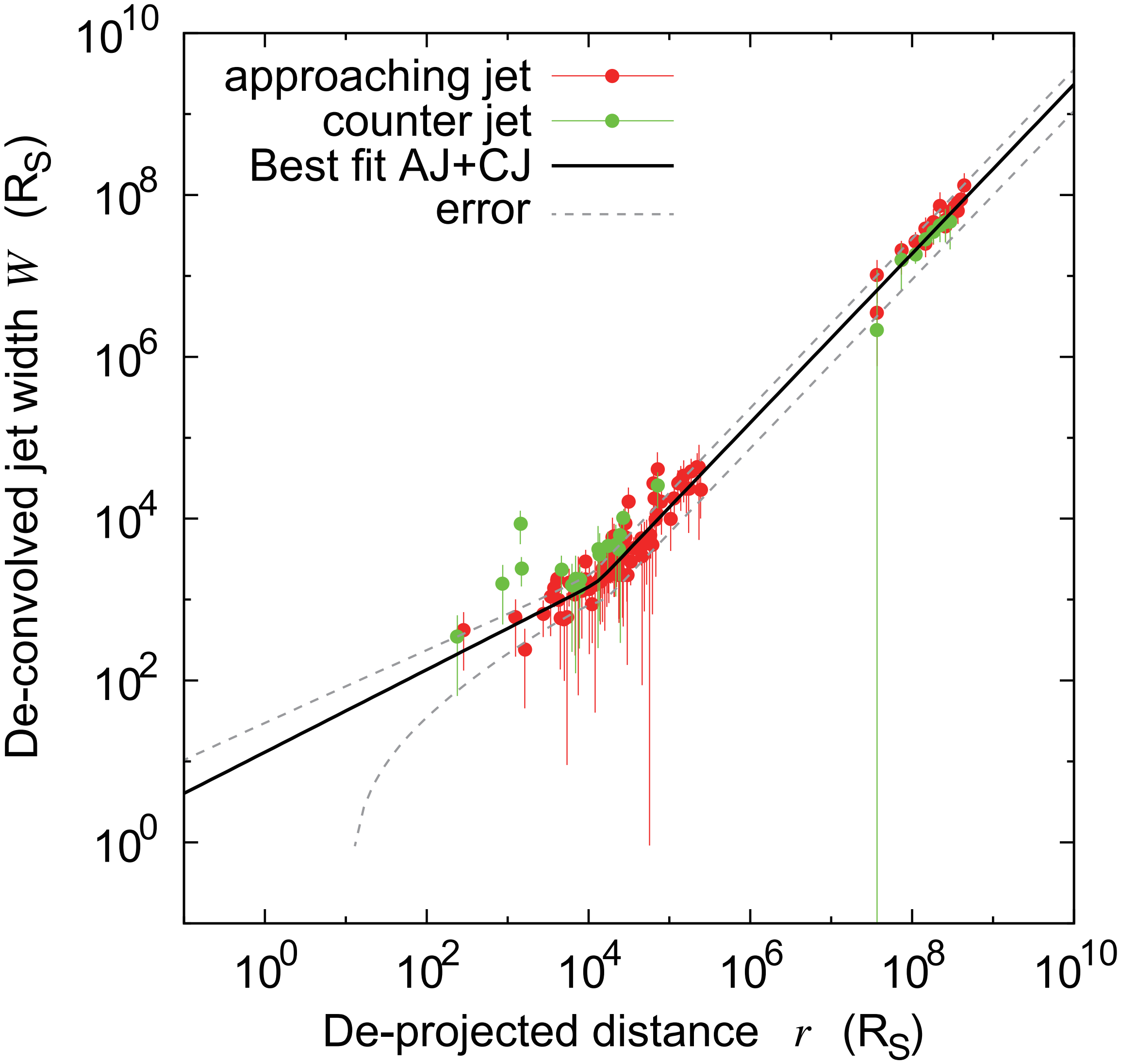

**Figure 2.16:** The broken power-law fitting with errors of jet width profile. The red and green dots describe the jet width for the approaching and counter sides, respectively. The black line describes the best fit of combined data. The dashed line represents the error (1 sigma) of the broken-power law fitting.

**Table 2.2:** Results of Broken Power-law Fit to Jet Structures.

| Case<br>(1) | $W_0$<br>($\times 10^3$ $R_\mathrm{S}$)<br>(2) | $r_\mathrm{b}$<br>($\times 10^3$ $R_\mathrm{S}$)<br>(3) | $a_\mathrm{u}$<br>(4) | $a_\mathrm{d}$<br>(5) | $\chi^2/ndf$<br>(6) |
|---|---|---|---|---|---|
| Approaching jet | $2.0 \pm 0.8$ | $16.1 \pm 6.7$ | $0.62 \pm 0.13$ | $1.05 \pm 0.01$ | 0.464 |
| Counter jet | $2.2 \pm 1.2$ | $7.8 \pm 5.0$ | $0.40 \pm 0.15$ | $0.96 \pm 0.02$ | 0.515 |
| Approaching + Counter jets | $1.7 \pm 0.6$ | $12.9 \pm 4.7$ | $0.51 \pm 0.13$ | $1.05 \pm 0.01$ | 0.570 |

Note. — Col. (1) Cases of fitting analyses; Col. (2) jet width at structural transition; Col. (3) radial distance of structural transition; Col. (4) power-law index of jet structure at upstream; Col. (5) power-law index of jet structure at downstream; Col. (6) reduced chi-square value.

### 2.3.2 Profile of Jet Radiation

Figure 2.17 shows intensity profiles along NGC 4261's approaching jet over VLBA and VLA scales. In this figure, the unit of intensity is Jy beam$^{-1}$; this is the scale used on synthesized images, and it cannot be compared directly among images taken at different frequencies or beam sizes. For the VLBA data, the intensities measured by pixel-based slicing are simply plotted. Intensities lower than $3\sigma$ of image RMS noise are discarded. On the VLA scale, the surrounding radio lobes contaminate the intensity of the jet ridges; therefore, we used the by-product peak intensity determined by double-Gaussian (jet + lobe) fitting on the slice analyses to measure the jet width.

We found significant differences between the profiles at the VLBA and VLA scales. Intensity is steeply decreasing at parsec scales, while nearly flat at the larger scales. Whereas the intensity steeply decreases at the parsec scale, it is nearly flat at larger scales. This indicates the existence of a transition between the VLBA and the VLA scales for which no measurement was available. This profile is quite different from that seen in the jet width profile. We discuss the possibility of a change in physical condition at this transitional scale later in Section 2.4.

Figure 2.18 shows the intensity profiles along NGC 4261's approaching jet using only VLBA results. We initially fitted the results to a single power-law function for each frequency. From these, we found that the power-law indices were systematically divided into two groups; approximately $\propto r^{-2.3}$ for the profiles at 1.4–2.3 GHz, and approximately $\propto r^{-1.6}$ at 5.0–43 GHz. Furthermore, bending signatures seem to occur at roughly $10^4$–$10^5 R_\mathrm{S}$ in the profiles at 2.3 GHz and 5.0 GHz. Based on these characteristics, we again performed fitting with a broken power-law function. However, unlike the broken power-law used for jet width, we performed fitting to intensities at different frequencies using different scaling factors but used common parameters for the break locations and power-law indices of the upper and down streams across frequencies. The resulting power-law indices were approximately $\propto r^{-1.6}$ and $\propto r^{-2.6}$ in the upstream and the downstream regions, respectively. We found a transition at approximately $3 \times 10^4 R_\mathrm{S}$, which is consistent with that seen in the jet width profile ($\sim 2 \times 10^4 R_\mathrm{S}$) for the approaching jet. The significantly lower signal-to-noise ratios in the counter jet prevented a sufficient analysis of its intensity profile.

To obtain radial profiles of jet radiation in a form independent of observing frequency, we calculated the expected flux density, $F'(r)$, per 1 mas at 1 GHz along the approaching jet. At each frequency, we derived the flux density from the intensity using the relation $F_\nu \simeq I_\nu \times \sqrt{\theta^2_\mathrm{SCFmaj} + W^2_\mathrm{jet}}/\theta_\mathrm{SCFmaj}$, as the flux density is defined as the product of intensity and solid angle of emitting region. Furthermore, we corrected the spectral index effects and those arising from changes in convolving size along the jet ($\theta_\mathrm{SCFmin}$). A spectral index should be required and we determined it through the following fitting analysis simultaneously. The fitting function:

$$F'_\mathrm{jet}(r) = F_0 \; 2^{\frac{b_\mathrm{u}-b_\mathrm{d}}{s}} \left(\frac{r}{r_\mathrm{b}}\right)^{b_\mathrm{u}} \left(1+\left(\frac{r}{r_\mathrm{b}}\right)^{s}\right)^{\frac{b_\mathrm{d}-b_\mathrm{u}}{s}}, \qquad (2.2)$$

where $F_0$ is the scale factor, $b_\mathrm{u}$ is the power-law index for the upstream jet, $b_\mathrm{d}$ is the power-law index for the downstream jet, $r_\mathrm{b}$ is the break location, and $s$ is the sharpness of the profile at the break (once again, we used the fixed value $s = 10$). Figure 2.19 shows the fitting result over the range of VLBA scale. We excluded the 43 GHz data from the fitting because the amplitude calibration error at this frequency was significant. The spectral index $\alpha = -0.76$ was found to minimize $\chi^2$. The fitting parameters are given in Table 2.3. The profile has a transition at approximately $2.3 \times 10^4 R_\mathrm{S}$ with power-law indices from $-1.43$ to $-2.5$ in the VLBA scale. The reduced chi square value of this broken power law fitting is 1.002; and the estimated error in Figure 2.20 is indicating that the model describes the data profile well. On the other hand, a single power-law fit resulted in a reduced chi square of 17.21, indicating that this fitting model is not good ($p$-value$\approx 0$). Hence, the detection of the transition in the radiation profile is evident. It is worth noting that the location of transition is consistent with that of the jet width profile. We consider that the identification of the transition in the jet width profile (Section 2.3.1) is significant. Although the profile in the VLA scale is not shown in Figure 2.19, it has a power-law index of $+0.51$ (Table 2.3), which is significantly different from the trend seen in the VLBA scale. This suggests that, as in the case of the intensity profile, a transition of profile between the VLBA and VLA scales is required.

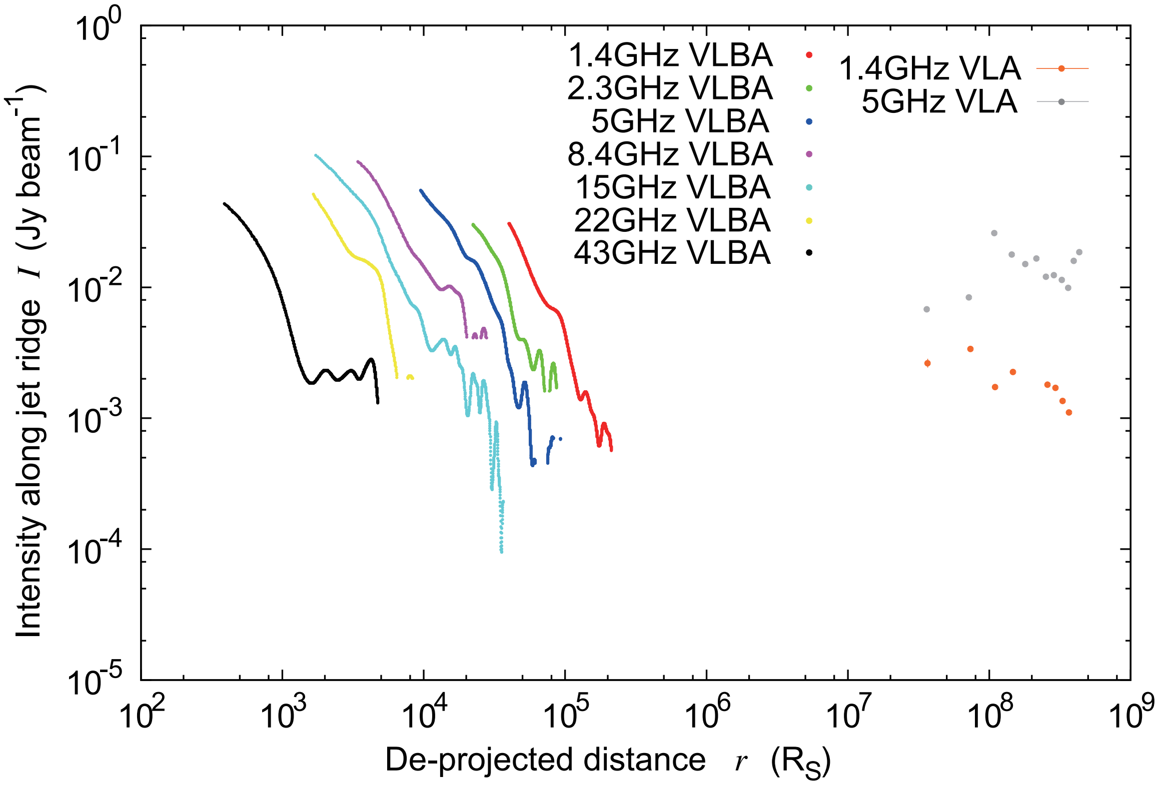

**Figure 2.17:** Measured intensity profiles along approaching jets over all scales. The color variation encodes each observed frequencies; red: 1.4 GHz, green: 2.3 GHz, blue: 5.0 GHz, purple: 8.4 GHz, light blue: 15 GHz, yellow: 22 GHz, black: 43 GHz for VLBA data, and orange: 1.4 GHz, gray: 5 GHz, for VLA data, respectively.

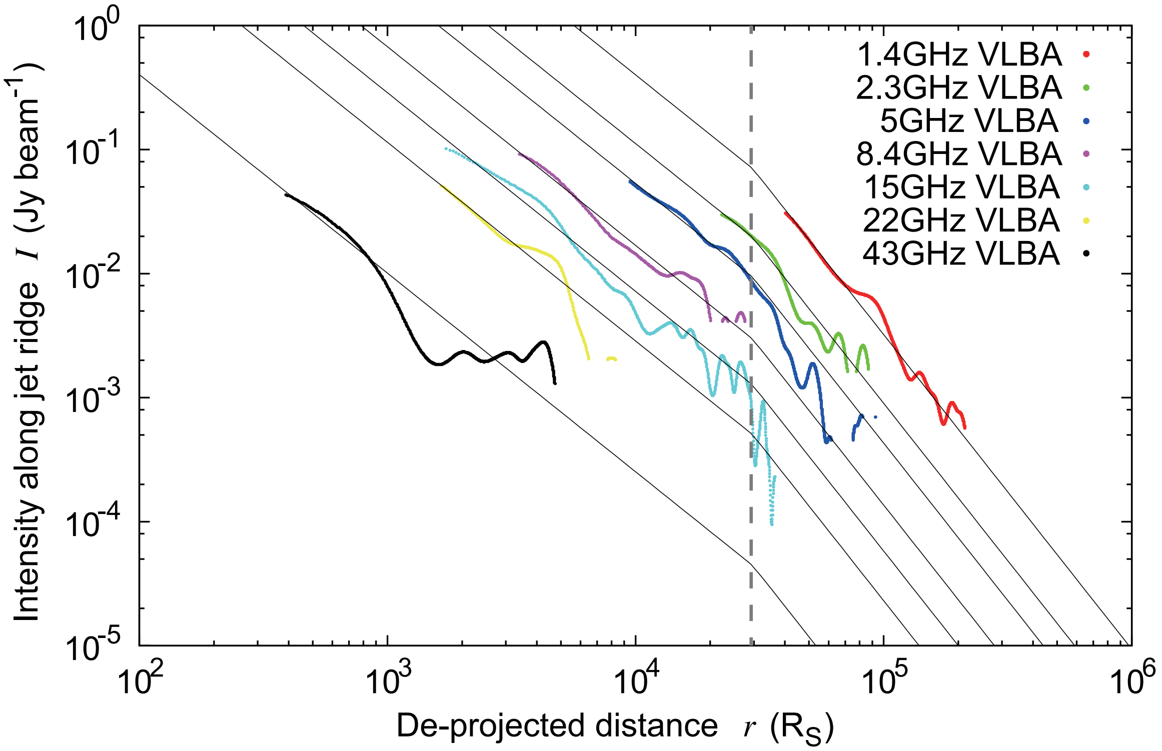

**Figure 2.18:** Intensity profiles along approaching jet in pc scales. The color variation encodes each observed frequencies; red: 1.4 GHz, green: 2.3 GHz, blue: 5.0 GHz, purple: 8.4 GHz, light blue: 15 GHz, yellow: 22 GHz, black: 43 GHz, respectively. The thin black solid lines are the results of simultaneous fitting with a broken power-law model to each frequency using a common break point (shown as a vertical dashed line at $(29.3 \pm 0.4) \times 10^3$ R$_\mathrm{S}$) as a free parameter.

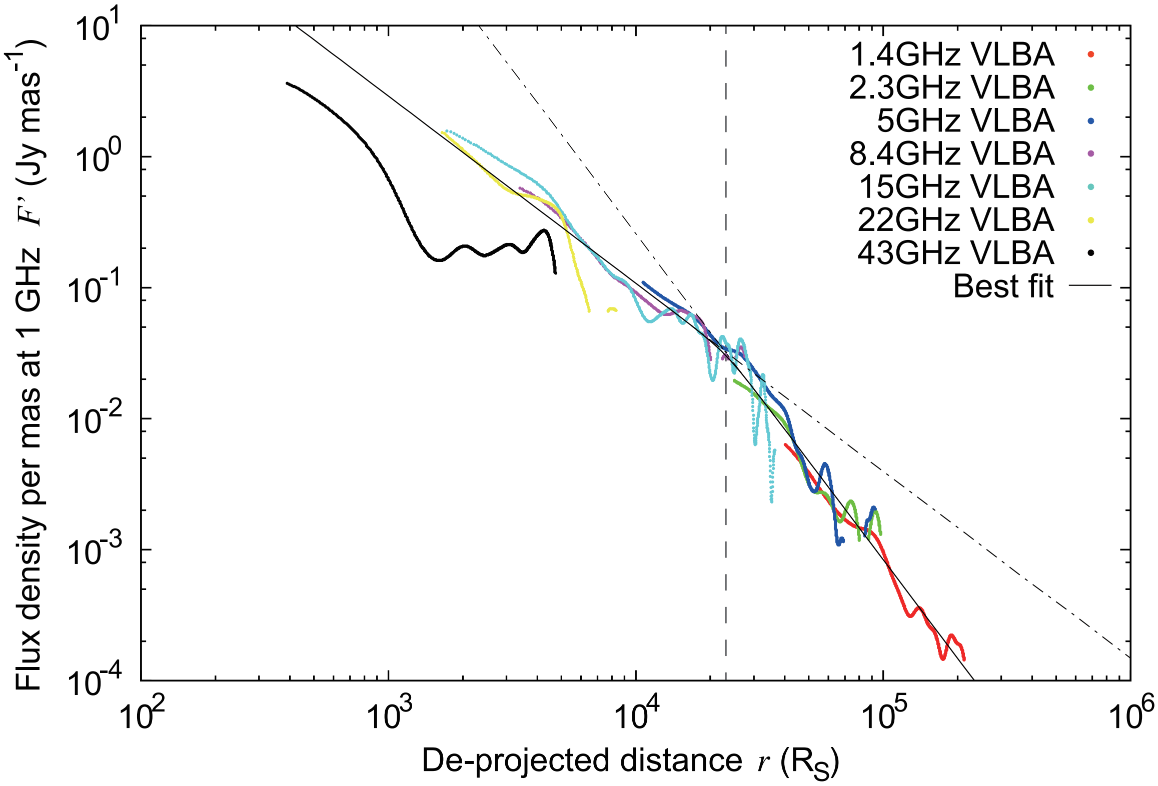

**Figure 2.19:** Expected flux density profiles per mas at 1 GHz along the approaching jet, assuming a spectral index of −0.76 throughout parsec scale jets. The color variation encodes the observed frequencies; red: 1.4 GHz, green: 2.3 GHz, blue: 5.0 GHz, purple: 8.4 GHz, light blue: 15 GHz, yellow: 22 GHz, black: 43 GHz, respectively. The thin black solid line is the result of simultaneous fitting with a broken power-law model and the spectra index to data without 43 GHz. The vertical dashed line at $23.1 \times 10^3$ $\mathrm{R_S}$ represents the break location. The dot dashed lines are the extrapolations of the trends of upper/down streams.

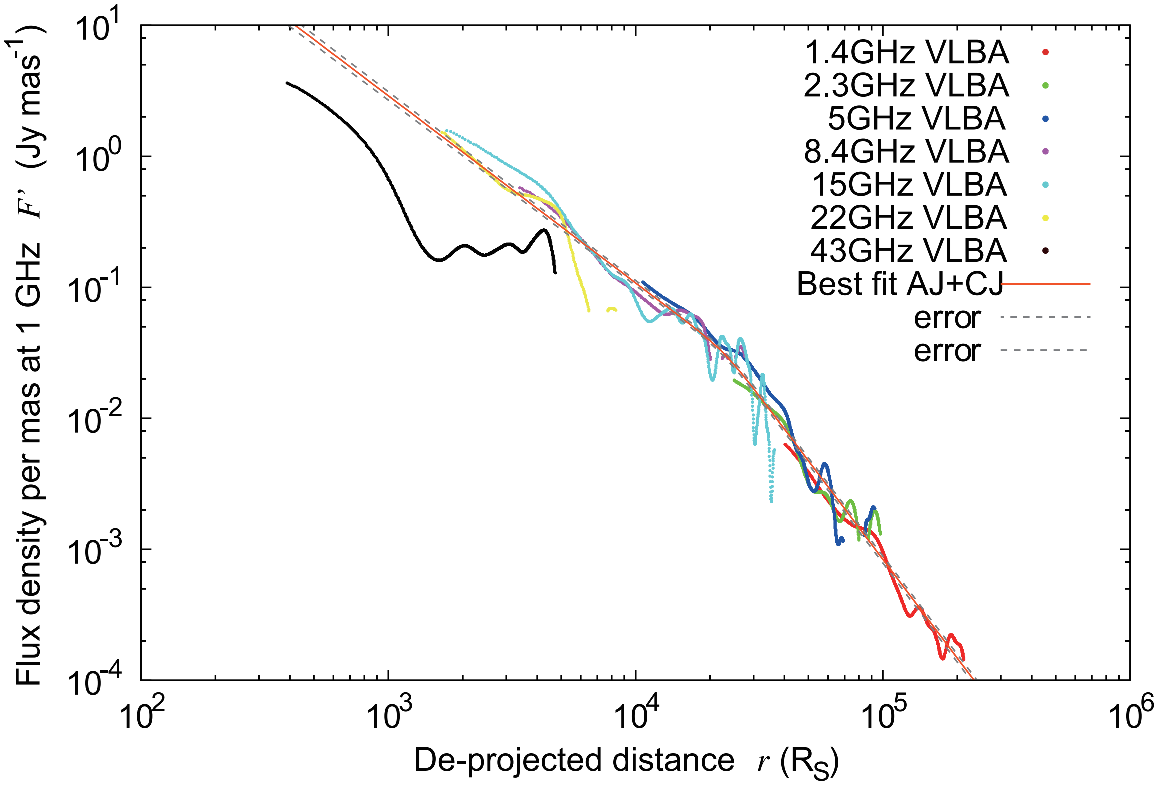

**Figure 2.20:** The error estimate of a broken power-law fitting of flux density profiles per mas at 1 GHz along the approaching jet. The color variation encodes the observed frequencies; red: 1.4 GHz, green: 2.3 GHz, blue: 5.0 GHz, purple: 8.4 GHz, light blue: 15 GHz, yellow: 22 GHz, black: 43 GHz, respectively. The red solid line is the the result of simultaneous fitting with a broken power-law model and the spectra index to data without 43 GHz. The dashed lines are the error estimate of the fitting results.

**Table 2.3:** Results of Power-law Fit to Expected Flux Density at 1 GHz per 1 mas Along approaching Jet

| Case (1) | $F_0$ (Jy mas$^{-1}$) (2) | $r_b^F$ ($\times 10^3$ $R_S$) (3) | $b_u^F$ (4) | $b_d^F$ (5) | $b_{VLA}^F$ (6) | $\alpha$ (7) | $\chi^2/ndf$ (8) |
|---|---|---|---|---|---|---|---|
| $F_{1GHz}$/1mas | $30.3 \pm 1.0$ | $23.1 \pm 0.4$ | $-1.43 \pm 0.02$ | $-2.50 \pm 0.02$ | $+0.51 \pm 0.14$ | $-0.76 \pm 0.01$ | 1.002 |

Note. — Col. (1) Cases of fitting analyses; Col. (2) expected flux density per 1 mas at 1 GHz at profile transition; Col. (3) radial distance of profile transition; Col. (4) power-law index at upstream in parsec scale; Col. (5) power-law index at downstream in parsec scale; Col. (6) power-law index at downstream in VLA scale; Col. (7) spectral index. (8) reduced chi-square value.

## 2.4 Discussion

### 2.4.1 Jet stractural transition of NGC 4261

We found that both the jet width and flux density profiles of the approaching side change at the same scale location of $\sim 10^4 R_{\rm S}$. This consistency (albeit at a statistically marginal level in the jet width findings) leads us to conclude that there is a physical change in conditions in the NGC 4261 jets that causes the transition. We found that the counter jet width profile also has a parabolic-to-conical structural transition at the same scale as seen on the approaching side.

### 2.4.2 Comparison with other Active Galactic Nucleus Jets

Figure 2.21 shows a comparison of our results with previous studies on M87 (Asada & Nakamura 2012) and NGC 6251 (Tseng et al. 2016). The M87 jet has a parabolic shape ($a \sim 0.6$) upstream and a conical expansion ($a \sim 1$) downstream, with the structural transition occurring at a distance scale of approximately $2.5 \times 10^5 R_{\rm S}$, which is close to the Bondi accretion radius ($3.8 \times 10^5 R_{\rm S}$; Allen et al. 2006). The NGC 6251 jet also has a structural transition from parabolic to conical at around $2 \times 10^5 R_{\rm S}$, which is close to the boundary of the sphere of gravitational influence (SGI[4], $\sim 5 \times 10^5 R_{\rm S}$). Thus, NGC 4261 is the third observational example of a structural transition from parabolic to conical shape. However, it is worth noting that the transition in NGC 4261 is at $\sim 10^4 R_{\rm S}$, which is not close to the Bondi radius (34±8 pc[5] (Balmaverde et al. 2008), corresponding to $6.9 \times 10^5$ $\rm R_s$), unlike in M87 or NGC 6251. The case of NGC 4261 therefore indicates that a transition close to the Bondi radius is not universal among AGNs. Furthermore, the jet width of NGC 4261 appears to be one order of magnitude larger than those in M87 and NGC 6251. Hence, we consider the following error budget. The horizontal axis in units of Schwarzschild radius can deviate by ∼ 3%, corresponding to 0.01 order of magnitude, as a result of a 5% formal error in the estimate of the inclination angle. The black hole mass estimate includes a 20% measurement error, which affects both the horizontal and vertical scales by 0.1 order of magnitude. The data for M87 and NGC 6251 would also be expected to contain the same types of errors. Thus, in assessing the relation between the NGC 4261 profiles

---

[4] Consequently, the Bondi radius is expected to be close to the SGI. See descriptions in Tseng et al. (2016).

[5] Although the Bondi radius of NGC 4261 was reported as 32 pc in the original paper, it was calculated from an assumed black hole mass of $5.2 \times 10^8 M_{\rm odot}$, a different value from that used in this paper. Thus, we adopt $34 \pm 8$ pc as the Bondi radius based on the black hole mass used in this paper, a propagated black hole mass measurement error 20%, and a 4% gas temperature decision error in X-ray observation.

and its Bondi radius, there is a 0.2 order of magnitude uncertainty on the horizontal axis scale, an error budget that does not affect the conclusion that the jet structural transition location of NGC 4261 is not close to the Bondi radius. At the same time, the significantly larger observed jet width in NGC 4261 than in M87 or NGC 6251 is presumably real. We show the result for Cyg A (Boccardi et al. 2016b, in which a jet width similar to NGC 4261 is observed), in Figure 2.21. The differences in width among the respective cases are attributable to inclination: NGC 4261 and Cyg A are highly inclined and have two-sided jets, while the jets of M87 and NGC 6251 are viewed at small inclination angles and are apparently one-sided. In the case of spine–sheath structured jets (Ghisellini et al. 2005), an outer-layer flow with a sub-relativistic speed would be observed in a highly inclined AGN, while an inner relativistic flow would be seen in an AGN viewed at a small inclination angle.

This study of NGC 4261 represents double-sided structural transition of jet width profile. The results suggest that the phenomenon is related to the global state of the circumnuclear environment and/or the AGN jets themselves rather than a local condition.

Thus, it is important to study the case of NGC 4261 in more details. The present study includes the measurement of radial profile for the flux density along the jet, which is expected to probe the evolution of radiative condition along the jet. By using the both of the jet width profile and the flux density profile, and the synchrotron theory in the assumption of the equipartition condition between the particles and magnetic field, we investigate following physical conditions of NGC 4261 jet later in Chapter 5: the synchrotron luminosity per unit volume, the synchrotron luminosity per unit jet length, the magnetic field, and the jet pressure.

## 2.5 Summary and Conclusions

In this Chapter, we presented new measurements based on VLBA and VLA images of jet width and radiation profiles along AGN jets in NGC 4261 over the range $10^3$–$10^9 R_\mathrm{S}$.

Although the result was statistically inconclusive, a parabolic-to-conical transition signature was inferred at $\sim 10^4 R_\mathrm{S}$ along both the approaching and counter jet width profiles corresponding to power-law index changes from $0.62 \pm 0.13$ to $1.05 \pm 0.01$ and from $0.40 \pm 0.15$ to $0.96 \pm 0.02$, respectively. A transition in the radiation profile at approximately the same distance was also found on the approaching jet, with the power-law indices changing from $-1.43 \pm 0.02$ to $-2.50 \pm 0.02$ at $\sim 2 \times 10^4 R_\mathrm{S}$. The radiation profile of the counter jet was not investigated owing to its lower signal-to-noise ratio.

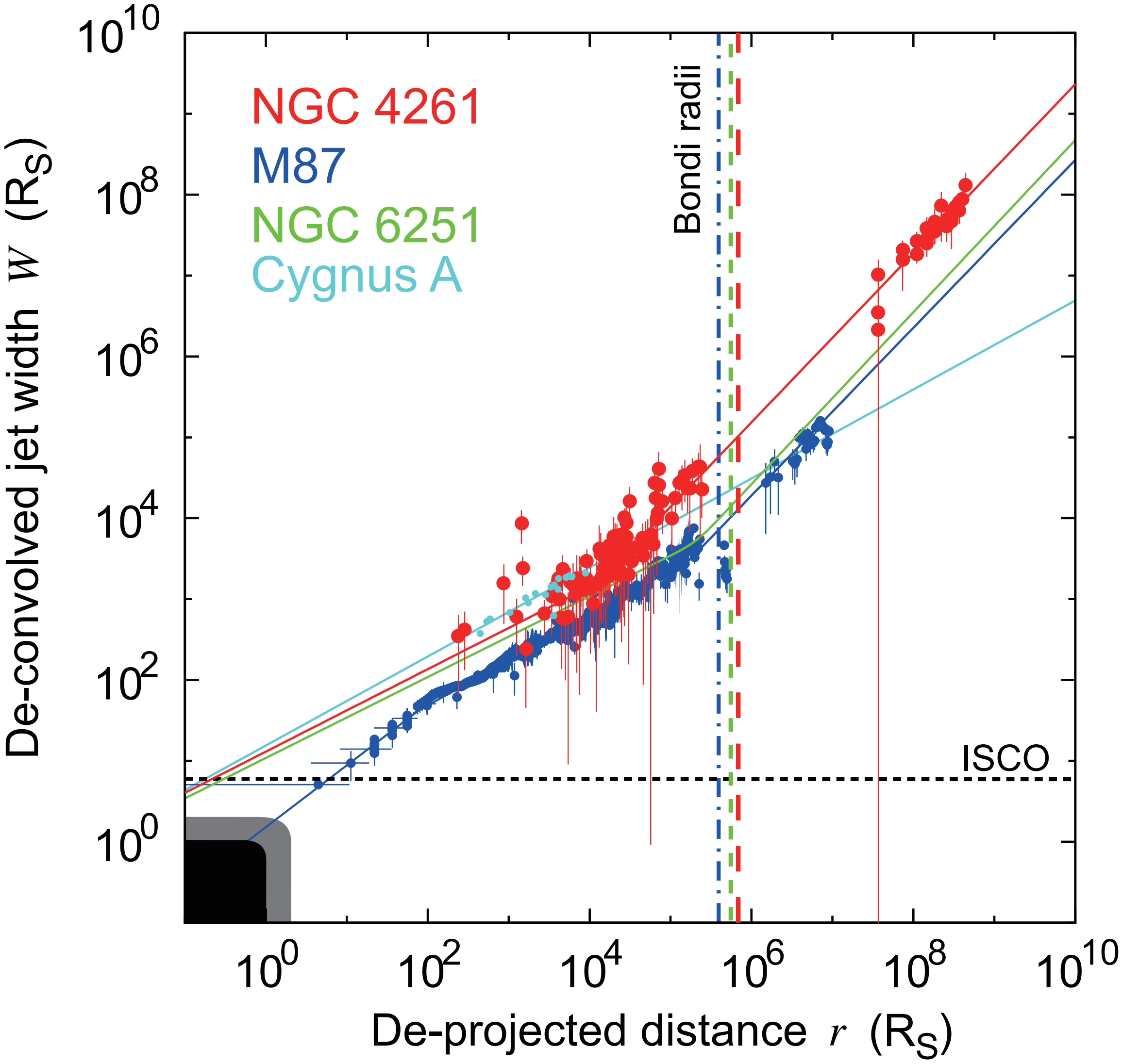

**Figure 2.21:** Comparisons with M87 and NGC 6251. Red, blue, green, and cyan plots are the radial profiles of measured jet widths of NGC 4261 (this work), M 87 (Hada et al. 2013; Asada & Nakamura 2012), NGC 6251(Tseng et al. 2016), and Cygnus A(Boccardi et al. 2016b), respectively (only a fitted line is given for NGC 6251). The black and gray area represent event horizon's surfaces for maximally spinning and non-spinning black holes, respectively. The dotted line shows the the inner stable circular orbit, which corresponds to ~ $6R_\mathrm{S}$ in diameter, as a guide for the innermost region of accretion disk/flow.

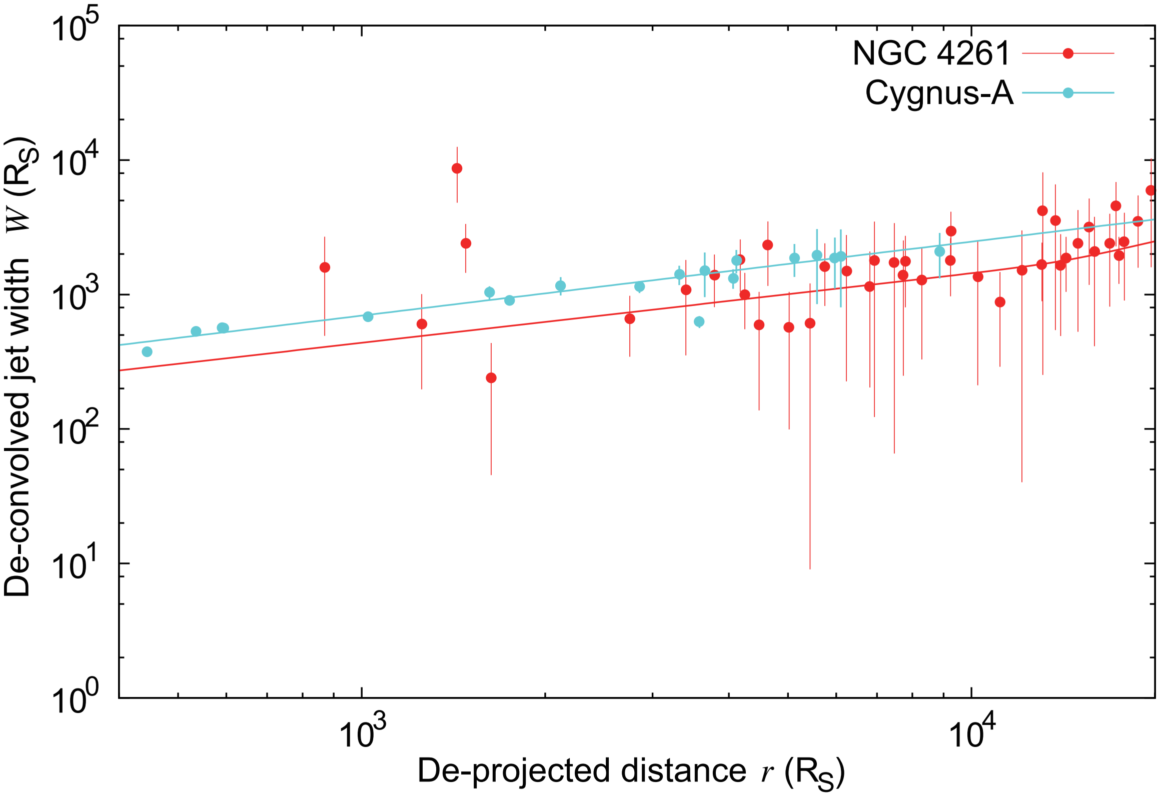

**Figure 2.22:** Comparisons with Cyg A. Red and cyan plots are the radial profiles of measured jet widths of NGC 4261 (this work) and Cygnus A(Boccardi et al. 2016b), respectively.

These transitions at nearly the same locations in the jet width and radiation profiles imply a change in physical conditions in the NGC 4261 jets at this site. Thus we consider that NGC 4261 represents the third observational example, after M87 and NGC 6251, of a structural transition from a parabolic to a conical shape.

Another transition was detected in the radiation profile at a distance of $\sim 3\times10^6 R_{\rm S}$ in the region of conical flow, based on significant differences in the profile indices derived from the VLBA and VLA ranges. This change reflects a jet enhancement in the outer region, with the jet kinetic energy being dissipated upon impact with the radio lobe.

We estimated a jet pressure profile based on an assumption of equipartition between particles and magnetic field. The consistency of out results with the X-ray-based hot gas pressure estimates observationally supports a balance of the jet pressure with that of the surroundings.

# Chapter 3

# NGC 1052

**Abstract** We investigated the radial profile of jet width in the nearby radio galaxy NGC 1052 at radial distances between $\sim 10^3$ and $10^9$ Schwarzschild radii on both their approaching and counter jet sides. The transverse width of jets was measured in images obtained with the VLBI Space Observatory Programme (VSOP), the Very Long Baseline Array (VLBA), and the Very Large Array (VLA). The jet-width profile of counter jets are apparently consistent with that of approaching jets throughout the measuring ranges, indicating symmetry continues up to intragalactic scale. We found a signature of interstellar broadening, which makes an observed radio size larger with a squared dependency of wavelength, toward the nuclear region of NGC 1052. It is the first time that the interstellar broadening is discovered around a supermassive black hole in extragalactic source, while the phenomenon has been known only toward the Galactic centre of Sgr A* and background radio sources of the Milky Way. The power-law index of the jet-width profile apparently shows a transition from an index of 0.03 to 0.92 at a radial distance of $\sim 1 \times 10^4$ $\mathrm{R_S}$, even at high frequencies, where the interstellar broadening should be negligible. The very small power-law index in inner jets is reminiscent of the previously observed inner jets in 3C 84. Both the nuclei of NGC 1052 and 3C 84 are confined by dense plasma torii of accreting matter onto their black holes.

## 3.1 Introduction

The structure of astrophysical jet in active galactic nuclei (AGNs) is considered to play an important role in the mechanism of accelerating the jet plasma flow in interstellar/intragalactic medium. The radial profile of the measured transverse widths of the jet in the nearby radio galaxy M87 exhibits a parabolic structure between a few hundred and $10^5$ Schwarzschild radii ($R_\mathrm{S}$) from the central engine (Asada & Nakamura 2012). The region at which the jet acceleration is observed by monitoring observations (Nakamura & Asada 2013; Mertens et al. 2016, e.g.,) coincides with that of the parabolic streamline (Asada et al. 2014). The parabolic structure continues roughly up to the sphere of gravitational influence of the central black hole and is ended with a transition into a conical downstream. Similar properties with a parabolic-to-conical transition at similar scales (typically $\sim 10^5 R_\mathrm{S}$) have also been found in NGC 6251 (Tseng et al. 2016) and NGC 4261 (Nakahara et al. in press). These results are thought to be observational evidence that a transverse pressure supports by the external medium with a relatively shallow radial dependence in the core regions of galaxies and that magnetic energy is dissipated into kinetic energy until they roughly reach comparable as suggested by studies of numerical simulations (e.g., Komissarov et al. 2009). On the other hand, a parabolic jet structure continues at least up to $\sim 10^8 R_\mathrm{S}$ without a transition to a conical structure is also suggested for the jets in Cygnus A (Nakahara et al. in preparation). Such results can be obtained by measurements over very wide physical scales beyond $\sim 10^5 R_\mathrm{S}$ by using both the very-long-baseline interferometry (VLBI) and connected array to cover the angular scales of interest for nearby radio galaxies. However, the number of samples investigated over such wide scales has been insufficient to establish the universality of the evolution of jet structure in AGNs.

NGC 1052 is a nearby ($z = 0.005037 \pm 0.000020$; Denicoló et al. 2005) radio galaxy whose nuclear activity is classified as low-ionization nuclear emission-line region (LINER). A well-defined double-sided radio jets elongated by several parsecs with a position angle of 65 deg. Kpc-scale jet–lobe structures are also prominent on the both sides in the VLA image at 1.4 GHz (Wrobel & Heeschen 1984). However, in the VLA image at 5 GHz the central core dominates against weak two-sided radio emissions (Jones et al. 1984). NGC 1052 shows a convex radio spectrum peaked at roughly 10 GHz, to be classified into the GHz-Peaked Spectrum (GPS) radio source (O'Dea 1998). The GPS radiation originates in the central core, which constitutes of pc-scale jets. VLBI observations revealed the presence of water masers that distribute along the pc-scale jets. The water masers were considered to be excited by shocks into circumnuclear molecular clouds, or amplification of the radio continuum emission of the jet by foreground molecular clouds (Claussen et al. 1998). On the other hand, the detailed profile of free–free absorber toward the nuclear region had been investigated and suggests the presence of a surrounding plasma torus with a radius of $\sim 0.5$ pc around the nucleus (Kameno et al. 2001, 2003). The location of large-opacity free–free absorption coincides with the distribution of water masers (on the both jet sides), all of which is redshifted by 50–350 km $\mathrm{s}^{-1}$ with respect to the systemic velocity of NGC 1052 (Sawada-Satoh et al. 2008). They argue that the masers in NGC 1052 are associated with gas in a circumnuclear torus or disk, which is accreting onto the central engine. Thus, NGC 1052 is one of well-investigated nearby radio galaxies with apparent two-sided jets. However, it has never been studied in terms of the evolution of jet width.

In the present paper, we report the measurements of the radial profiles of jet width for NGC 1052. At the distance of 20 Mpc to NGC 1052, an angular resolution of 1 mas is equivalent to a linear scale of $\sim 0.095$ pc. Assuming an inclination of 86 deg (Baczko et al. 2016), 1 mas is equivalent to $\sim 6,400\ R_{\mathrm{S}}$, given the mass of the central black hole $10^{8.19}\ M_{\odot}$ (Woo & Urry 2002). We uncover the structure of jets over a range of $\sim 500$ to $4 \times 10^{7} R_{\mathrm{S}}$ in distance from the central engine of NGC 1052 on both the approaching and counter jets. The present paper is structured as follows. In Section 3.2, the VLA and VLBI data we used in the present paper and image analysis for jet-width measurements are described. In Section 3.3, we present the results of the jet-width profiles. In Section 3.4 we make brief discussion of the jet structure and its physical origin. Finally, our study is summarized in Section 3.5.

## 3.2 Data and Image analysis

### 3.2.1 VSOP data

We used space VLBI images obtained in the VLBI Space Observatory Programme (VSOP; Hirabayashi et al. 2000) at 1.6 GHz (observation code: W513A) and 4.8 GHz (W513B), which have already been published by Kameno et al. (2003). The observations were carried out on August 7 and July 31, 2001, respectively. Left-hand circular polarization was received with a bandwidth of 32 MHz. The spacecraft HALCA was linked to two tracking stations during each observation: Green Bank and Tidbinbilla for W513A, Green Bank and Usuda for W513B. The ground telescopes were the 10 antennas of the Very Long Baseline Array (VLBA). We remade an image at each frequency with a restored circular beam, as shown in Table 3.1; the size of the restored beam was determined by the geometric mean of the major and minor axes for the original synthesized (elliptical) beam. Figure 3.1 and 3.2 show the VSOP images.

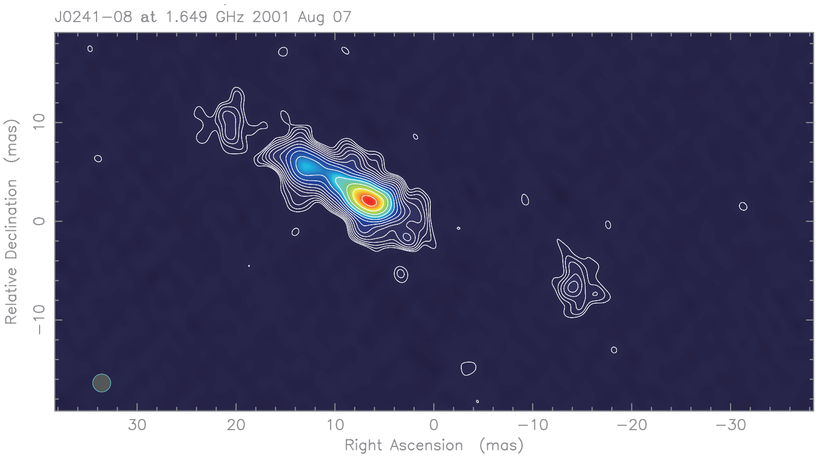

**Figure 3.1:** Radio image of NGC 1052 at 1.6 GHz VSOP. Contours start from the 3 sigma image RMS noise and increase by factors of $\sqrt{2}$

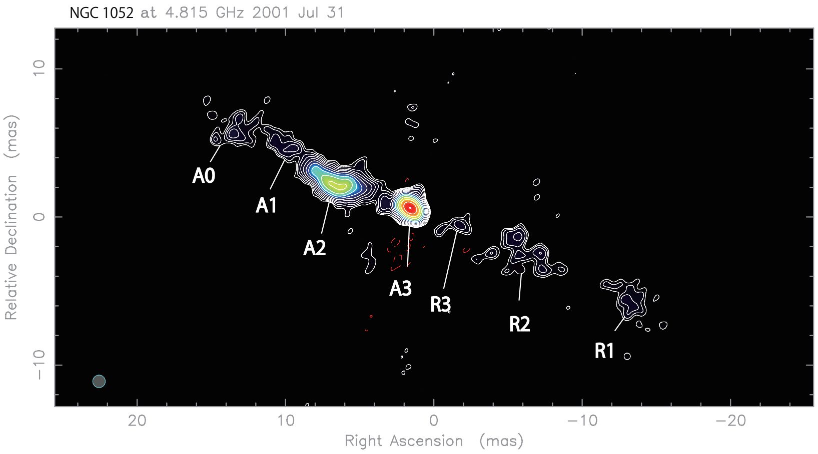

**Figure 3.2:** Radio image of NGC 1052 at 4.8 GHz VSOP. Contours start from the 3 sigma image RMS noise and increase by factors of $\sqrt{2}$

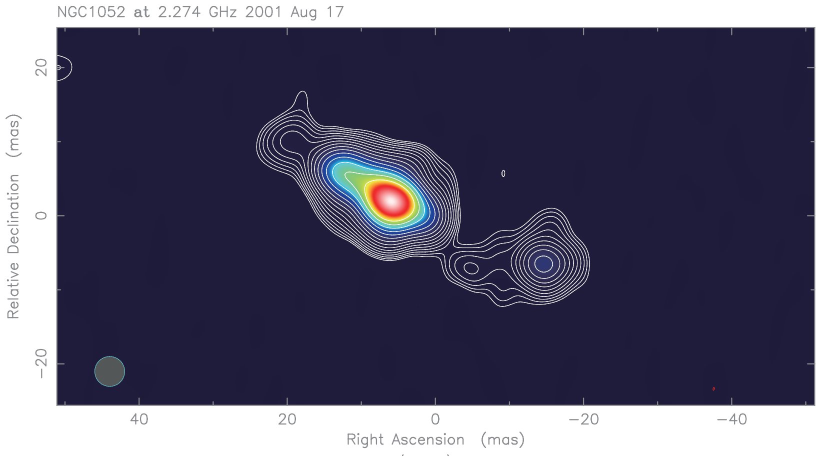

**Figure 3.3:** Radio image of NGC 1052 at 2.3 GHz VLBA. Contours start from the 3 sigma image RMS noise and increase by factors of $\sqrt{2}$

### 3.2.2 VLBA data

To obtain the innermost region of the jets in NGC 1052, I used the same data sets that have already presented by Sawada-Satoh et al. (2008) and Kameno et al. (2003). NGC 1052 were observed using VLBA at 2.3/8.4/15.4 GHz on 17 August 2001 (Kameno et al. 2003), and at 15.4/22.1/43.2 GHz on 24 July 2000 (Sawada-Satoh et al. 2008). More details of the observations and the data reduction processes are described in Sawada-Satoh et al. (2008) and Kameno et al. (2003). The natural weighting image was adopted at 15.4/22.1/43.2 GHz for measuring the hazy spreading jet structure; while the uniform waiting image was adopted at 22.1/43.2 GHz for measuring the compact innermost structure of jets taking advantage of the high spatial resolution. We restored the imaging beam size for circular beam represented in table 3.1 which was geometric mean of synthesized elliptical beam. Figures 3.3–3.8 show the VLBA images.

### 3.2.3 VLA data

The VLA data set AR0396 was retrieved from the data archive system of the National Radio Astronomy Observatory (NRAO). We chose the data which has the longest on-source time (33.85 ksec) to NGC 1052 in the VLA archive. The observation was conducted on 20 June 1998 at 8.270 GHz in the X-band using the VLA A-array configuration. Dual-circular polarization was received, with a bandwidth of 25 MHz. The data reduction procedures follow standard manners for VLA data using `AIPS`

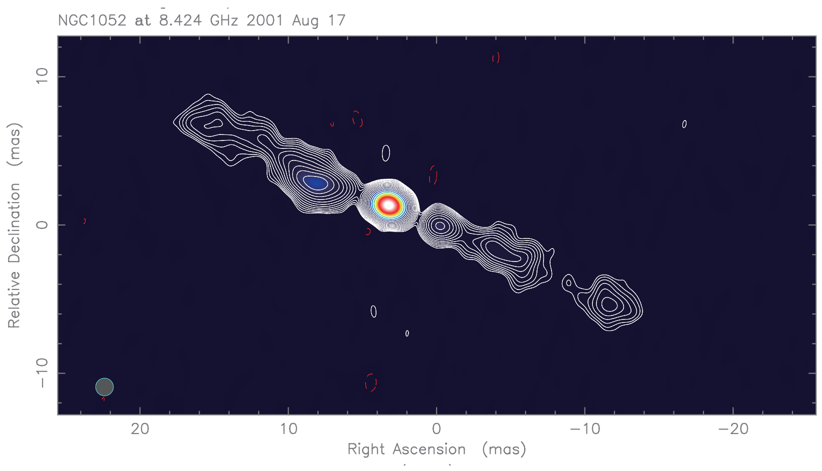

**Figure 3.4:** Radio image of NGC 1052 at 8.4 GHz VLBA. Contours start from the 3 sigma image RMS noise and increase by factors of $\sqrt{2}$

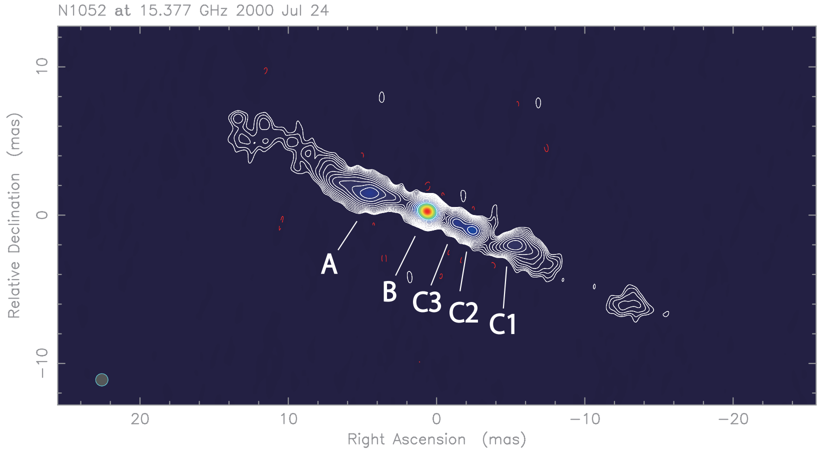

**Figure 3.5:** Radio image of NGC 1052 at 15.4 GHz VLBA which was observed on July/24/2000. Contours start from the 3 sigma image RMS noise and increase by factors of $\sqrt{2}$

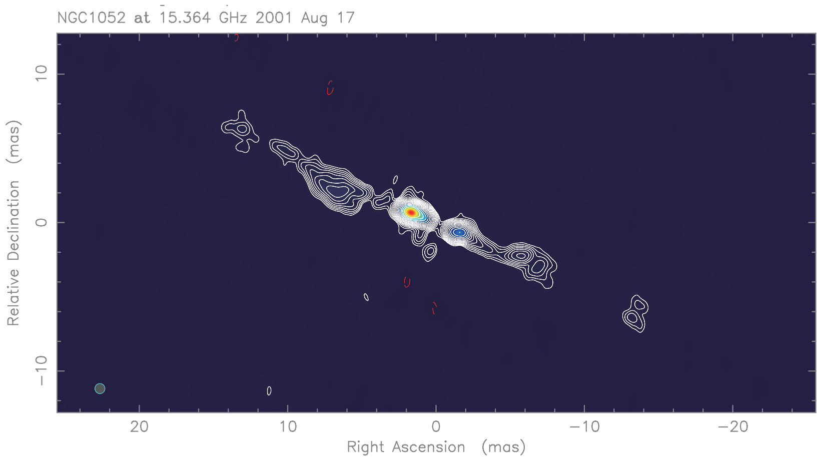

**Figure 3.6:** Radio image of NGC 1052 at 15.4 GHz VLBA which was observed on August/17/2001. Contours start from the 3 sigma image RMS noise and increase by factors of $\sqrt{2}$

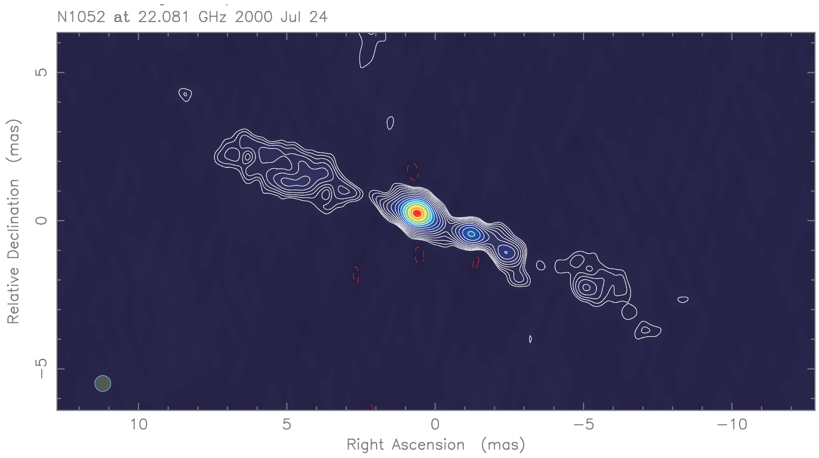

**Figure 3.7:** Radio image of NGC 1052 at 22.1 GHz VLBA. Contours start from the 3 sigma image RMS noise and increase by factors of $\sqrt{2}$

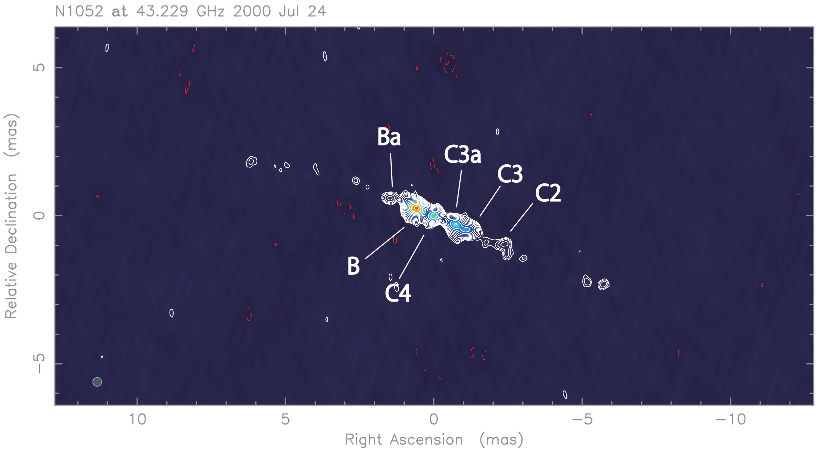

**Figure 3.8:** Radio image of NGC 1052 at 43.2 GHz VLBA. Contours start from the 3 sigma image RMS noise and increase by factors of $\sqrt{2}$

(Astronomical Image Processing System). Data of the antennae 3, 7, 9, 19, and 27 were flagged because their system noises were apparently strange. We performed CLEAN deconvolution using `Difmap` software for image construction. The image was made with natural weighting and a restored circular beam of 0.6-arcsec diameter, which was the geometric mean of original elliptical of synthesized beam. The image is shown in Figure 3.9.

### 3.2.4 Determination of the central engine location

Radio emission from the nuclear region of NGC 1052 suffers strong free–free absorption (FFA; Kameno et al. 2001, 2003; Kadler et al. 2004; Sawada-Satoh et al. 2008). Kameno et al. (2003) proposed that a parsec-scale circumnuclear torus consisting of cold dense plasma is responsible for observed convex radio continuum spectra due to FFA. Therefore, there is frequency dependence in the apparent position of the upstream end in the jet. To determine the position of the central engine, it is necessary to measure the core shift. Kadler et al. (2004) tried core shift measurement, but it was not so conclusive. It may be suggesting that the geometry as a free-free absorber of dense plasma torus is not so simple, in addition the blobby structure of the jet is possibly affecting. Kadler et al. (2004) concludes that the central engine is most likely to be present around 0.03 pc between the specific two components of the 43 GHz image.

Alternatively, there is a method that the ejection point of the approaching and counter jets on the basis of their proper motions is regarded as the central engine

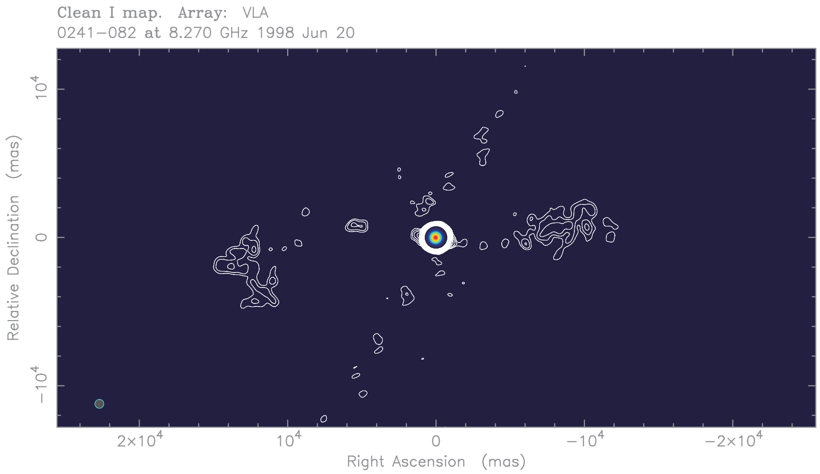

**Figure 3.9:** Radio image of NGC 1052 at 8.3 GHz VSOP. Contours start from the 3 sigma image RMS noise and increase by factors of $\sqrt{2}$

**Table 3.1:** Image performance of NGC 1052

| Telescope<br>(1) | $\nu$ (GHz)<br>(2) | Obs. date (Jy/beam)<br>(3) | $\sigma$ (mJy/beam)<br>(4) | $\theta_{\mathrm{beam}}$ (mas)<br>(5) |
|---|---|---|---|---|
| VSOP | 1.649 | 2001-08-07 | 2.53 | 1.82 |
| | 4.815 | 2001-07-31 | 3.84 | 0.85 |
| VLBA | 2.274 | 2001-08-17 | 1.83 | 4.04 |
| | 8.424 | 2001-08-17 | 1.68 | 1.20 |
| | 15.377 | 2001-08-17 | 1.11 | 0.83 |
| | 15.364 | 2000-07-24 | 1.55 | 0.68 |
| | 22.081 | 2000-07-24 | 3.75 | 0.54 |
| | 43.229 | 2000-07-24 | 2.74 | 0.30 |
| VLA | 8.27 | 1998-06-20 | 0.19 | 601 |

Columns are as follows: (1) Telescope; (2) Frequency; (3) Observation date; (4) Image RMS noise; (5) The restored synthesized beam size.

position. This method uses only simple kinematics. The present study adopts to determine the location of the central engine in the latter way. The proper motions of approaching jet and counter jet of NGC 1052 have intensively been measured at 15 GHz, 15 GHz, and 43 GHz by Vermeulen et al. (2003); Lister et al. (2013), and Baczko et al. (2016), respectively. Apparent velocity for each blob shows variation in some levels. We averaged the jet velocities reported in table 2 of Vermeulen et al. (2003), and obtained $0.0781 \pm 0.0022$ pc $\mathrm{yr}^{-1}$ for approaching jets, $0.0783 \pm 0.0037$ pc $\mathrm{yr}^{-1}$ for counter jets. Therefore, the position to divide the distance between approaching jet and counter jet components into 0.0781:0.0783 is considered to be the putative location of the central engine.

Before estimations for the location of central engine, we superimposed images of different frequencies. The positions of all jet components were determined using `AIPS JMFIT` task on all VLBA and VSOP images. Identified components were labeled as shown in Figures 3.2, 3.5 and 3.8. Subsequently, we made pattern matching among the distributions of determined positions at different frequencies in the same manner presented in Kameno et al. (2003); Sawada-Satoh et al. (2008). Because the data of Kameno et al. (2003) and Sawada-Satoh et al. (2008) were obtained at different epochs, jet structures changed. Hence, we made pattern matching for the multi-frequency images of these two groups separately.

Next, we presumed to make pairs of an approaching and a counter jet component. The highest FFA opacities with two-sided tails were located at the point between A1–R1 (Kameno et al. 2003) and near the component C4 (Sawada-Satoh et al. 2008). Therefore, the defined pairs are A1–R1, A2–R2, A3–R3 for the epoch 2001 summer, B–C3a, A–C1, Ba–C3 for the epoch July 24, 2000 at each frequency in the present study. The separations between a pair was divided into 0.0781 and 0.0783 for the pairs of A3–R3, A2–R2, Ba-C3, and B-C3a, which are located at a relatively inner region. Finally, we determined the position of black hole by weighted means for the two epochs separately with uncertainty to 22 $\mu$arcsec and 13 $\mu$arcsec for the epoch 2001 summer and the epoch July 24, 2000, respectively (Figures 3.10 and 3.11).

### 3.2.5 Jet width measurements

I have done the jet width measurements by using almost the same way as NGC 4261 jet. NGC 1052 jet also shows a single ridge structure extending almost in the east-west direction (position angle $PA \approx 65$ deg). Thus, the images were rotated by 25 deg counterclockwise to make the mean jet axis being parallel to the horizontal axis, and sliced pixel-by-pixel along the transverse direction of jet without the lobe component in VLA data. The transverse intensity profile of each slice were fitted with a Gaussian model profile such like NGC 4261. Details are described in Section 2.2.2.

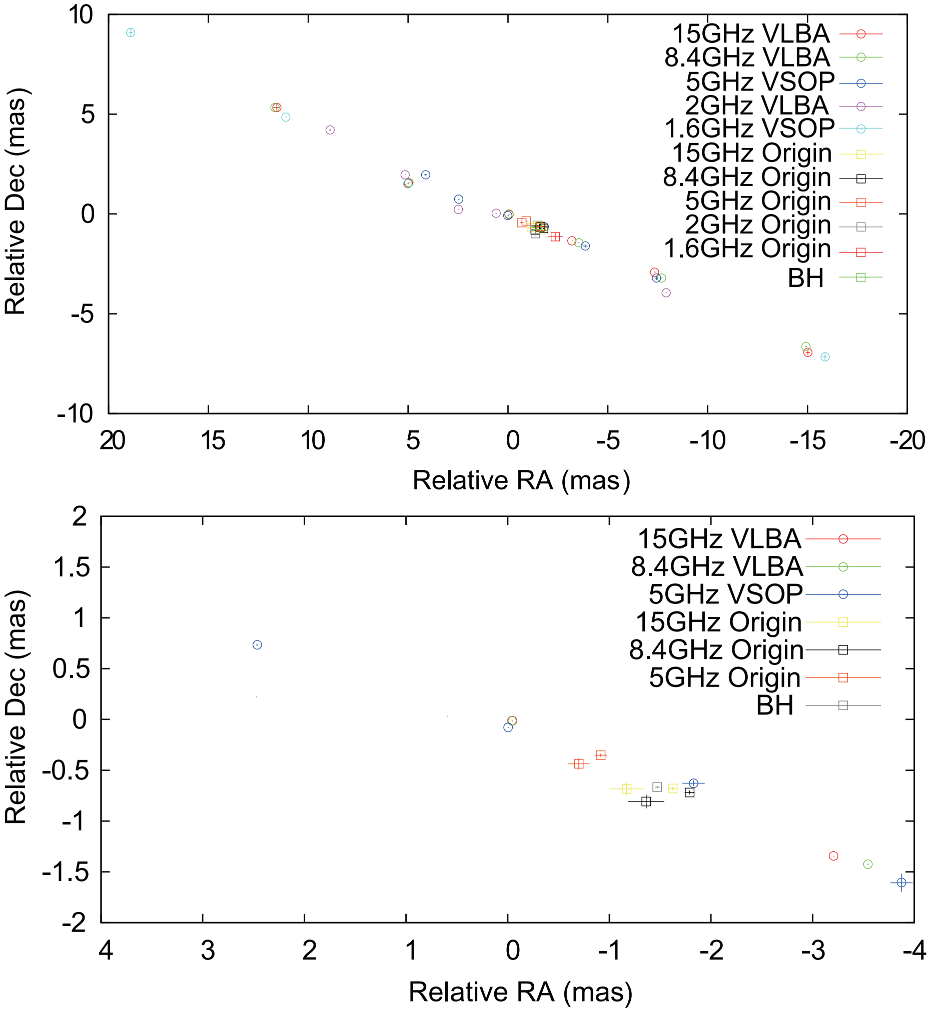

**Figure 3.10:** JMFIT results of NGC 1052 at 1.6/2.3/5/8.4/15 GHz. Data sets are the same as Kameno et al. (2003). (Top) Whole region. (Bottom) Focused on central region.

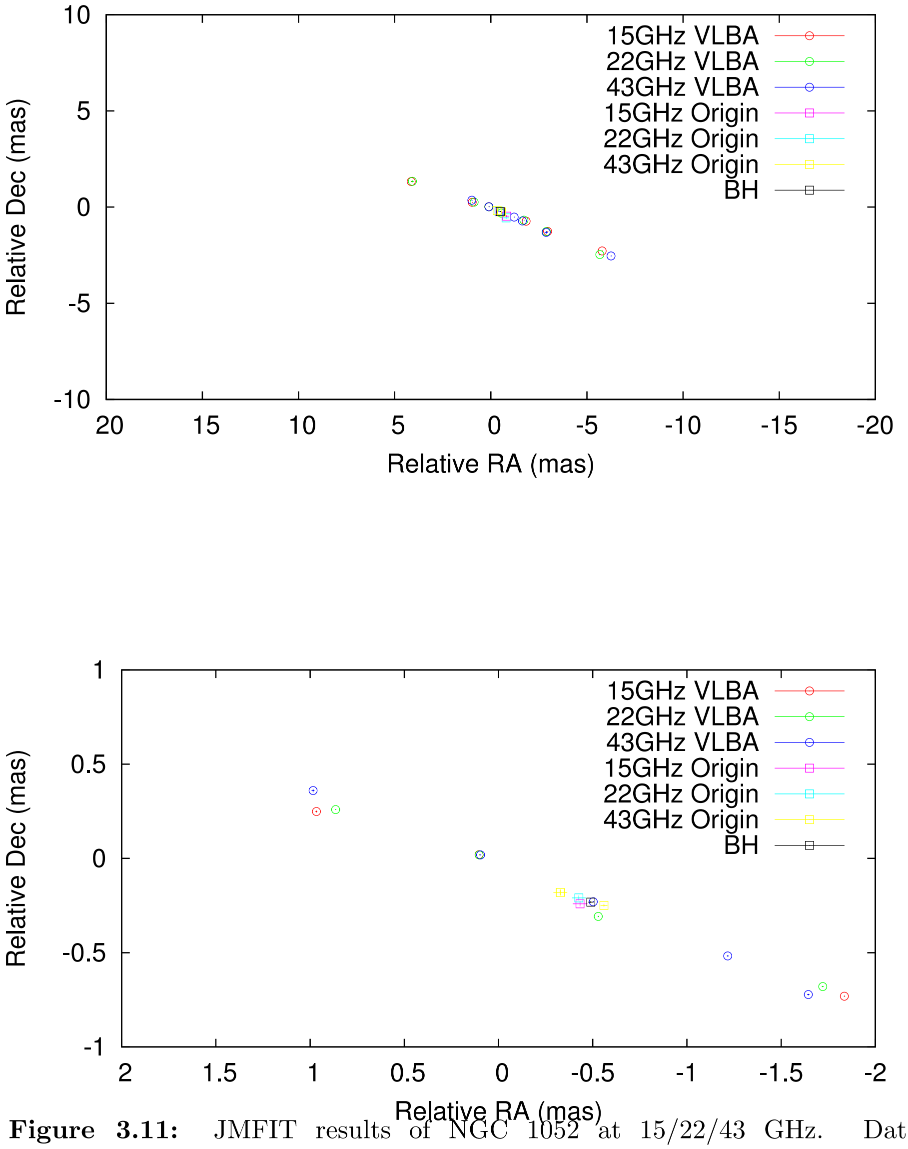

**Figure 3.11:** JMFIT results of NGC 1052 at 15/22/43 GHz. Data sets are the same as Sawada-Satoh et al. (2008). (Top) Whole region. (Bottom) Focused on central region.

## 3.3 RESULTS

### 3.3.1 Profile of Jet Width of NGC 1052

The radial profiles of jet width are shown in Figure 3.12 for the approaching side and Figure 3.13 for the counter side. Figure 3.14 shows the comparison of them. As a result, the measurements were carried out in scales ranging of 0.075 mas–5.85 arcsec, corresponding to 0.0071–560 pc from the core. The unit of horizontal axis of all these plots is a deprojected distance in Schwarzschild radii ($R_{\rm S}$), converted from mas on projected jet images. The measurement range in radial distance resulted in $\sim 480$–$3.7 \times 10^7 R_{\rm S}$ from the core for the jet width of NGC 1052.

At first, the measurements of jet width along jet axis had been fitted with a single power-law model function ($W_{\rm jet} \propto r^a$; $W_{\rm jet}$ is the jet width, $r$ is the distance from the black hole in the unit of $R_{\rm S}$, and $a$ is the power-law index). Since the density of the data sample is significantly higher in the upstream jet than in the downstream as can be seen in Figures 3.12 and 3.13, the upstream jets has a much greater influence on the fit. Therefore, we binned all the multi-frequency data at intervals of $10^{0.25} R_{\rm S}$. Before the binning, we excluded data of $r \leq 10^{4.75} R_{\rm S}$ at 1.6/2.3/4.8 GHz because a significant deviation from a trend is seen. We consider the these deviations only at low frequencies is possibly caused by interstellar broadening effect at our line of sight to the innermost jets, which will be studied in a separate paper. The single power-law fitting resulted in the power-law indices $a = 0.39 \pm 0.11$ and $a = 0.83 \pm 0.09$, for the approaching side and the counter side, respectively. The reduced $\chi^2$ was 1.83 ($p$-value= 0.0252) and 2.07 ($p$-value= 0.0070), indicating that the single power-law does not fit the data well.

Next, we made the fit with a broken power-law model as the same manner in the previous study for NGC 4261 (Nakahara et al. in press). The fitting function is

$$W_{\rm jet}(r) = W_0 \, 2^{\frac{a_{\rm u}-a_{\rm d}}{s}} \left(\frac{r}{r_{\rm b}}\right)^{a_{\rm u}} \left(1 + \left(\frac{r}{r_{\rm b}}\right)^{s}\right)^{\frac{a_{\rm d}-a_{\rm u}}{s}}, \tag{3.1}$$

where $W_0$ is the scale factor, $a_{\rm u}$ is the power-law index for the upstream jet, $a_{\rm d}$ is the power-law index for the downstream jet, $r_{\rm b}$ is the break location, and $s$ is the sharpness of the profile at the break (here, we use the fixed value $s = 10$). The fitting results are represented in Table 3.2 and the reduced $\chi^2$ was improved from single power-law fitting. I consider that these reduced $\chi^2$ values smaller than one are responsible for the oversampling due to overlapping the slice measurements at multi-frequency, not by the overfitting. The reduced $\chi^2$ values in the previous studies had also been taking the smaller values than one. These results and discussions are robust against statistical fluctuation (see Figure 3.15).

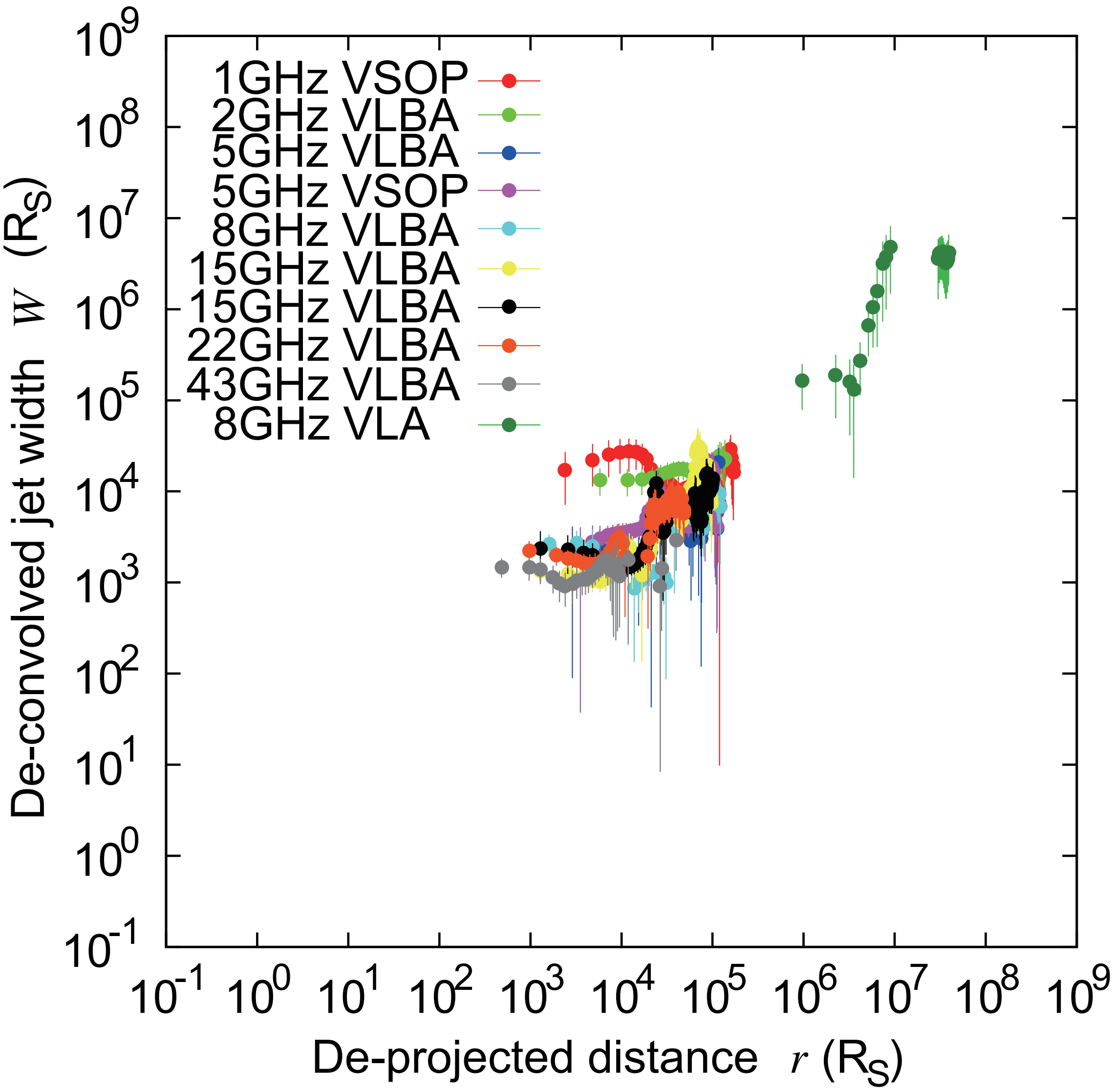

**Figure 3.12:** Radial profile of the measured jet width for approaching side of NGC 1052. The horizontal axis shows distance from the central engine. The vertical axis shows deconvolved jet width. Color variation describes each observed frequency; red: 1GHz and purple: 5 GHz for VSOP data, light green: 2 GHz, blue: 5 GHz, light blue: 8 GHz, yellow: 15 GHz a, black: 15 GHz b, orange: 22 GHz, gray: 43 GHz for VLBA data, and dark green: 8 GHz for VLA data, respectively.

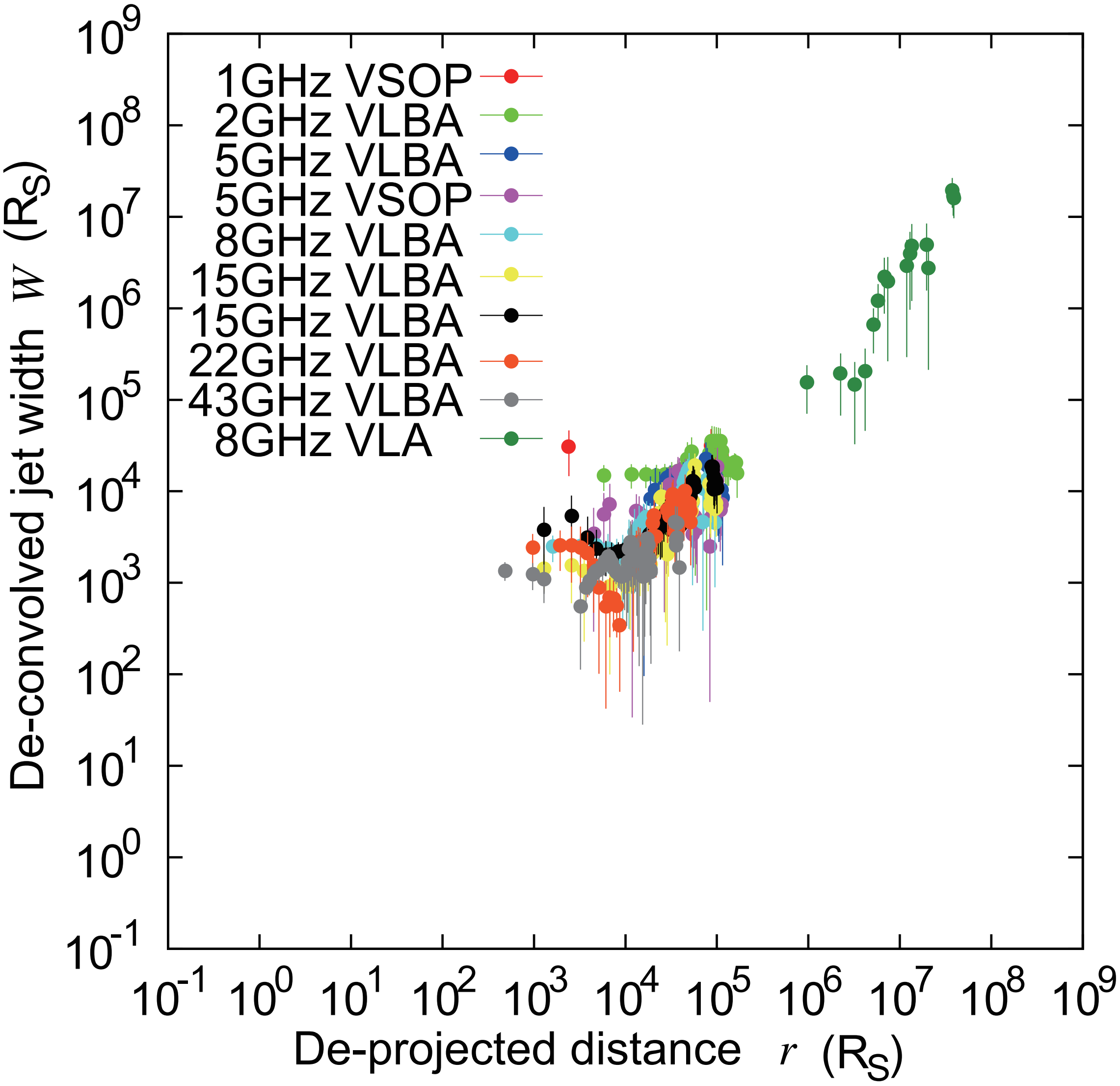

**Figure 3.13:** Radial profile of the measured jet width for counter side of NGC 1052. The horizontal axis shows distance from the central engine. The vertical axis shows deconvolved jet width. Color variation describes each observed frequency; red: 1GHz and purple: 5 GHz for VSOP data, light green: 2 GHz, blue: 5 GHz, light blue: 8 GHz, yellow: 15 GHz a, black: 15 GHz b, orange: 22 GHz, gray: 43 GHz for VLBA data, and dark green: 8 GHz for VLA data, respectively.

**Table 3.2:** Results of Broken Power-law Fit to Jet Structures of NGC 1052.

| Case<br>(1) | $W_0$<br>($\times 10^4$)<br>(2) | $r_\mathrm{b}$<br>($\times 10^4$ $R_\mathrm{S}$)<br>(3) | $a_\mathrm{u}$<br>($\times 10^4$ $R_\mathrm{S}$)<br>(4) | $a_\mathrm{d}$<br>(5) | $\chi^2/ndf$<br>(6) | $ndf$<br>(7) | $p$-value<br>(8) |
|---|---|---|---|---|---|---|---|
| Approaching jet | $0.17 \pm 0.03$ | $0.96 \pm 0.26$ | $0.87 \times 10^{-2} \pm 7.55 \times 10{-}2$ | $0.91 \pm 0.04$ | 0.33 | 13 | 0.99 |
| Counter jet | $1.8 \times 10^{-3} \pm 0.52 \times 10^{-3}$ | $1.03 \pm 0.44$ | $3.77 \times 10^{-2} \pm 0.11$ | $0.95 \pm 0.06$ | 0.63 | 14 | 0.84 |
| Approaching + Counter jets | $0.17 \pm 0.03$ | $0.99 \pm 0.23$ | $0.03 \pm 0.06$ | $0.92 \pm 0.03$ | 0.44 | 31 | 1.00 |

Note. — Col. (1) Cases of fitting analyses; Col. (2) jet width at structural transition; Col. (3) radial distance of structural transition; Col. (4) power-law index of jet structure at upstream; Col. (5) power-law index of jet structure at downstream; Col. (6) reduced chi-squared value; Col. (7) the number of degree-of-freedom; Col. (8) probability of the $\chi^2$ distribution value..

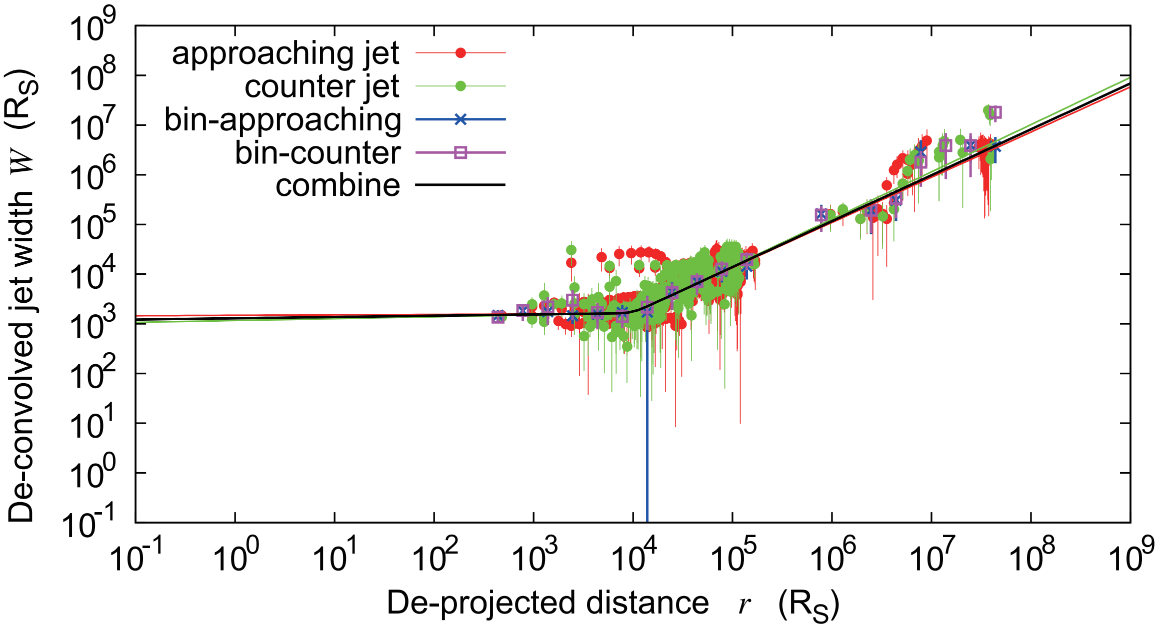

**Figure 3.14:** Comparison between approaching jet and counter jet of NGC 1052. The horizontal axis shows distance from the central engine. The vertical axis shows deconvolved jet width. Red and green points represent approaching and counter jet, respectively. Blue cross and purple square shows the radial binning of approaching jet and counter jet, respectively. The red, green and black lines are power-law fitting of the measured jet width profile for approaching side, counter side, and combined data, respectively.

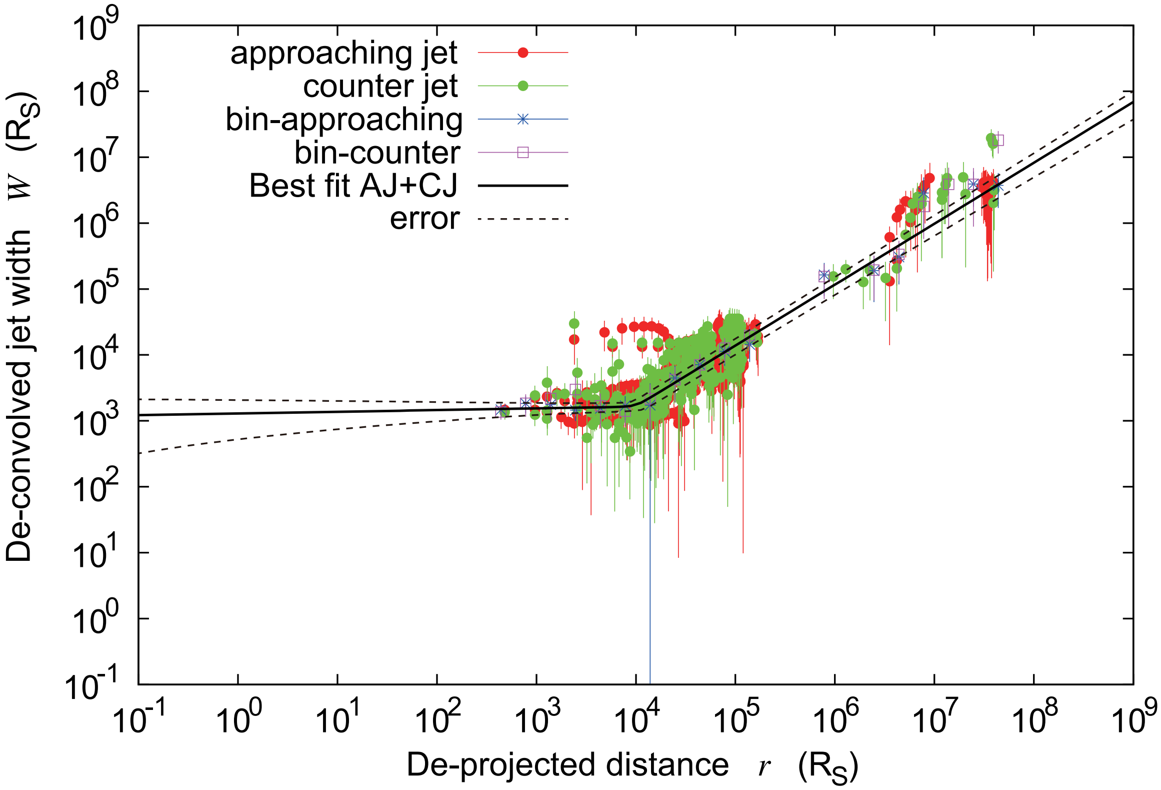

**Figure 3.15:** The broken power-law fitting with the fitting error. The red and green dots are the jet width for approaching and counter side, respectively. The black line represents the broken power-law fitting result. The dashed line represents the fitting error (1 sigma).

## 3.4 Discussion

### 3.4.1 The cylindrical-to-conical structure

On the basis of our investigation for the radial profile of jet width, we found that the approaching and counter jets are symmetric within errors (Table 3.2). Following the case of NGC 4261 (Nakahara et al. in press), NGC 1052 is the second example for the confirmation of symmetry in the two-sided jet structure throughout very wide ranges of physical scales. Moreover, both side of the jet structure changes from a cylindrical ($a \sim 0$) to a conical ($a \sim 1$) structure at $\sim 10^4 R_{\rm S}$. Consequently, we found a structural transition in the NGC 1052 jets, as well as those seen in M87 (Asada & Nakamura 2012), NGC 6251 (Tseng et al. 2016) and NGC 4261 (Nakahara et al. in press) of nearby radio galaxies. However, note that the characteristic feature in the NGC 1052 case is that the jet exhibits a cylindrical-to-conical structure, not a parabolic-to-conical structure as seen in the other these AGNs. The discussion for the physical origin of cylindrical-to-conical structure is presented later in Section 5.2.3.

### 3.4.2 Interstellar Broadening

The interstellar broadening is the phenomenon that the observed radio emission is scattered by the interstellar plasma and the obtained radio image has the dependence of the square of wavelength. This phenomenon had been reported only in Sagittarius A$^*$ (Bower et al. 2006; Doeleman et al. 2008) which is the nearest AGN and locates at the center of our galaxy. Because of the interstellar broadening, the VLBI radio core of Sgr A$^*$ has not been resolved yet. Here, I argue the finding of interstellar broadening in NGC 1052.

I focused on the upper stream jet width for each frequency In the Figure 3.12; and I noticed that the measured jet width seemed to be saturating in upper stream for each frequency. Then, it is reminiscent of the interstellar broadening issue about Sgr A$^*$, and investigated the correlation between frequency and the jet width in upper stream. Figure 3.16 represent the correlation between frequency and the jet width in upper stream. I made the fit with a single power-law function of $a \times x^b + c$ and the fitting results are shown in Table 3.3. It is clear that the jet width of upper stream depends on frequency. Furthermore, the fitted power-law index of the squared frequency indicates that the interstellar broadening exits in the NGC 1052 jet. This is the first discovering for outside the Milky Way.

In Figure 3.17, I compared the size of plasma torus ($\sim$ 0.5 pc; Kameno et al. (2003)) to the jet width profiles at 1.6 and 2.3 GHz. The upstream region whose jet width is rapidly increasing and regularly flattening is the region suspected to be affected by

**Table 3.3:** Results of Single Power-law Fit to Jet Structures of NGC 1052 for upper stream > $10^4.75R_\mathrm{S}$ to investigate the interstellar broadening.

| Case<br>(1) | $a$<br>(2) | $b$<br>(3) | $c$<br>(4) | $\chi^2/ndf$<br>(5) |
|---|---|---|---|---|
| Approaching + Counter jets | $10.42 \pm 2.41$ | -2.14±0.18 | $0.19 \pm 0.01$ | 0.74 |

Note. — Col. (1) Cases of fitting analyses; Col. (2) scale factor ; Col. (3) power law index of jet width; Col. (4) constant; Col. (5) reduced chi-squared value.

the interstellar broadening. As can be seen in Figure 3.17, the size of plasma torus is consistent with the region to be affected by the interstellar broadening.

The central component is undetectable at any frequencies except for 43 GHz (See Figure 3.1–3.9). It suggests that there is a very strong absorption along the line of sight by the free–free absorber with a high electron density such that the central component can not be observed even at 22 GHz.

## 3.5 Summary

We found the symmetric radial profiles of jet width throughout scales from 500 to $4 \times 10^7 R_\mathrm{S}$ on the approaching and counter jet sides in the nearby radio galaxy NGC 1052. The jets show cylindrical-to-conical structures with transitions at $\sim 10^4 R_\mathrm{S}$. The distance of the transitions is consistent with the estimated radius of dense plasma torus as a free–free absorber around the central engine. We suggest a picture that the transverse pressure by the cold accreting matter in the torus supports the over-collimation of the innermost jets in NGC 1052.

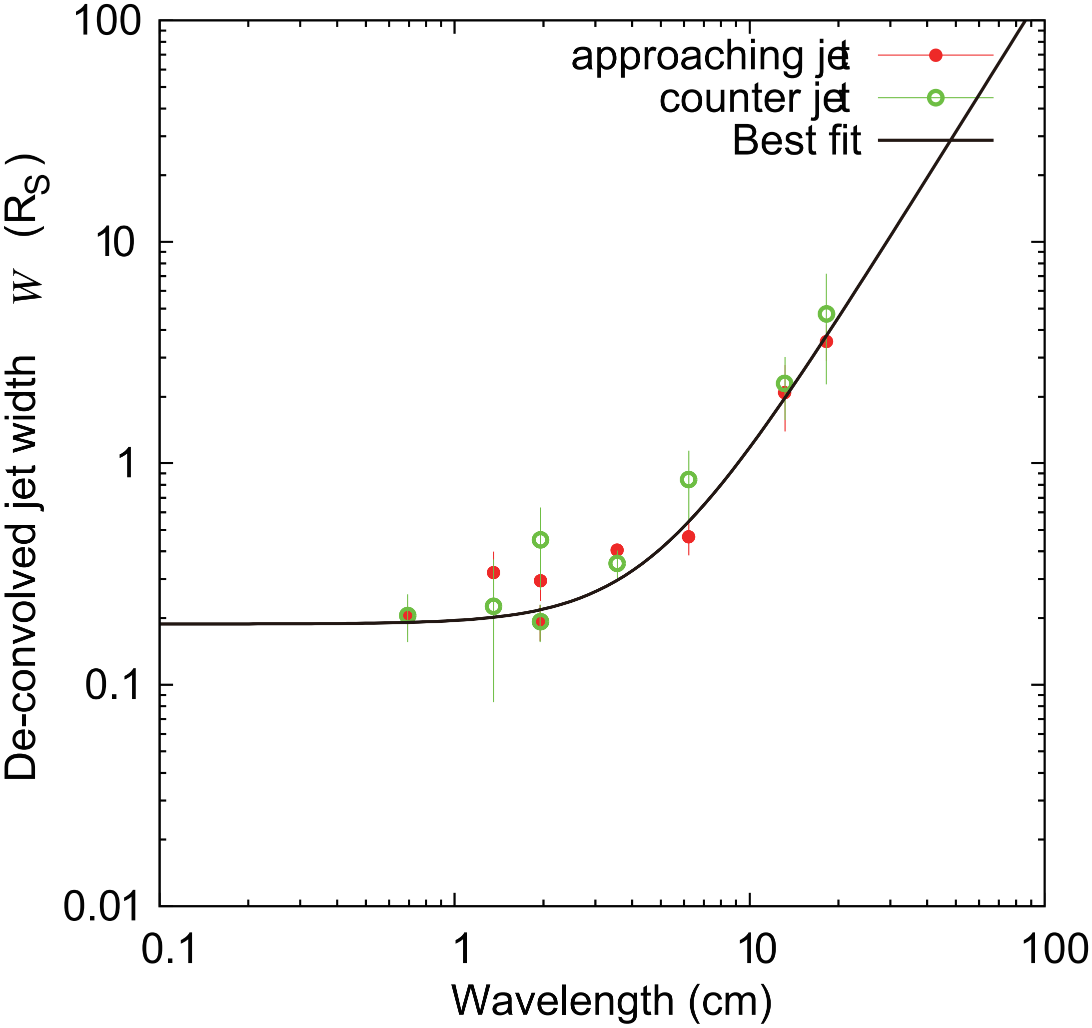

**Figure 3.16:** Results of Power-law Fit to Jet Structures of NGC 1052 for $r < 10^{4.75} R_{\rm S}$. The horizontal axis shows distance from the central engine. The vertical axis shows deconvolved jet width. Gray points and black circles represent approaching and counter jet, respectively. Black line is the best fit for all plots.

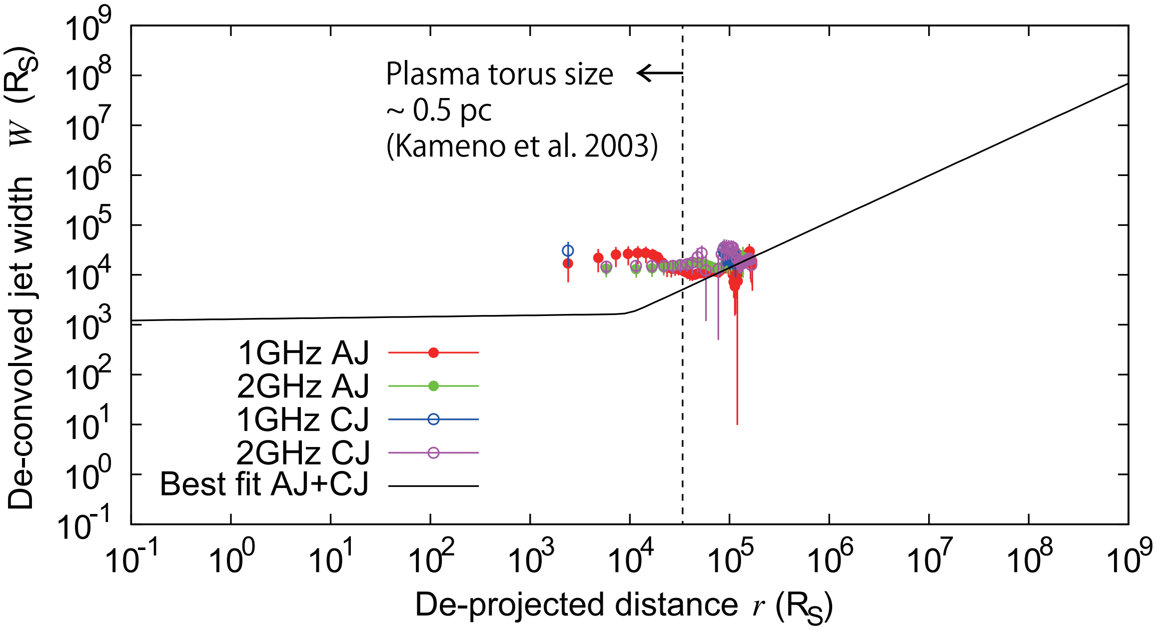

**Figure 3.17:** I compared the plasma torus size ~ 0.5 pc proposed in Kameno et al. (2003) to the measured jet width at 1.6 and 2.3 GHz which corresponds to the region likely to cause interstellar broadening. The red and green plots represent the approaching jet at 1.6 and 2.3 GHz, respectively. The purple and blue circle show the counter jet at 1.6 and 2.3 GHz, respectively. The solid black line represents the broken-power law fit to all the binning data of jet width (same with the black line in Figure 3.14). The dashed line represents the size of plasma torus proposed in Kameno et al. (2003).

# Chapter 4

# Cygnus A

**Abstract** Observational evidence that acceleration of astrophysical jet is related to collimation has been found in several active galactic nuclei (AGNs). Collimation is observed in the form of a parabolic shape in the radial dependence of the transverse width of the jet. We investigated the radial profile of jet width $W(r)$ in Cygnus A at the radial distance $r$ ranging from $\sim 10^3$ $\mathrm{R_S}$ to $\sim 10^9$ $\mathrm{R_S}$ on both their approaching and counter jet sides. We found a discontinuity in the radial profiles of jet width; the jet apparently inflates wider by a factor of six at the radial distance $\sim 5 \times 10^5$ $\mathrm{R_S}$. The power-law dependences of the jet width profile in the inner parsec-scale and outer kiloparsec-scale regions show to be $a \sim 0.55$ $(W(r) \propto r^a)$ consistently. It represents that the parabolic streamline maintains throughout very large scales beyond the gravitational circle of the central black hole. The estimated pressure distribution of the intracluster medium seems to have an ability to confine the Cygnus A jets up to the observed radial range of $\sim 10^9$ $\mathrm{R_S}$. The observed discontinuity suggests that the jet has a multi-layered structure. Which flow layer with a velocity was observed can be explained by a stratified jet scenario and Doppler-debeaming effect for the highly inclined jets of Cygnus A.

## 4.1 Introduction

The collimation and acceleration mechanisms in astrophysical jets remains one of the open questions and actively discussed in astrophysics. Cygnus A (3C 405) is one of the most luminous radio galaxies and an archetypal Fanaroff-Ryley II (FR II) radio galaxy (Carilli & Barthel 1996) with very narrow jets, which transport power from the central engine to terminal hot spots in two-sided radio lobes. The jet of Cygnus A is seen at a large viewing angle in the range 50–85 deg (Bartel et al. 1995, and references therein). Counter jets are apparent with knots with a few seemingly smooth emission, in addition to a series of elongated knots continuous to the lobe in the approaching side (Steenbrugge & Blundell 2008). The parsec (pc) and sub-pc scale jets have been intensively investigated by very-long-baseline interferometry (VLBI) observations at milli-arcsecond (mas) resolutions (e.g., Carilli et al. 1991; Krichbaum et al. 1998; Bach 2004; Boccardi et al. 2016b,a). The limb brightening intensity profile along the transverse direction is found at inner 2 mas regions on both the approaching and counter jet sides in Cygnus A (Boccardi et al. 2016b). The limb brightening has been interpreted as layered compositions of spine and sheath flows in the jet, i.e., one is a fast and light ultra-relativistic spine embedded in an outer layered flow of slower and denser material (Sol et al. 1989). Boccardi et al. (2016b) suggested the presence of a fast and a slow layer with different acceleration gradients in the pc scale jets of Cygnus A. The evolution of bulk acceleration depending on radial distances from the nucleus has also been observed by Krichbaum et al. (1998) and (Bach et al. 2002) from proper motion measurements. In this acceleration zone, a parabolic shape has been inferred from the radial dependence of jet width (Boccardi et al. 2016b). On the other hand, the jet was resolved transversely with a constant width from 4 mas to 20 mas, suggesting a confined jet (Carilli et al. 1991). The external pressure to collimate the jet flow by the ambient medium has been discussed (see, Carilli & Barthel 1996, for a review). Thus, Cygnus A is an important example that the evidence of relation between bulk acceleration and collimation has been suggested from observations at the sub-pc and pc scale regions.

The connection between the parabolic shape and the bulk acceleration in a jet has been confirmed throughout from the scale of Schwarzschild radius ($\mathrm{R_S}$) to $\sim 130$ pc in the M87 jet (Nakamura & Asada 2013; Hada et al. 2013; Asada et al. 2014; Mertens et al. 2016). The parabolic acceleration region eventually ends at an outer radial distance and transitions to a conical shape, which has been detected in the M87 jet at $\sim 2 \times 10^5 \mathrm{R_S}$ from the central engine (Asada & Nakamura 2012), the NGC 6251 jet at $(1\text{–}2) \times 10^5 \mathrm{R_S}$ (Tseng et al. 2016), and the NGC 4261 jets at $\sim 10^4 \mathrm{R_S}$ (Nakahara et al. in press). The detections of this sort of transition have been required to investigate the evolution of jet width over very wide ranges of radial distance from sub-pc to kpc scales. However, for Cygnus A, the profile of jet width throughout such a wide radial distance or the existence of transition is still unknown although prominent jets in sub-pc to kpc scales are clearly observed. Moreover, Cygnus A is a Fanaroff-Riley (Fanaroff & Riley 1974) class II (FR-II) radio galaxy, while all the three sources in the previous studies are FR-I type ones. Transversally resolving of this FR-II jets over very wide ranges of radial distance potentially bring a crucial result for understanding of the jet collimation.

Cygnus A is at the redshift $z = 0.056075$ (Owen et al. 1997), the sixth closest FR-II galaxy in the 3CR catalog (Leahy et al. 1997; Black et al. 1992). Cygnus A is located at a co-moving distance of 238 Mpc, assuming ΛCDM cosmology with $H_0 = 70.5\ h^{-1}$ km s$^{-1}$ Mpc$^{-1}$, $\Omega_{\mathrm{M}} = 0.27$, $\Omega_\Lambda = 0.73$; an angular scale of 1 mas corresponds to 1.09 pc in projection. Other nearby FR-II galaxies whose jets are clearly observed are 3C 111 ($z = 0.048500$) and 3C 445 ($z = 0.055879$); their black hole masses are $1.8 \times 10^8\ M_\odot$, (Chatterjee et al. 2011) and $1.4 \times 10^8\ M_\odot$ (Bettoni et al. 2003), respectively. On the other hand, a much higher mass for Cygnus A's black hole was estimated to be $2.5 \times 10^9\ M_\odot$ from a study based on kinematics for optical and near-infrared spectroscopic data (Tadhunter et al. 2003). The angular scale of 1 mas corresponds to $4.5 \times 10^3$ $\mathrm{R_S}$ in deprojection, if we assume an inclination angle of 74.5 deg (an upper limit, see Boccardi et al. 2016b). Therefore, geometrical investigations in units of Schwarzschild radius can be advantageously promoted in this radio galaxy.

In this Chapter, we investigate the evolution of radial profiles of jet width for Cygnus A on the basis of new measurements using Very Large Array (VLA) archival data, in addition to published data from VLBI measurements. We uncover the structure of jets over a range of $10^3$–$10^9$ $R_{\mathrm{S}}$ in distance from the central engine of Cygnus A on both the approaching and counter jets. The present paper is structured as follows. In Section 4.2, the VLA and VLBI data we used in the present paper and image analysis for the jet-width measurement in the VLA images are described. In Section 4.3, we present the results of the jet-width profiles. In Section 4.4, we discuss the structure and its physical conditions for the Cygnus A jets. Finally, we summarize the results and implications of our study in Section 4.5.

## 4.2 Data and image analyses

### 4.2.1 VLA 5 GHz data

We retrieved a VLA archival image of total intensity map from the NASA/IPAC Extragalactic Database (NED). The image was originally provided by Perley et al. (1984). The visibility data had been obtained at 4.885 GHz in the A-array and B-array configurations, and combined for image synthesis. A circular beam of 0.4 arcsec in diameter was used for convolution. The image was made in 0.125 arcsec/pixel. The image root-mean-square (RMS) noise was measured to be $1\sigma = 0.9$ mJy beam$^{-1}$ in a region of blank sky.

The image is shown in Figure 4.1. In the approaching jet side, several blobs and continuous jet structures are clearly seen toward the western radio lobe. On the other hand, only a few features are apparent in the counter jet side.

### 4.2.2 VLA 22 GHz data

The VLA data set GK0012 was retrieved from the data archive system of the National Radio Astronomy Observatory (NRAO). We chose the data because of the longest on-source time (26.66 ksec) to Cygnus A in the VLA archive for the K-band with the VLA A-array configuration. The observation was conducted on 04 March 1994 at 22.2351 GHz. Dual-circular polarization was received, with a bandwidth of 50 MHz. The data reduction procedures follow standard manners for VLA data using `AIPS` (Astronomical Image Processing System). In the procedures, we performed opacity correction, which is required for data at high frequencies. We performed deconvolution and self-calibration (only in phase term) iteratively using `Difmap` software for image construction. Since significant contributions from two hot spots separated from the central core by $\sim$ 1 arcmin, flux subtractions by CLEAN algorithm was needed to reveal weak jet features. The image was made with natural weighting, resulting in a synthesized beam of $\sim 0.1$ arcsec in diameter. We explicitly defined a restored circular beam with a 0.10-arcsec diameter to obtain a final image.

The image is shown in Figure 4.3. Unlike the VLA 5 GHz image (Section 4.2.1), only jet features near the central core are seen at 22 GHz. Hence, The we made a image focusing on the central region in 0.01 arcsec/pixel. The resultant image RMS noise is $1\sigma = 0.7$ mJy beam$^{-1}$.

### 4.2.3 VLBI 4.9 GHz data

We use measured component sizes provided by Bach (2004) based on VLBI observations using VLBA and Effelsberg at 4.9 GHz, which can bridge the gap between the VLA scales and the innermost region. The observations were carried out at three epochs (2002.03, 2002.51, and 2003.24). The sizes were determined by visibility-based model fitting with circular Gaussian model components using `Difmap`. We use for the present study only components that were separated by more than 3 mas from a stationery central component, because inner components might not be sufficiently resolved with the spatial resolution at 5 GHz. The values are listed in table 6.9 in Bach

(2004). The listed error of the full-width at half maximum (FWHM) for each component is relatively small; for the present study, we determined the error of FWHM by doubling the error in position, according to Fomalont (1999): the positional error and the width error are approximately estimated to be $\Delta RW/2P$ and $\Delta RW/P$, respectively, where $\Delta R$ is the post-fit r.m.s. error, $P$ is the peak intensity, and $W$ is the width.

### 4.2.4 VLBI 43 GHz data

We adopt component sizes measured in VLBI image obtained at 43 GHz by Boccardi et al. (2016b) to describe the jet-width profile at the innermost region. The observations were carried out at four epochs (2007.81, 2008.79, 2009.21, and 2009.86) using the Global VLBI array. In the study by Boccardi et al. (2016b), two methods were performed to analyze jet structures: visibility-based model fitting assuming circular Gaussian model components and slice analyses of transverse profile of jets. The result values from the former method were listed in table 2 in Boccardi et al. (2016b). On the other hand, the latter was shown only in the form of plot. The latter analysis revealed a double-ridge structure in the transverse profile of jets at inner 2 mas. Their figure 7 showed a comparison of the results by the two methods; FWHM of the transverse structure from the two method were apparently consistent. Hence, we use the FWHMs as jet widths by the Gaussian model-fitting analysis. Since the errors of the FWHMs listed are quite small compared to the beam size. For the present study, we determined the error of FWHM by doubling the error in position by the same way applied to the VLBI 4.9 GHz data above (Section 4.2.3).

They reported that the radial profile of jet width has power-law dependence of $a = 0.55 \pm 0.07$ ($W(r) \propto r^a$), suggesting a parabolic shape, as shown in their figure 8. We omitted the component J2, occupies only a portion of the jet in the transverse direction, following Boccardi et al. (2016b). An outlier (J3, epoch 4) was also discarded in the present study.

### 4.2.5 Image analyses

In the VLA image at 5 GHz, we made a pixel-based analysis of jet structures in the rectangular region indicated in Figure 4.1. First, the images were rotated by 16 deg clockwise to make the mean jet axis being parallel to the horizontal axis, and sliced pixel-by-pixel along the transverse direction of jet. Next, the transverse intensity profile of each slice were fitted with a Gaussian model profile. We considered a baseline level as a free parameter in the Gaussian fitting, because of some contribution was present in lobe region. We discarded a fit result if its solution indicated that (1)

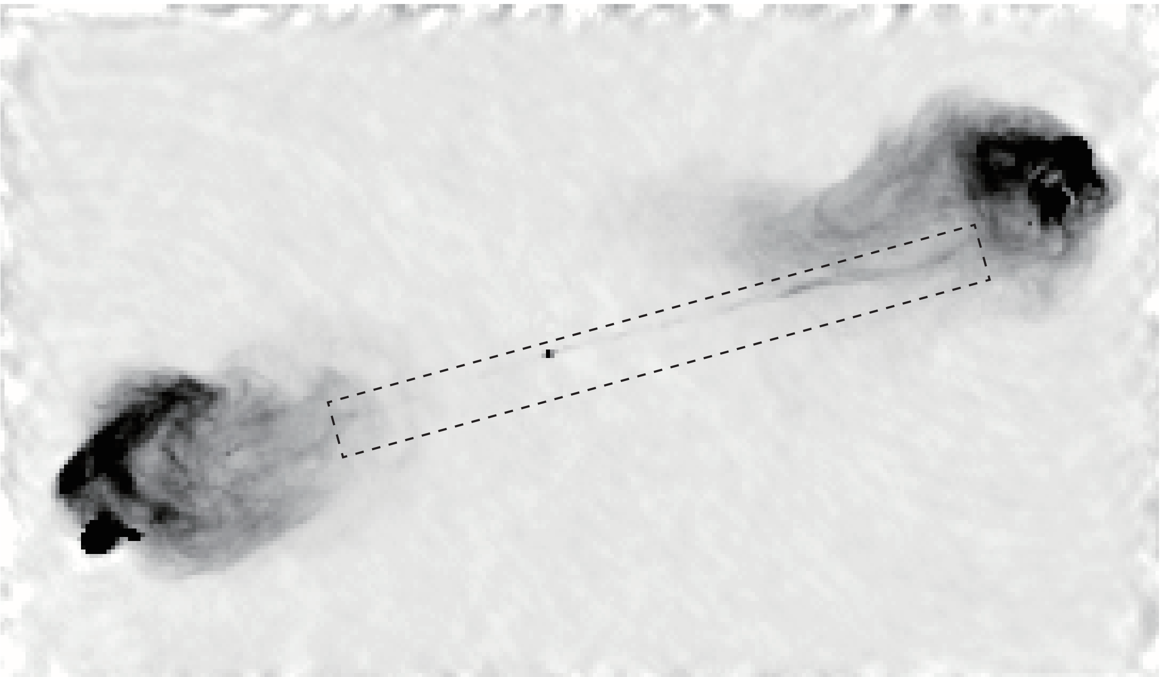

**Figure 4.1:** The 5-GHz VLA archival image originally provided by Perley et al. (1984), which was retrieved from NED. The map was rotated clockwise by 16 deg. Rectangle shows the region that was the subject of slice analysis in the present study.

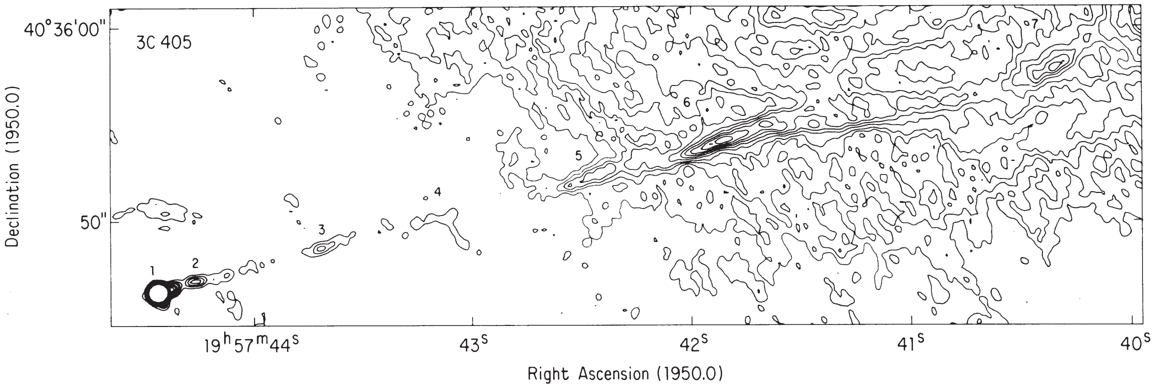

**Figure 4.2:** The 5-GHz VLA contour map for the approaching jet side of Cygnus A, which was presented as figure 3 in Perley et al. (1984). The map was rotated clockwise by 16 deg.

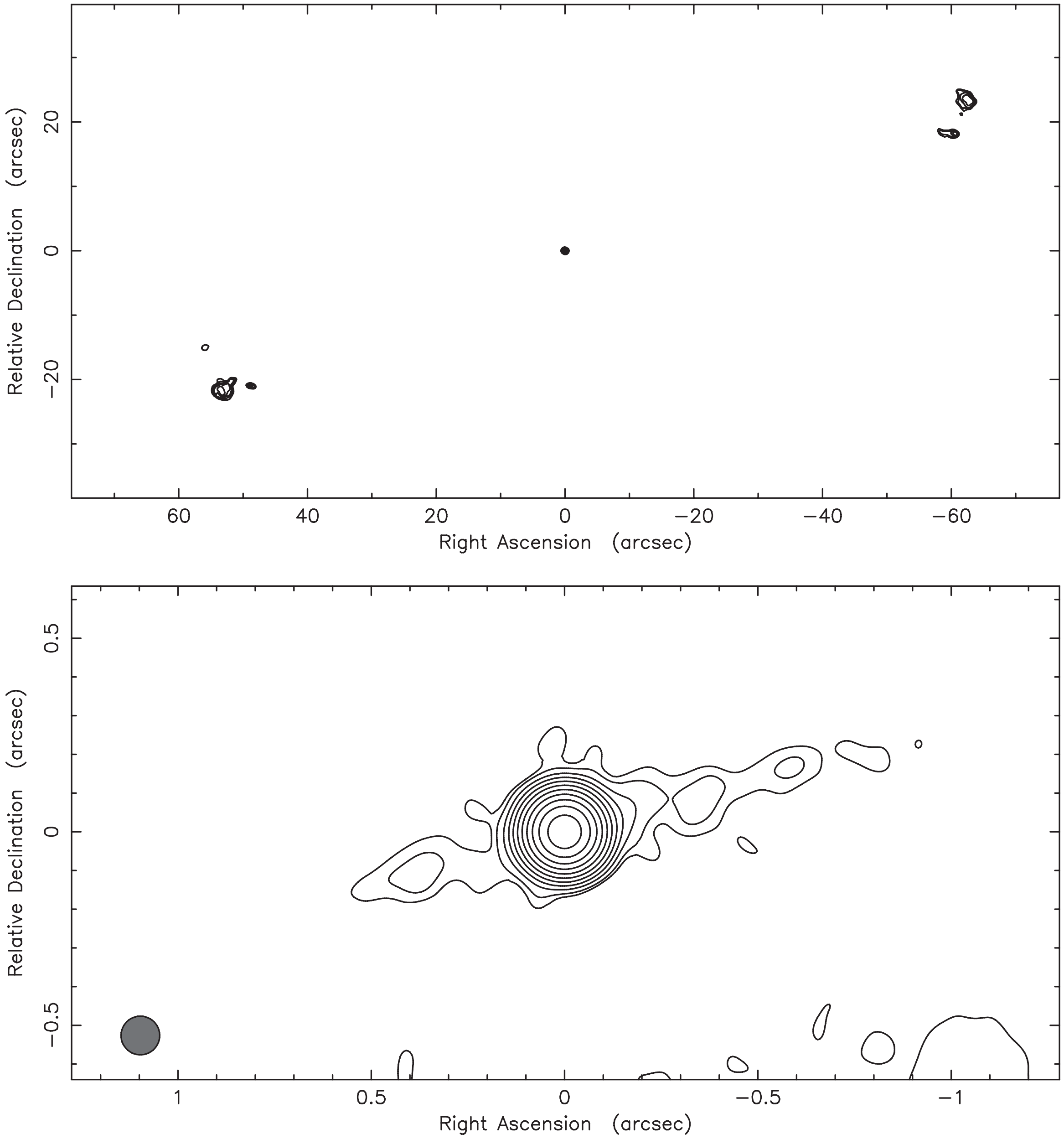

**Figure 4.3:** (Upper) Wide field-of-view image of VLA 22 GHz. Contours start from the 5 sigma image RMS noise and increase by factors of 2 ($1\sigma = 3.7$ mJy beam$^{-1}$). (Lower) Nuclear region of the VLA 22 GHz image. The lowest contour is $2\sigma$, and subsequent ontours start from $3\sigma$ of image RMS noise and increase by factors of $\sqrt{2}$ ($1\sigma = 0.7$ mJy beam$^{-1}$).

a jet width was statistically unresolved, (2) a peak intensity was less than $3\sigma$ of image noise, or (3) a sliced location was too close (less than 1.5 times the angular resolution) to the peak of the central core. The third condition needs to avoid a contamination from the central core, which would involve whole emissions of inner (approaching and counter) jets with various widths. Because 0.125 arcsec/pixel and a 0.4-arcsec resolution resulting in 1 pixel corresponding to 1/3.2× resolution, the pixel-based analysis along the jet axis was not so oversampling. Previous studies making the same kind of analysis sliced at every 1/5 of the beam size as independent measurements (Tseng et al. 2016; Boccardi et al. 2016b, see a study of resolution limit by Lobanov 2005).

We analyzed the central region of the VLA image at 22 GHz, where extended structures in both the approaching and counter jet sides were apparent (Figure 4.3). First, the images were rotated by 16 deg clockwise to make the mean jet axis being parallel to the horizontal axis, and sliced pixel-by-pixel (0.01 arcsec/pix) along the transverse direction of jet. Next, the transverse intensity profile of each slice were fitted with a Gaussian model profile. We discarded fit results if its solutions met the conditions (1), (2), or (3) described above. Furthermore, (4) we reduced oversampled measurements into an appropriate sampling every one fifth of resolution, equivalent to 0.02 arcsec. Consequently, we obtained measurements of jet width at distances of 0.15–0.37 arcsec and 0.15–0.42 arcsec in westward (the approaching jet) and eastward (the counter jet), respectively, from the peak of the central core. Although the approaching jet appears more extended, the distance range of successful measurements were less because of large uncertainty.

## 4.3 Results

We make plots for the radial dependence of jet-width profiles in a unit of the Schwarzschild radius ($\mathrm{R_S}$) over wide scales like previous studies (Asada & Nakamura 2012; Tseng et al. 2016; Nakahara et al. in press). We assume a black hole mass of $2.5 \times 10^9\ M_\odot$ (Tadhunter et al. 2003) and an inclination of 74.5 deg (an upper limit, see Boccardi et al. 2016b) for Cygnus A to convert the angular scale in arcsec into the deprojected linear scale in $\mathrm{R_S}$. In the present study, we use $4.5 \times 10^6\ \mathrm{R_S}$/arcsec for the conversion.

The definition of the location of black hole is crucial to test the radial profile of inner $\sim 10^4\ \mathrm{R_S}$, corresponding to inner $\sim 2$ mas, which is the subject of VLBA observations. An apparent peak intensity of the central core is potentially shifted by the order of sub-mas toward downstream due to synchrotron self-absorption or free–free absorption (Lobanov 1998; Kovalev et al. 2008). In Cygnus A, apparent core shifts between different frequencies have been reported by Bach (2004), which determined by averaging results from all the epochs of their multi-frequency observations. From these results, we derive a core shift as a function of frequency: $r = 17.4\nu^{-1.42}$ in units of mas, where $\nu$ is the observing frequency in units of GHz. The position of central engine can be estimated at infinite frequency by using this function. As a result, the positions of components for the VLBI measurements should be corrected by 1.83 mas and 0.085 mas at 4.9 GHz and 43 GHz, respectively. The correction of radial positions was applied to the approaching and the counter jet sides. Boccardi et al. (2016b) pointed out the presence of a sharp gap with $\sim 0.1$ mas in size and a minimum width in the jet emission situated at $\sim 0.2$ mas east of the core at 43 GHz; they argued that it is likely that the gap marks the true location of the central engine (see also, Krichbaum et al. 1998; Boccardi et al. 2016a). In the present paper we used the location of central engine on the basis of the core shift effect.

Figures 4.4 and Figure 4.5 show the radial dependences of measured jet widths for Cygnus A, which are separately described the approaching jets and counter jets, respectively. Figure 4.6 shows the plot in which both the approaching jet side and the counter side are overlaid. As a result, the measurements covers the range from $\sim 10^3$ $\mathrm{R_S}$ to $\sim 10^9$ $\mathrm{R_S}$, which is comparable to the investigations for NGC 6251 (Tseng et al. 2016) and NGC 4261 (Nakahara et al. in press) The jet widths in the two sides are apparently good agreement throughout the measurement ranges, although the counter jet is slightly wider than the approaching one (by a factor of $\sim 2$ in the outer region).

### 4.3.1 Discontinuity in Jet Width Profiles

Most notably, power-law dependences of the jet width profile at $< 0.1$ arcsec in the VLBI measurements and $> 0.1$ arcsec in the VLA measurements look similar but scale factors are different by roughly an order of magnitude. This feature is evident in the approaching side; a similar sign is also apparent on the counter jet side. Thus, the radial profile of jet width shows a discontinuity between the inner region and the outer region. The boundary at $\sim 0.1$ arcsec is approximately $5 \times 10^5$ $\mathrm{R_S}$ from the central engine.

### 4.3.2 Power-law Dependencies

We make statistical evaluations for these observed profile. We performed fitting with a power-law function to various cases, results of which are shown in Table 4.1. The fitting function is $W(r) \propto r^a$, where a is the power-law dependence.

By using data from the whole range of radial distances, a single power-law function cannot describe well the measurements of approaching jets (the probability $p = 0.012$)

**Table 4.1:** Results of Single Power-law Fit to Jet-Width Profile.

| Case<br>(1) | $a$<br>(2) | $\chi^2/ndf$<br>(3) | $ndf$<br>(4) | $p$-value<br>(5) |
|---|---|---|---|---|
| Inner AJ | $0.55 \pm 0.02$ | 1.223 | 43 | 0.150 |
| Inner CJ | $0.66 \pm 0.03$ | 0.384 | 9 | 0.943 |
| Inner AJ+CJ | $0.55 \pm 0.02$ | 1.501 | 54 | 0.010 |
| Outer AJ | $0.56 \pm 0.03$ | 0.744 | 190 | 1.000 |
| Outer CJ | $0.55 \pm 0.03$ | 0.533 | 32 | 0.986 |
| Outer AJ+CJ | $0.51 \pm 0.03$ | 0.791 | 224 | 0.991 |
| Inner+Outer AJ | $0.69 \pm 0.01$ | 1.220 | 235 | 0.012 |
| Inner+Outer CJ | $0.73 \pm 0.01$ | 0.827 | 43 | 0.782 |
| Inner+Outer AJ+CJ | $0.69 \pm 0.01$ | 1.522 | 295 | $10^{-8}$ |

Note. — Col. (1) Cases of fitting analyses; Col. (2) power-law index $a$ of jet width profile ($W(r) \propto r^a$); Col. (3) reduced chi-squared value (chi-square and the number of degree-of-freedom (ndf)); Col. (4) the number of degree-of-freedom; Col. (5) probability of the $\chi^2$ distribution value.

or the both jets ($p = 10^{-8}$); see the cases "Inner+Outer AJ" and "Inner+Outer AJ+CJ," respectively in Table 4.1. For the counter jet, a single power-law is statistically possible ($p = 0.728$), although the number of measurements was significantly smaller in particular at the inner jet region. The difference of fitted jet widths is a factor of ∼ 6 between the inner and the outer jets.

Next, we fitted the measurements for the inner region and the outer region separately. The fitting results are shown in Table 4.1. It is noteworthily that the power-law dependences in the inner and outer regions for the approaching jets equals within their fitting errors for the approaching jet: $a = 0.55 \pm 0.02$ and $0.56 \pm 0.03$, respectively. Furthermore, the power-law index of the counter jets is substantially identical in the outer region ($0.55 \pm 0.03$) where the number of samples is significant.

## 4.4 Discussion

One of the three our findings is that the radial profile of jet widths in Cygnus A appears a discontinuity at 0.1 arcsec (approximately $5 \times 10^5$ $\mathrm{R_S}$) from the central engine. This boundary corresponds between the VLBI observation and the VLA observation regions. The jet width jumps wider by roughly an order of magnitude at the boundary. The second of our findings is that both the inner and the outer jets has radial dependences with almost the same power-law index of $a \sim 0.55$, indicating that the parabolic shape is maintained throughout a very wide range of the radial

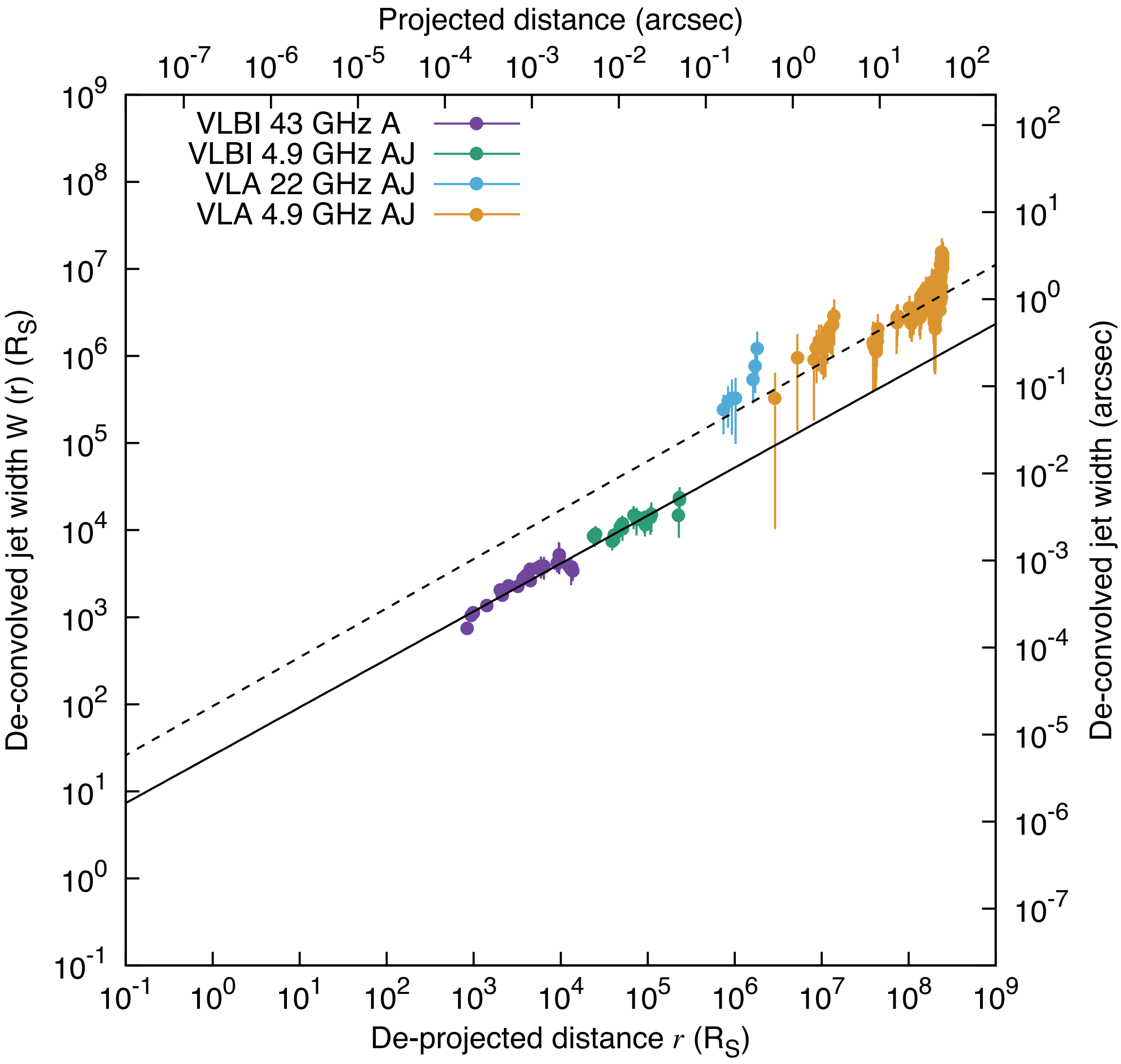

**Figure 4.4:** Radial profile of measured jet width for Cygnus A in approaching jet (AJ) side. The horizontal axis shows deprojected distance from the central engine. The vertical axis shows deconvolved jet width. Filled symbols represent measurements. Color variation represents as follows. AJ in VLBI at 43 GHz. Green: AJ in VLBI at 4.9 GHz. Cyan: AJ in VLA at 22 GHz. Orange: AJ in VLA at 5 GHz. Black solid line and dashed line represent fit results determined separately for inner jets and outer jets, respectively (Table 4.1).

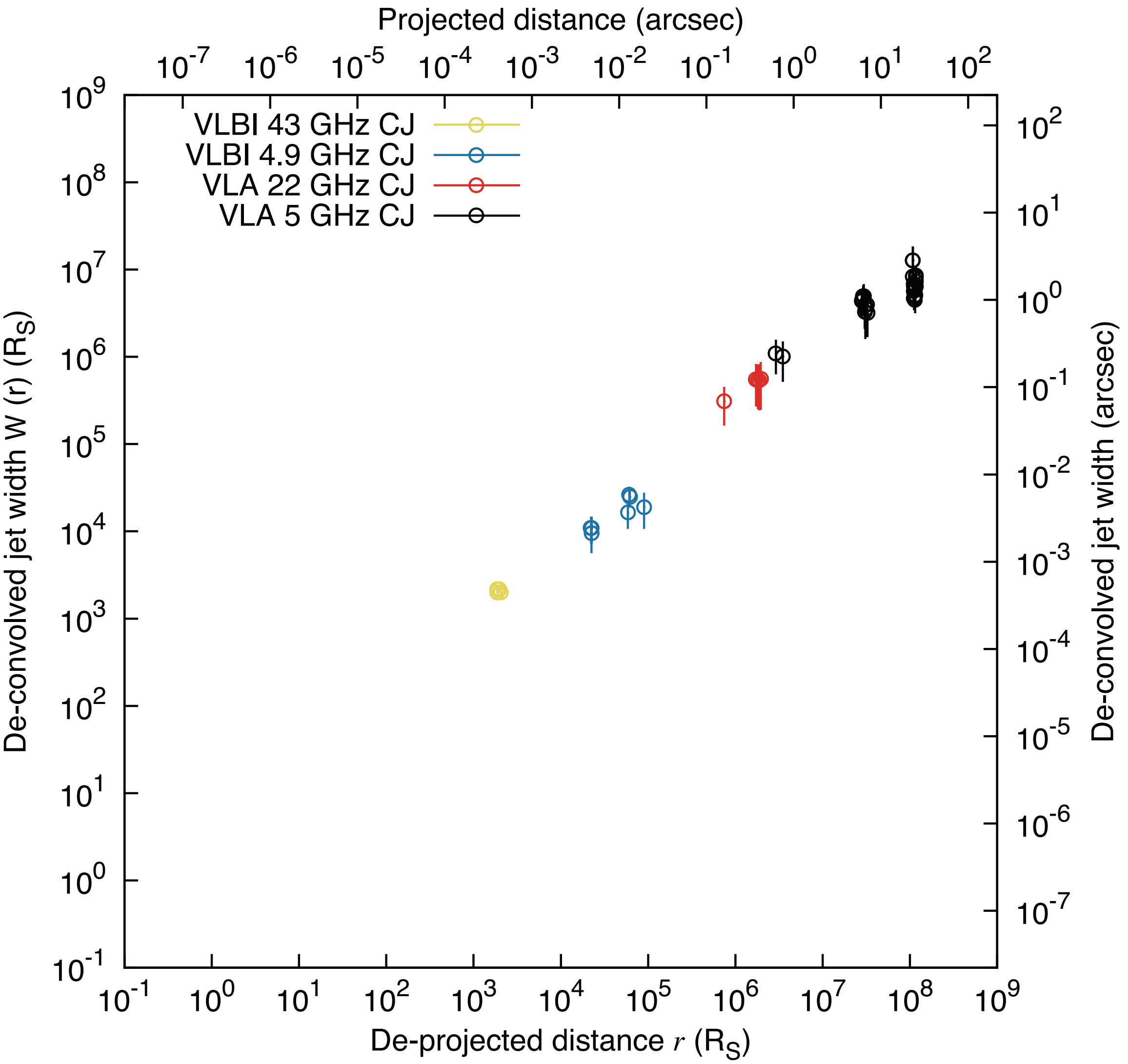

**Figure 4.5:** Radial profile of measured jet width for Cygnus A in counter jet (CJ) side. The horizontal axis shows deprojected distance from the central engine. The vertical axis shows deconvolved jet width. Filled symbols represent measurements. Color variation represents as follows. Yellow: CJ in VLBA at 43 GHz. Dark-blue: CJ in VLBI at 4.9 GHz. Red: CJ in VLA at 22 GHz. Black: CJ in VLA at 5 GHz. No fit result is shown because of less statistics with a relatively small number of measurements for the counter jet.

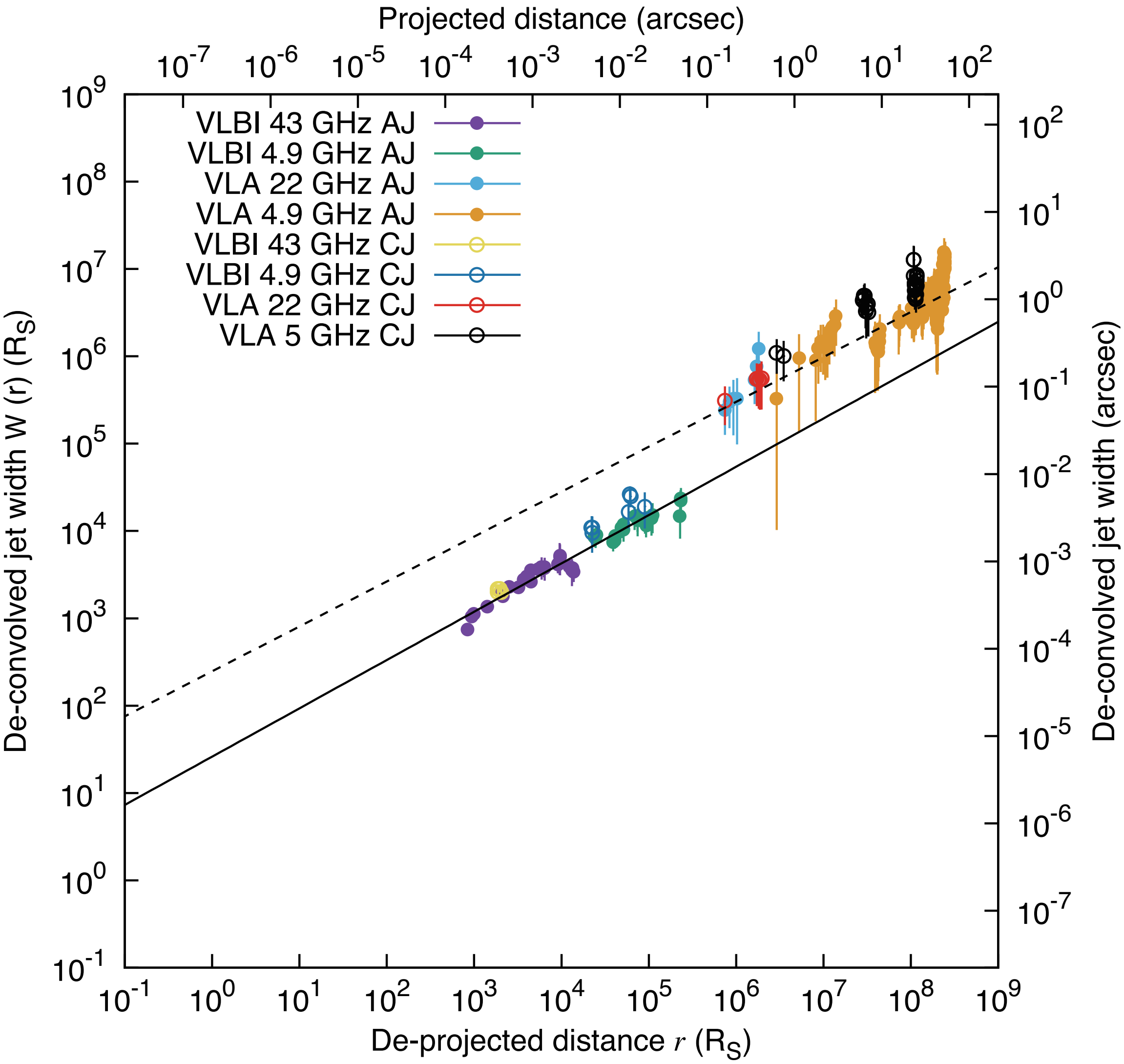

**Figure 4.6:** Radial profile of measured jet width for Cygnus A in approaching jet (AJ) side and counter jet (CJ) side. The horizontal axis shows deprojected distance from the central engine. The vertical axis shows deconvolved jet width. Filled and open symbols represent AJ and CJ, respectively. Color variation represents as follows. Purple: AJ in VLBI at 43 GHz. Green: AJ in VLBI at 4.9 GHz. Cyan: AJ in VLA at 22 GHz. Orange: AJ in VLA at 5 GHz. Yellow: CJ in VLBA at 43 GHz. Dark-blue: CJ in VLBI at 4.9 GHz. Red: CJ in VLA at 22 GHz. Black: CJ in VLA at 5 GHz. Black solid line and dashed line represent fit results determined separately for inner jets and outer jets, respectively (Table 4.1).

distance ranging from $r \sim 10^3$–$10^9$ $\mathrm{R_S}$. The inner jet in the counter side showed a different dependence ($a = 0.66$), which might be attributable to their small number of measurements. The third of our findings is that the the jet width profiles are reasonably symmetric. The fitting results suggested that the counter jet has a wider width by a factor of $\sim 2$ in the outer region.

Jet collimation in Cygnus A had been pointed out from previous VLBI studies. Boccardi et al. (2016b) reported that the jet width profile at the sub-pc scale has power-law dependence of $a = 0.55 \pm 0.07$, suggesting a parabolic shape, as shown in their figure 8 (the present study used their data, see Section 4.2.4). Carilli et al. (1991) reported that the jet was observed to be resolved transversely with a constant width of 2.2 mas at 4–20 mas, suggesting a confined jet. The present study discovered jet collimation on the kpc scales in Cygnus A for the first time.

Compared with the other AGNs from the previous studies, it is decisively different that the shape does not shift to conical even in large scale jets in Cygnus A. The jets of M87 and NGC 6251 show a transition from parabolic to conical shape at $\sim 10^5$ $\mathrm{R_S}$, which are close to their Bondi radii (Asada & Nakamura 2012; Tseng et al. 2016); a transition at $\sim 10^4$ $\mathrm{R_S}$ was also suggested in the jets of NGC 4261 (Nakahara et al. in press). General relativistic magneto hydro dynamic (MHD) simulations have produced parabolic collimation by external pressure and produced transitions from parabolic to conical streamlines (McKinney 2006). Theoretical studies have also suggested that non-conical shape requires a transverse pressure that supports by the external medium with a radial dependence of $p_{\mathrm{ism}} \propto r^{-b}$ (e.g., Blandford & Rees 1974; Blandford & Königl 1979). Komissarov et al. (2009) showed that when the external gas pressure follows $2 \leq b < 4$, the jet forms a parabolic shape with the dependence of $0.5 < a \leq 1$ and eventually becomes conical in outer scales due to insufficient external pressure support. Hence, the jets in Cygnus A should be under-pressured against the ambient gas to maintain the parabolic shape up to $10^9$ $\mathrm{R_S}$.

For Cygnus A the jet pressure estimated under the minimum energy condition is $\sim 6 \times 10^{-10}$ ergs $\mathrm{cm^{-3}}$ for kpc-scale jets (Carilli & Barthel 1996), which should be under-pressured against the pressures of the ambient medium. X-ray observations revealed the pressure gradient of hot gas at kpc scales. The radial profile of intracluster medium (ICM) with a power-law index of $b \sim 1.6$ at 70–500 kpc from the nucleus, which is far from the radio lobe's hot spots ($\sim 60$ kpc), is derived from large-field *Chandra* observations[1], suggesting that the ambient hot gas would collimate jets to a parabolic shape if the pressure is absolutely significant. Reynolds & Fabian (1996) showed the pressure profile at 10–500 kpc based on a *ROSAT* observation, indicating a profile becoming flatter in the radio emitting region; recently, Hofmann et al. (2016)

---

[1] We obtained the index by fitting to the published values of pressure estimates listed in table 5 in Smith et al. (2002).

also presented the pressure profile flattened at inner 30 kpc based on a *Chandra* observation for Cygnus A. Pressures at locations of $\sim$ 10–30 kpc were estimated to be $\sim 5 \times 10^{-10}$ ergs cm$^{-3}$ from *Chandra* data (Chon et al. 2012), which are comparable to the minimum pressure of kpc-scale jets. Consequently, the ambient pressure of X-ray emitting hot gas has a shallow slope and is significant to balance with the minimum jet pressure. Thus, the observed parabolic streamline of jets up to kpc scales is reasonably interpreted in terms of the pressure balance against ambient gas for Cygnus A.

For the discontinuity observed in the jet width profile of Cygnus A, it is necessary to explain the mechanism that causes that phenomenon. I discussed in detail in Section 5.2.6 together with other objects.

## 4.5 Conclusions

We conclude that the observed properties of the Cygnus A jets, (1) a discontinuity in the jet-width radial profile, (2) parabolic shapes up to kpc scales, and (3) a slightly wider apparent width in counter jet side, can be explained by the stratified jet scenario and the Doppler deboosting in this highly inclined FR-II radio galaxy. Such a long-lasting parabolic shape has never been seen in other AGNs (FR-I) in the previous studies for the jet width measurements over very wide ranges of radial distances. The pressure distribution of the ICM radiating X-ray seems to have an ability to confine the Cygnus A jets up to the observed radial range of $\sim 10^9$ R$_\mathrm{S}$. Cygnus A plays an increasingly important role in researches on the jet acceleration/collimation mechanism.

# Chapter 5

# Discussion: Properties of the Parabolic/Conical Jet Structure in Astrophysical Jets

## 5.1 Radial evolution of physical condition in NGC 4261 jet

### 5.1.1 Calculation of physical parameters assuming equipartition condition

Assuming that a jet satisfies the synchrotron minimum energy condition (Pacholczyk 1970), its magnetic field strength is

$$B_{\mathrm{eq}} = \left(6\pi(1+k)c_{12}L_{\mathrm{syn}}\Phi^{-1}V^{-1}\right)^{\frac{2}{7}}, \tag{5.1}$$

where $c_{12}$ is an integral constant containing physical constants, $k$ is the energy ratio of the non-radiating particles to the radiating relativistic electrons (here, we set $k = 1$), $\Phi$ is a filling factor (also set equal to 1), $V$ is the volume, and $L_{\mathrm{syn}}$ is the synchrotron luminosity, which is equivalent to the total radiated radio luminosity calculated as the radio power integrated between 10 MHz and 100 GHz with a spectral index of $-0.76$ along the jet (Table 5.1). The jet pressure is given by

$$P_{\mathrm{jet}} = \frac{B^2}{2\mu_0\epsilon} + \frac{(1+k)U_{\mathrm{e}}}{3V\Phi}, \tag{5.2}$$

where $\mu_0$ is the permeability of free space ($4\pi$ in cgs units), $\epsilon$ is the ordering of the magnetic field (here, we adopt $\epsilon = 3$, indicating a tangled magnetic field, as in

Kolokythas et al. 2015 and O'Sullivan et al. 2011), and $U_{\mathrm{e}}$ is the electron energy density.

Using the obtained profiles $W(r) \propto r^a$ and $F'(r) \propto r^b$, the expected radial profiles of the synchrotron luminosity per unit volume $L_{\mathrm{syn}}/V$, synchrotron luminosity per unit length $L_{\mathrm{syn}}/R_{\mathrm{S}}$, magnetic field strength $B_{\mathrm{eq}}$, and the jet pressure $P_{\mathrm{jet}}$ are formed as follows:

$$\begin{aligned} L_{\mathrm{syn}}(r)/V &\propto r^{b-2a} && (5.3)\\ L_{\mathrm{syn}}(r)/R_{\mathrm{S}} &\propto r^{b} && (5.4)\\ B_{\mathrm{eq}}(r) &\propto r^{\frac{2}{7}(b-2a)} && (5.5)\\ P_{\mathrm{jet}}(r) &\propto r^{\frac{4}{7}(b-2a)}, && (5.6) \end{aligned}$$

as $L_{\mathrm{syn}}(r) \propto F'(r)$ and $V = (W(r)/2)^2\pi dL$, where $dL$ is the unit length along a jet.

### 5.1.2 Evolution of Synchrotron Energetics

Figures 5.2, 5.3, 5.4, and 5.9 show the radial profiles of $L_{\mathrm{syn}}/V$, $L_{\mathrm{syn}}/R_{\mathrm{S}}$, $B_{\mathrm{eq}}$, and $P_{\mathrm{jet}}$, respectively, along the approaching jet in the equipartition condition. These figures include the results of a fitting analysis using a broken power-law model. In all cases, two transitions located at $\sim 1 \times 10^4 R_{\mathrm{S}}$ and $\sim 3 \times 10^6 R_{\mathrm{S}}$ are found. From this, we define the following three regions for convenience: (i) $r {<\sim} 1 \times 10^4 R_{\mathrm{S}}$, (ii) $1 \times 10^4 R_{\mathrm{S}} {<\sim} r {<\sim} 3 \times 10^6 R_{\mathrm{S}}$, and (iii)$3 \times 10^6 R_{\mathrm{S}} {<\sim} r$. Table 5.1 lists the results of power-law indices for the three regions: all of the indices are consistent with those expected from equations (5.3), (5.4), (5.5), and (5.6).

All of the physical parameters decrease more steeply in the conical region (ii) than in the parabolic region (i). This can essentially be explained by the difference in expansion rates as the internal energy density should be significantly decreased by adiabatic expansion in the conical region.

In the region (iii), $L_{\mathrm{syn}}/R_{\mathrm{S}}$ increases with distance as shown Figure 5.3, while $L_{\mathrm{syn}}/V$ continues to decrease. This suggests that the cross sectional increase contributes more efficiently than does the decrease of synchrotron radiative efficiency at the VLA scale. Energy injection to the radiative particles and magnetic field is required for this enhancement. If the bulk jet motion is decelerated, the kinetic energy of the jet flow is potentially converted to particle and magnetic energies in the plasma and then thrown off as synchrotron radiation. This might be the reason for the enhancement of the observed flux density with increasing distance in region (iii) ($F'(r) \propto r^{+0.51}$, as given in Table 2.3). Through this process, the total magnetic energy can be accumulated in the jet plasma, resulting in a milder reduction of the radial profile of the magnetic field strength in region (iii), as shown Figure 5.4. Our spectral index profile also supports this process. In our calculation of jet radiation profile in Section 2.3.2, a spectral index $\alpha = -0.76$ was applied at the VLBA scale. On the other hand, Figure 5.1 shows spectral index profiles along the approaching jet of between 1.4 and 5.0 GHz at the VLA scale. The spectral index decreases from $\alpha = -0.76$ at the VLBA scale to $\alpha \sim -1.6$ at the beginning of the VLA scale and subsequently enhances to $\alpha \sim -0.5$, which is consistent with the previous result of $\alpha = -0.53$ (Kolokythas et al. 2015) focusing on the lobe. Note that the spectral index is locally enhanced to $\alpha \sim 0$ at $\sim 30$ arcsec ($\sim 1 \times 10^8 R_{\rm S}$) from the nucleus. This location corresponds to the site at which the jet becomes surrounded by the lobe on the VLA images, a phenomenon that can also be explained by the conversion of jet kinetic energy to particle and magnetic energies. The surrounding medium of the lobe disturbs the flow in the middle of FR-I jets, resulting in an obvious enhancement of spectral index. This phenomenon is differs from the particle acceleration seen in hot spots at the tips of FR-II jet lobes.

The bulk acceleration of jets takes place in a parabolic stream in M87 (Nakamura & Asada 2013; Asada et al. 2014). By contrast, NGC 4261 has only one example for jet speed measurement, with an intrinsic speed of $(0.46 \pm 0.02)c$ at 8.4 GHz at $r \sim 2 \times 10^4 R_{\rm S}$ (Piner et al. 2001), a location corresponding to the transition point between the parabolic (i) and conical (ii) regions. In the case of NGC 4261, high spatial resolution observations above 15 GHz are necessary to measure the proper motion in the parabolic region (i).

### 5.1.3 Magnetic energy

It can also define that the magnetic energy per unit jet length is

$$B_{\rm eq}(r)^2 W(r)^2 \propto r^{\frac{2}{7}(b-2a))^2+a^2}. \tag{5.7}$$

I calculated the magnetic energy by substituting $a$ and $b$ into equation 5.7 for the regions (i), (ii), and (iii), and obtained following theoretical values: region (i) $\propto r^{-0.38}$, (ii) $\propto r^{-0.53}$, and (iii) $\propto r^{1.14}$. Figure 5.5 shows the magnetic field energy profile obtained by substituting the magnetic field strength $B_{\rm eq}$ and the jet width $W(r)$. The fitting results are following values: region (i) $r^{-0.24\pm0.01}$, (ii) $r^{-0.48\pm0.01}$, and (iii) $r^{1.04\pm0.41}$; these values are nearly consistent with theoretical values. The error estimate of fitting results are shown in Figure 5.6. It is important that the magnetic energy is rapidly increasing at downstream of the jet (region (iii)), while decreasing at region (i) and (ii). The synchrotron luminosity per unit jet length is also increasing in region (iii) (Figure 5.3). These phenomenon can be explained by considering the energetics as follows: in region (i) and (ii), the magnetic energy is converted to kinetic energy, and partially radiation energy, of the jet and then the jet is accelerated; in region (iii),

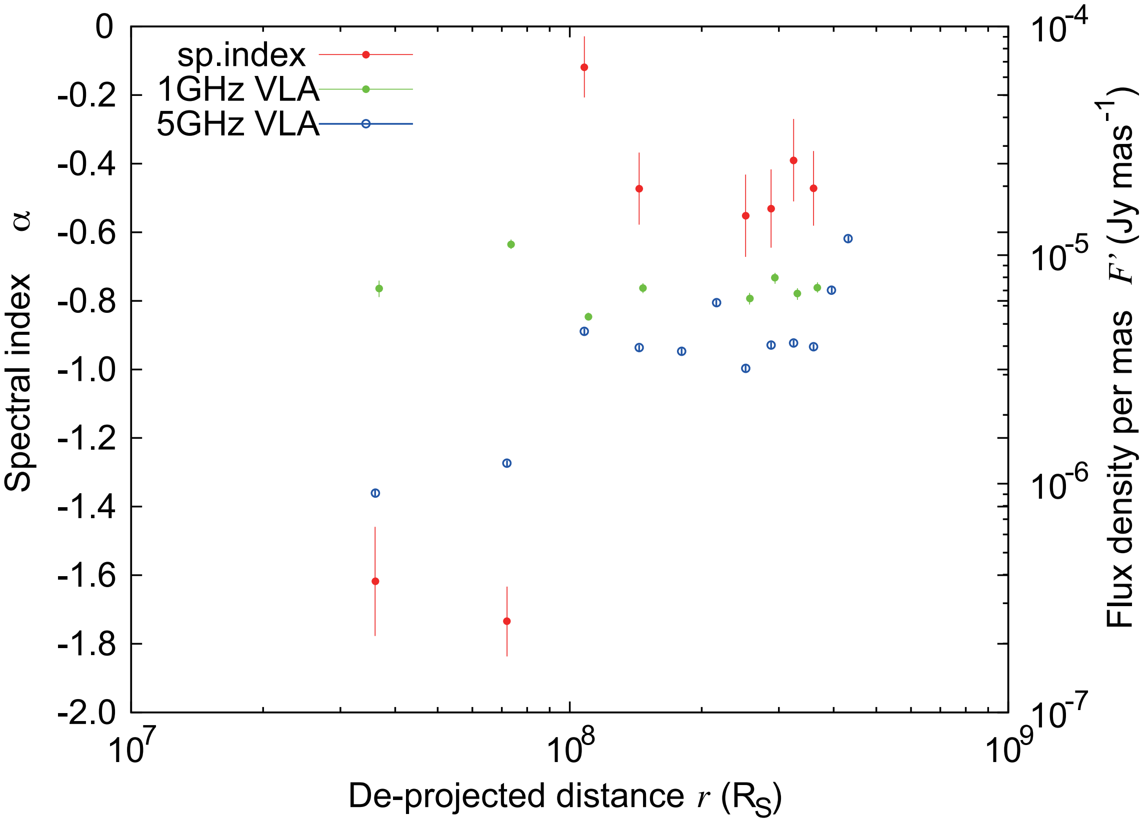

**Figure 5.1:** Measured flux density per mas and spectral index along approaching jets over VLA scales. The error of flux density was determined from root-sum-squared of the VLA flux scaling error (3%) and a slice fitting error with a double-Gaussian model (Section 2.2.2).

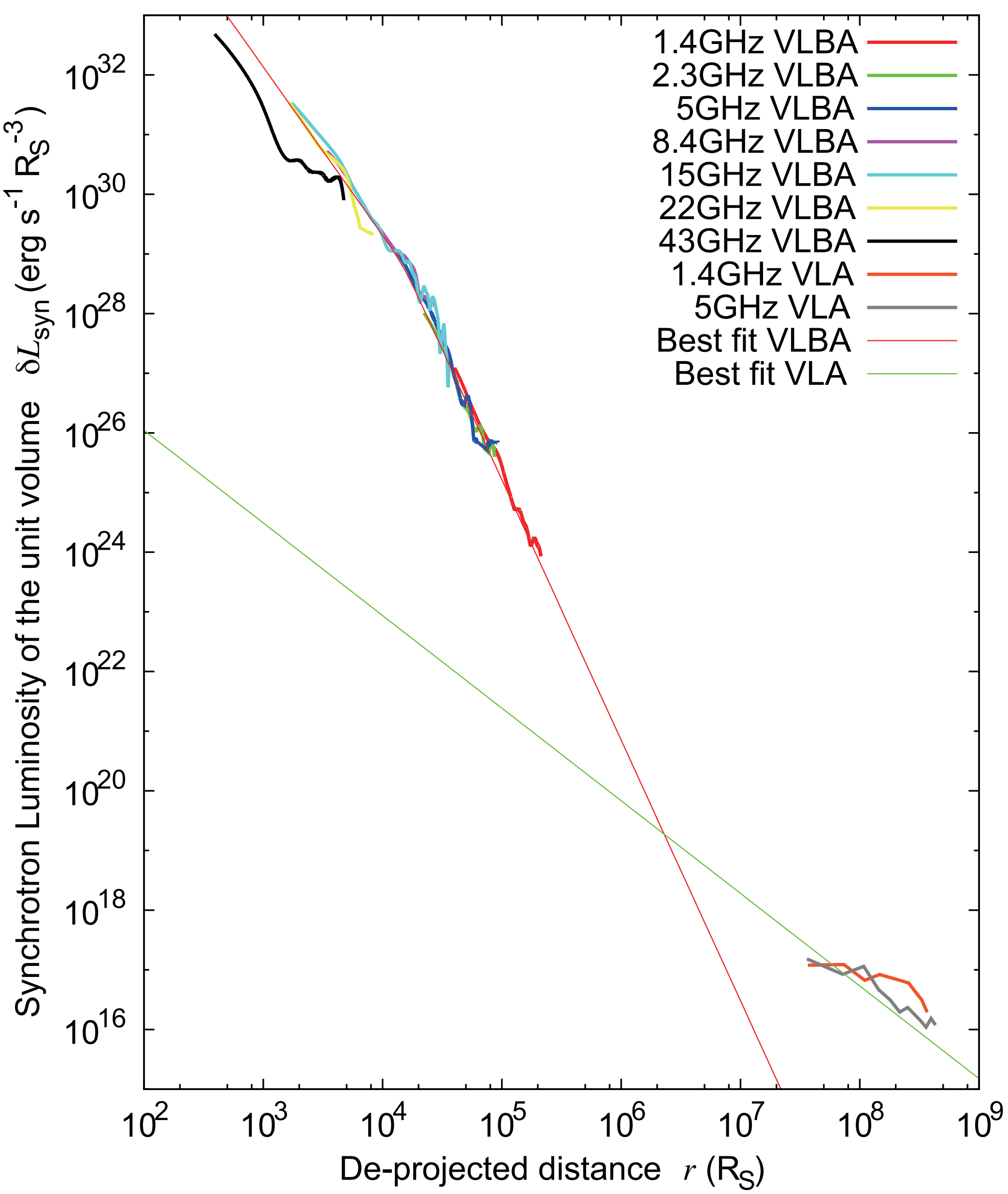

**Figure 5.2:** Radial profile of synchrotron luminosity per unit volume for approaching jet. The horizontal axis shows the distance from the central engine, taking into account the core-shift effect. The vertical axis shows synchrotron luminosity of the unit volume. Color variation describes each observed frequency; orange: 1.4 GHz with VLA, gray: 5.0 GHz VLA, red: 1.4 GHz with VLBA, green: 2.3 GHz with VLBA, blue: 5.0 GHz with VLBA, purple: 8.4 GHz with VLBA, light blue: 15 GHz with VLBA, yellow: 22 GHz, black: 43 GHz VLBA, respectively. The thin red line shows the best fit of broken power-law for the VLBA data sets without 43 GHz data; the break point is at $1.50 \pm 0.03 \times 10^4$ R$_\mathrm{S}$. The thin green line shows the best fit line for the VLA data sets.

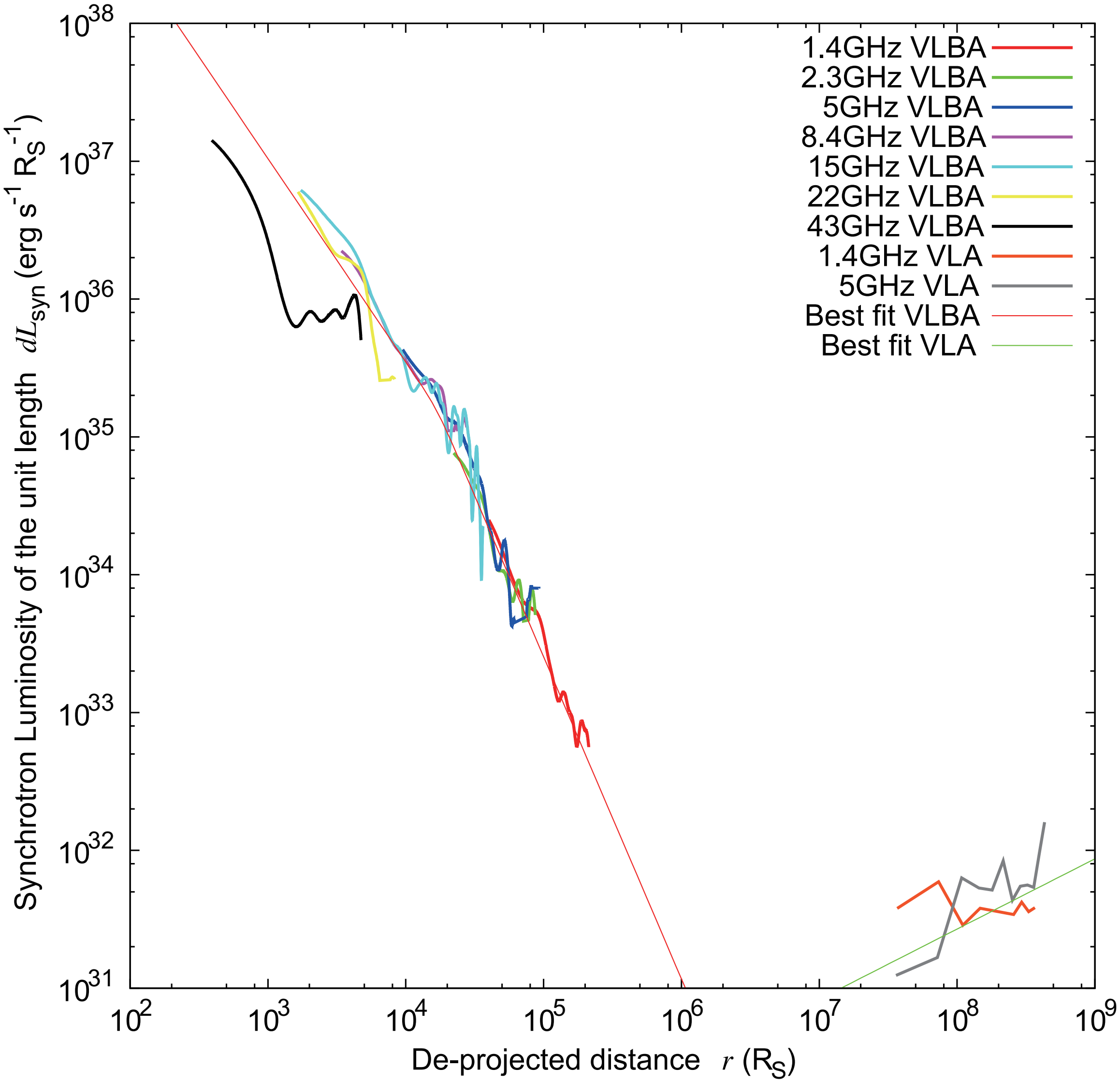

**Figure 5.3:** Radial profile of synchrotron luminosity per unit length for approaching jet. The horizontal axis shows the distance from the central engine, taking into account the core-shift effect. The vertical axis shows synchrotron luminosity of the unit length. Color variation describes each observed frequency; orange: 1.4 GHz with VLA, gray: 5.0 GHz VLA, red: 1.4 GHz with VLBA, green: 2.3 GHz with VLBA, blue: 5.0 GHz with VLBA, purple: 8.4 GHz with VLBA, light blue: 15 GHz with VLBA, yellow: 22 GHz, black: 43 GHz VLBA, respectively. The thin red line shows the best fit of broken power-law for the VLBA data sets without 43 GHz data; the break point is at $1.70 \pm 0.06 \times 10^4$ R$_{\rm S}$. The thin green line shows the best fit line for the VLA data sets.

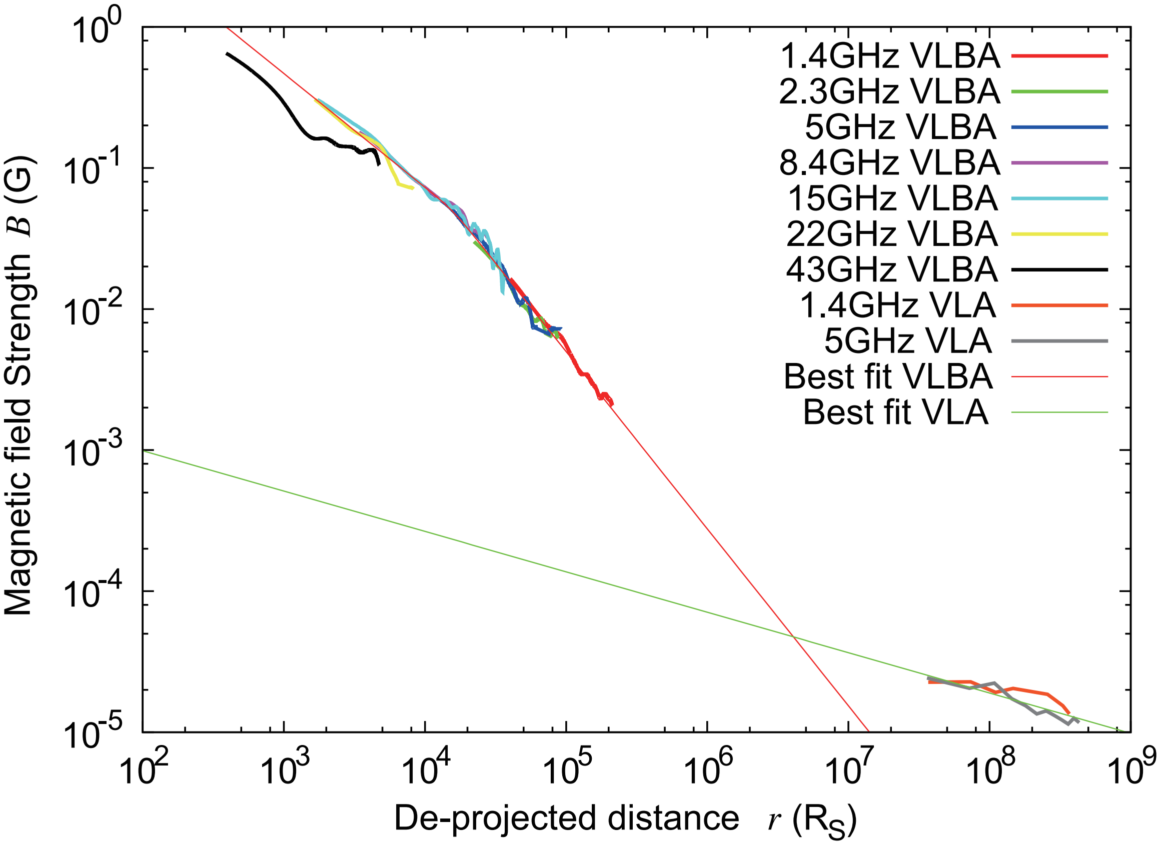

**Figure 5.4:** Radial profile of Magnetic field strength. The horizontal axis shows the distance from the central engine, taking into account the core-shift effect. The vertical axis shows magnetic field strength. Color variation describes each observed frequency; orange: 1.4 GHz with VLA, gray: 5.0 GHz VLA, red: 1.4 GHz with VLBA, green: 2.3 GHz with VLBA, blue: 5.0 GHz with VLBA, purple: 8.4 GHz with VLBA, light blue: 15 GHz with VLBA, yellow: 22 GHz, black: 43 GHz VLBA, respectively. The thin red line shows the best fit of broken power-law for the VLBA data sets without 43 GHz data; the break point is at $1.59 \pm 0.03 \times 10^4$ $R_S$. The thin green line shows the best fit line for the VLA data sets.

the jet decelerates and its kinetic energy is converted to the magnetic energy, then, electron energy and synchrotron radiation also increases with the magnetic energy as the equipartition. The Schematic view is shown in Figure 5.7. This is the first time that the jet energetics from the jet production to dissipation is observationally suggested. Even considering error, the magnetic energy is increasing in the region (iii) and presents evidence that the region (iii) is a location of dissipation of kinetic energy.

Such an overall picture throughout jets is consistent with the predictions from the theoretical point of view. During the evolution of jets, Poynting energy (magnetic energy), kinetic energy, and particle energy are expected to be exchanged each other in the jet flow. Note that the "equipartition condition" is generally mentioned on the relation between the magnetic field and particles; it is basically difficult to evaluate the relation to the kinetic energy because the kinetic energy is observationally invisible. However, this invisible form of energy plays an important role in the middle stage of jet evolution. At the first stage, a jet is launched under the magnetic dominated situation. Jet's proper motion from sub-relativistic up to superluminal apparent speed indicates a gradual acceleration, which has been observed at parsec scales through many VLBI observations as mentioned in Section 1.1.2. This is evidence for the magnetic dominated jets in this scale, and a strong indication of the conversion into kinetic energy. Second, the stage of conversion from the kinetic energy to the particle energy would be started after the magnetic energy has decreased down to near equipartition with the kinetic energy. The kpc-scale jets need for "in situ" energy dissipation to provide fast-cooling ultra-relativistic electrons responsible for synchrotron radiation frequently observed in the optical and X-ray bands. This is strong evidence from observations for the energy conversion to radiating particles in jets from, presumably, the kinetic energy that has been injected through the bulk acceleration over the parabolic streamline of jets. The particle acceleration is still under the debate, several mechanisms are proposed to explain observational results: (1) MHD instabilities being developed in a jet during its final stages of acceleration, and subsequent possible processes of (2) collisions between velocity inhomogeneities propagating down a matter-dominated jet, which is known as the internal shock scenario, or (3) the magnetic reconnection models. The magnetic reconnection models predict only the narrow energy distributions of accelerated electrons, which might be inconsistent with the observed broadband spectra. These are the possible scenarios for the mechanism of energy conversion into particles in jets.

In the energized regions of jets, i.e., from parsec scales to kpc scales before lobes, astronomers consider that the equipartition condition between the magnetic field and particles is physically feasible. One of the reasons why the energy potential profile around the minimum energy is fairly sharp (Figure 5.8). Second, systems with interacting components often tend toward equipartition. Third, observed huge energies in active radio galaxies, such as Cygnus A and AGNs investigated by this thesis, can explain only under the assumption of minimum energy (near equipartition) condition. On the other hand, at the final stage after energetically decoupled from the jet energy injection, radio lobes become evolved to the cooling phase. In this stage, the dominance of particle energy has been observed by the combination of radio and X-ray observations, such as a VLA–*Suzaku* combination (e.g., Isobe & Koyama 2015).

### 5.1.4 Interaction between Jets and Intergalactic environment

Jet pressure should be balanced with the pressure of the material surrounding the jet. In NGC 4261, there are two examples for studying the pressure of the surrounding medium, both of which are in the region corresponding to the VLA scale we investigated in this study. Kolokythas et al. (2015) examined the pressure of radio lobes radiating synchrotronically using the Giant Metrewave Radio Telescope (GMRT). O'Sullivan et al. (2011) examined the pressure of the hot intragroup medium (IGM) using the X-ray astronomical satellites *Chandra* and *XMM-Newton*. The respective results of these studies are shown in Figure 5.9 along with our results. The pressures of the radio lobes and the hot IGM are clearly different, while the jet pressure we obtained is closer to that of the hot IGM than it is to the radio lobes, even though most of the VLA scale jet is surrounded by the radio lobe. Observations of 3C84 under the VLBI Space Observatory Programme (VSOP) revealed radio lobe synchrotron radiation generated from the boundary surface between the lobe and the ambient gas (Asada et al. 2006). On the other hand, Kolokythas et al. (2015) estimated pressure by assuming that the synchrotron radiation arises within the lobe volume, and therefore that differently radiating sites were likely related to inconsistencies in their lobe pressure estimates. As the pressure of the radio lobe content is potentially balanced with the IGM pressure, the pressure of a jet penetrating a lobe would also be equivalent to the IGM pressure. Because the spatial resolution of the X-ray telescope was insufficient to measure it, there is no pressure estimate for the ambient gas in the inner VLBA region that is directly comparable to our estimate of the jet pressure.

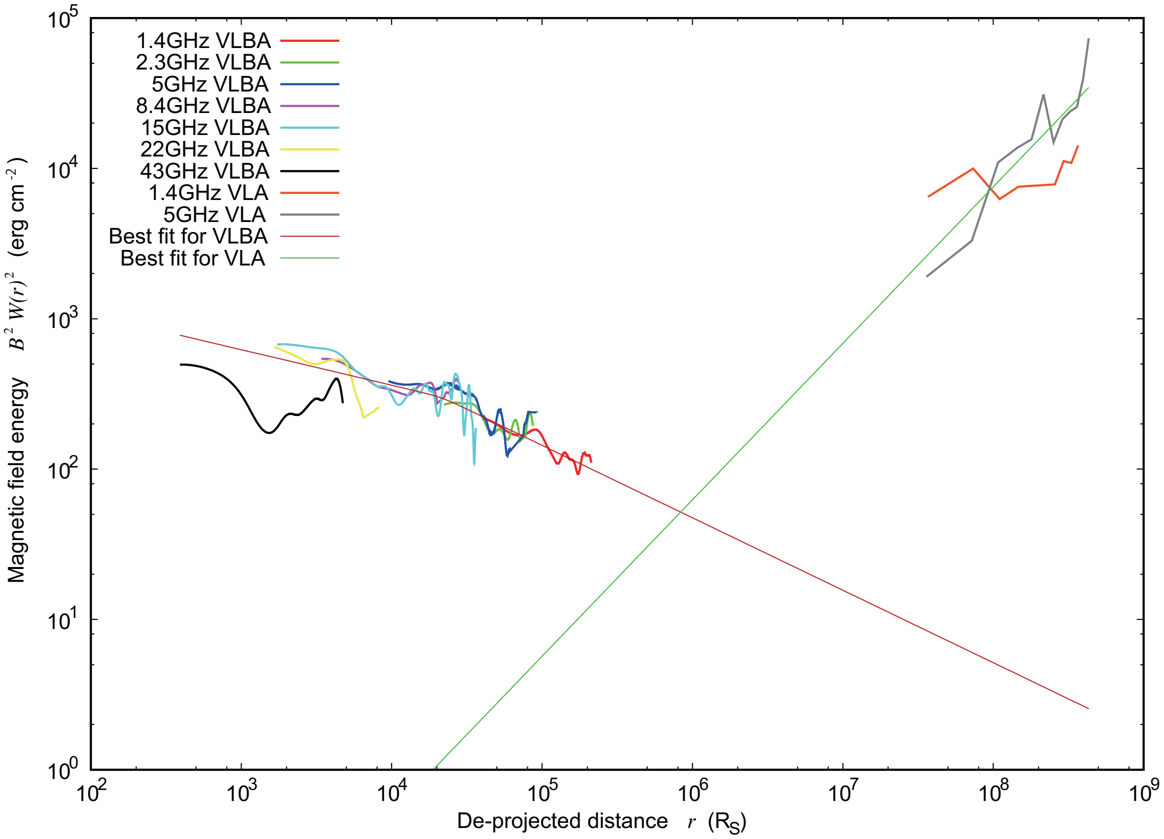

**Figure 5.5:** Radial profile of magnetic energy per unit jet length. The horizontal axis shows distance from the central engine, which is taken account for the core shift effect. The vertical axis shows magnetic field strength. Color variation describes each observed frequency; orange: 1.4 GHz with VLA, gray: 5.0 GHz VLA, red: 1.4 GHz with VLBA, green: 2.3 GHz with VLBA, blue: 5.0 GHz with VLBA, purple: 8.4 GHz with VLBA, light blue: 15 GHz with VLBA, yellow: 22 GHz, black: 43 GHz VLBA, respectively. Red thin line shows the best fit of broken power-law for the VLBA data sets without 43 GHz data. Green thin line shows the best fit line for the VLA data sets.

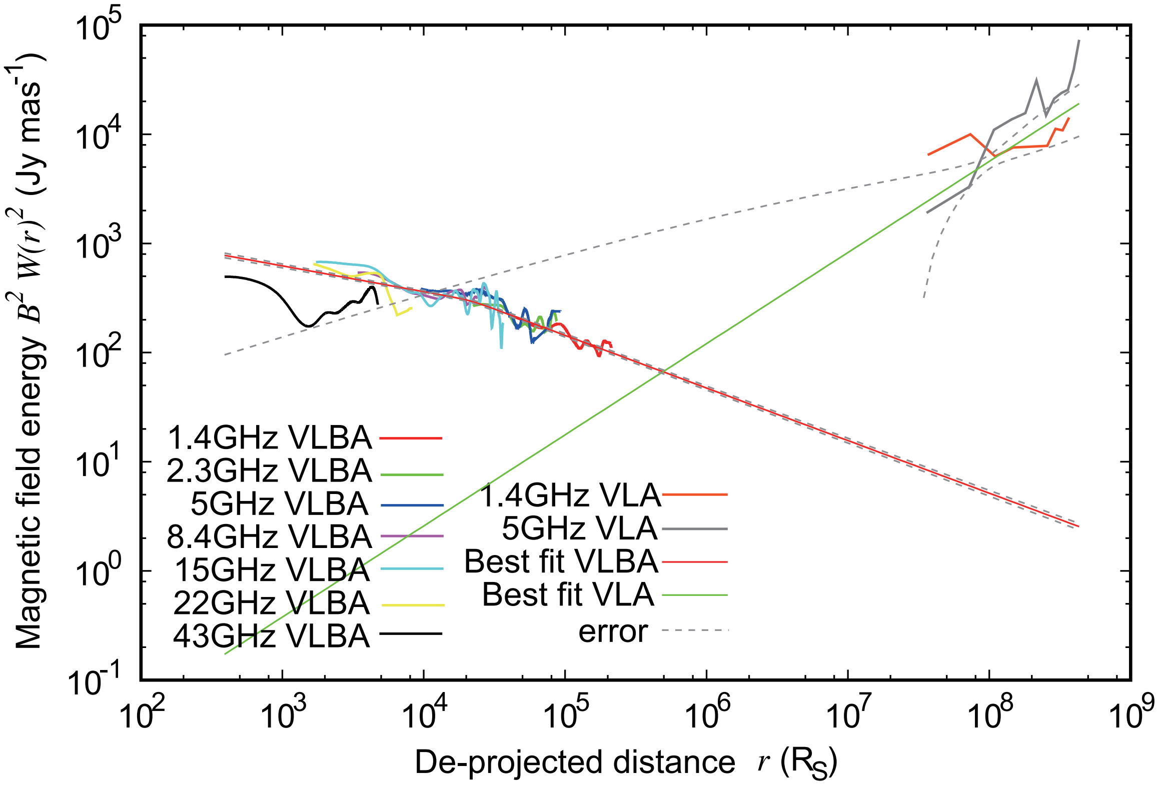

**Figure 5.6:** The error estimate of the fitting result of magnetic energy. The color variation describes each observed frequency; orange: 1.4 GHz with VLA, gray: 5.0 GHz VLA, red: 1.4 GHz with VLBA, green: 2.3 GHz with VLBA, blue: 5.0 GHz with VLBA, purple: 8.4 GHz with VLBA, light blue: 15 GHz with VLBA, yellow: 22 GHz, black: 43 GHz VLBA, respectively. Red thin line shows the best fit of broken power-law for the VLBA data sets without 43 GHz data. Green thin line shows the best fit line for the VLA data sets. The dashed lines show the error estimate of fitting results.

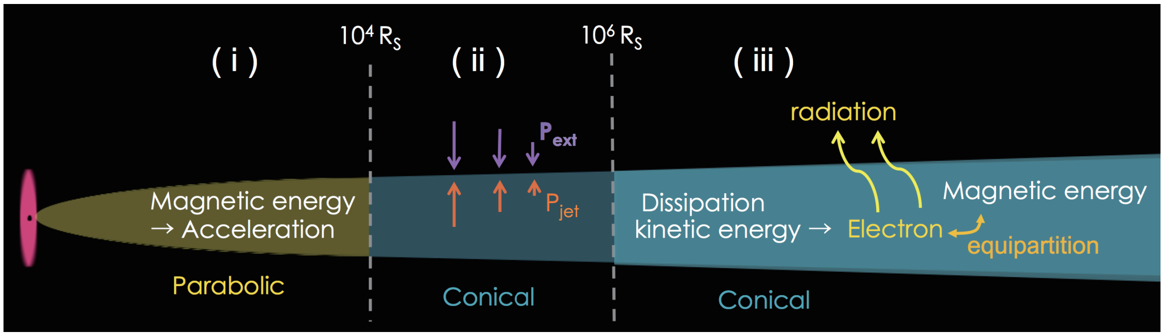

**Figure 5.7:** The magnetic field is converted to the acceleration and possibly radiative energy of the jet in region (i) and (ii). in region (iii), the jet decelerates and its kinetic energy is converted to the electron energy, then, the magnetic energy also increases with the electron energy as we assume equipartition. The increased electron energy is thrown away as radiation as can be seen in Figure 5.3.

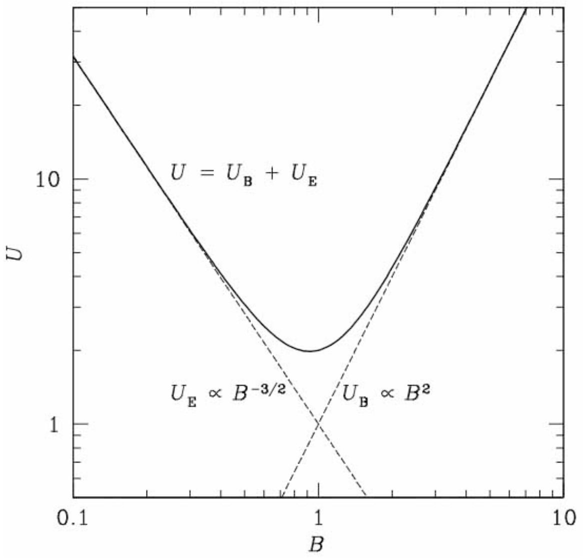

**Figure 5.8:** The total energy density of magnetic field and particles around the minimum energy.

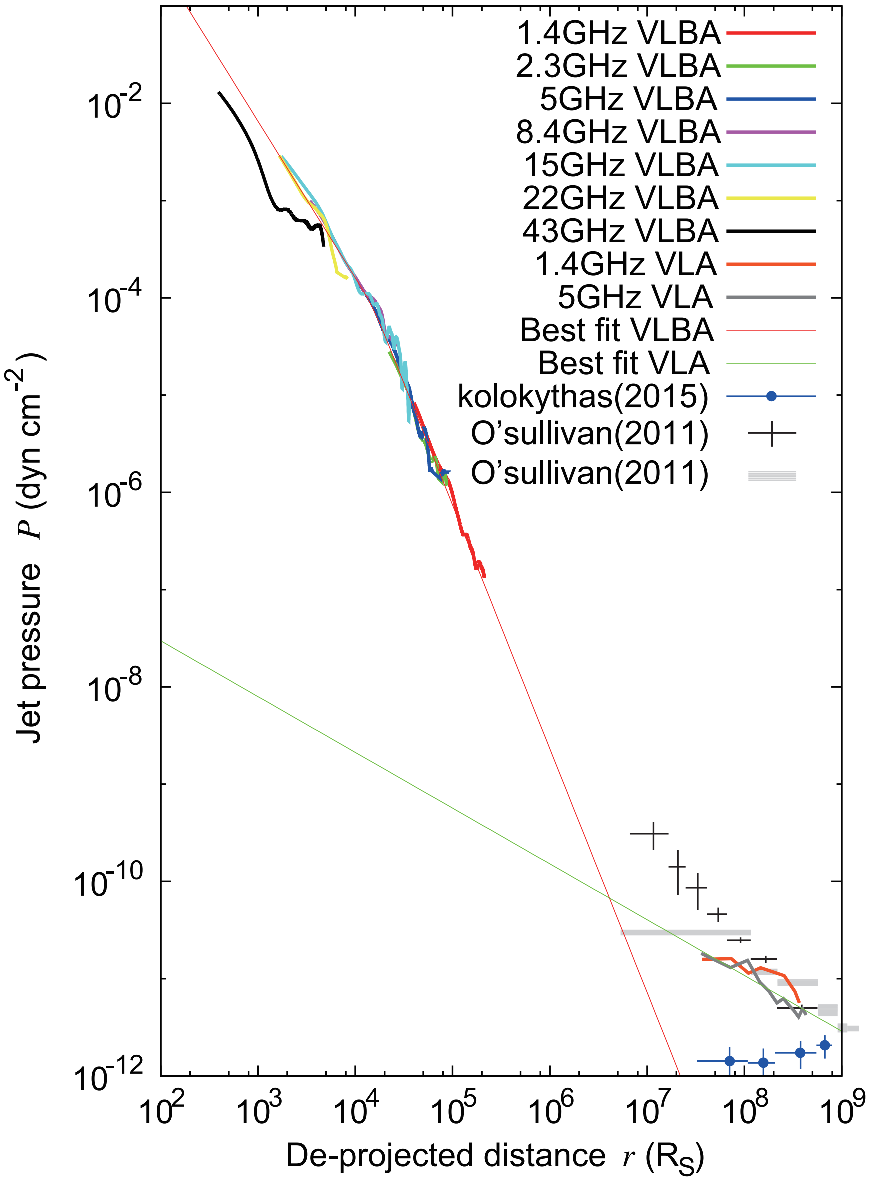

**Figure 5.9:** Radial profile of jet pressure. The horizontal axis shows the distance from the central engine, taking into account the core-shift effect. The vertical axis shows jet pressure. Color variation describes each observed frequency; orange: 1.4 GHz with VLA, gray: 5.0 GHz VLA, red: 1.4 GHz with VLBA, green: 2.3 GHz with VLBA, blue: 5.0 GHz with VLBA, purple: 8.4 GHz with VLBA, light blue: 15 GHz with VLBA, yellow: 22 GHz, black: 43 GHz VLBA, respectively. The thin red line shows the best fit of broken power-law for the VLBA data sets without 43 GHz data; the break point is at $1.54 \pm 0.03 \times 10^4$ $\mathrm{R_S}$. The thin green line shows the best fit line for the VLA data sets. The blue symbols denote the lobe pressure based on GMRT observation at 240 MHz (Kolokythas et al. 2015). The black crosses and gray region represent the pressures of the hot intragroup medium based, respectively, on the *Chandra* observation and the *XMM-Newton* observations (O'Sullivan et al. 2011).

**Table 5.1:** Results of Broken Power-law Fit to Physical Condition Profile of Jet under Equipartition

| Profile<br>(1) | $\beta^{\mathrm{i}}_{\mathrm{u}}$<br>(2) | $\beta^{\mathrm{i}}_{\mathrm{d}}$<br>(3) | $\beta^{\mathrm{i}}_{\mathrm{VLA}}$<br>(4) |
|---|---|---|---|
| $L_{\mathrm{syn}}/V(r)$ | $-2.82 \pm 0.03$ | $-4.37 \pm 0.01$ | $-1.55 \pm 0.27$ |
| $L_{\mathrm{syn}}/R_{\mathrm{S}}(r)$ | $-1.48 \pm 0.02$ | $-2.34 \pm 0.01$ | $+0.51 \pm 0.12$ |
| $B_{\mathrm{eq}}(r)$ | $-0.81 \pm 0.01$ | $-1.25 \pm 0.00$ | $-0.29 \pm 0.03$ |
| $P_{\mathrm{jet}}(r)$ | $-1.61 \pm 0.02$ | $-2.51 \pm 0.01$ | $-0.58 \pm 0.06$ |

Note. — Col. (1) Cases of fitting analyses; Col. (2) power-law index at upstream in VLBA scale; Col. (3) power-law index at downstream in VLBA scale; Col. (4) power-law index in VLA scale.

## 5.2 Comparison of jet structure among five objects

Now, I obtained five samples of jet width profile, including two objects of the previous study and three objects of the present study. Figure 5.10 represents the comparison of jet structure among five objects. Then, It become possible to discuss features of five jets such as common points and differences.

### 5.2.1 Structural transition

As shown In Figure 5.10, the four jets have a structural transition from parabolic/cylindrical to conical, while only one jet (Cygnus A) keeps parabolic shape among long spatial scale ($\sim 10^7 R_{\rm S}$). The difference between Cygnus A and the other samples is that Cygnus A is an Fanaroff-Riley type II (FR-II) jet and the rest are the FR-I type jets.

### 5.2.2 Fanaroff-Riley type I/II Dichotomy

Fanaroff and Riley classified AGN jets into two types. FR-I jet decreases as the distance from the radio core (edge dark), while FR-II jet exhibits increasing luminosity in the lobes (edge brightened). FR-II outflow is more powerful than FR-I, and makes bright edge region called hot spot which is made by shock between the outflow and interstellar medium surrounding jet. Cygnus A is one of the typical FR-II jet and other objects are FR-I jet; and only Cygnus A keeps parabolic shape mentioned above. This result can be understood that powerful FR-II jet keeps to be accelerated from the upstream to the end of the jet assuming that the jet acceleration and collimation region of the jet correspond to each other. However, Cygnus A is the first FR-II object which is measured the jet structure from the Schwarzschild radius to the galactic scale; therefore in order to confirm this theory, further FR-II jet's structure should be investigated.

### 5.2.3 Over-collimation with plasma torus

The profile at $< 1 \times 10^4 R_{\rm S}$ in NGC 1052 becomes flat, rather than parabolic, from a conical outer profile (Figure 3.14). It is necessary to explain its physical cause.

A relatively flat profile had also been reported in the jet-width radial profile of very young radio galaxy 3C 84 (Nagai et al. 2014), although the measurement was limited to the range of $\sim 10^4$–$10^5 R_{\rm S}$ in that research on the basis of a VLBA 43-GHz observation. In the observed scale, a limb brightening structure is apparent, with a nearly cylindrical flow showing a power-law index of $a = 0.25 \pm 0.03$. If the magnetized jets are collimated by the pressure of external medium as theoretical studies suggest,

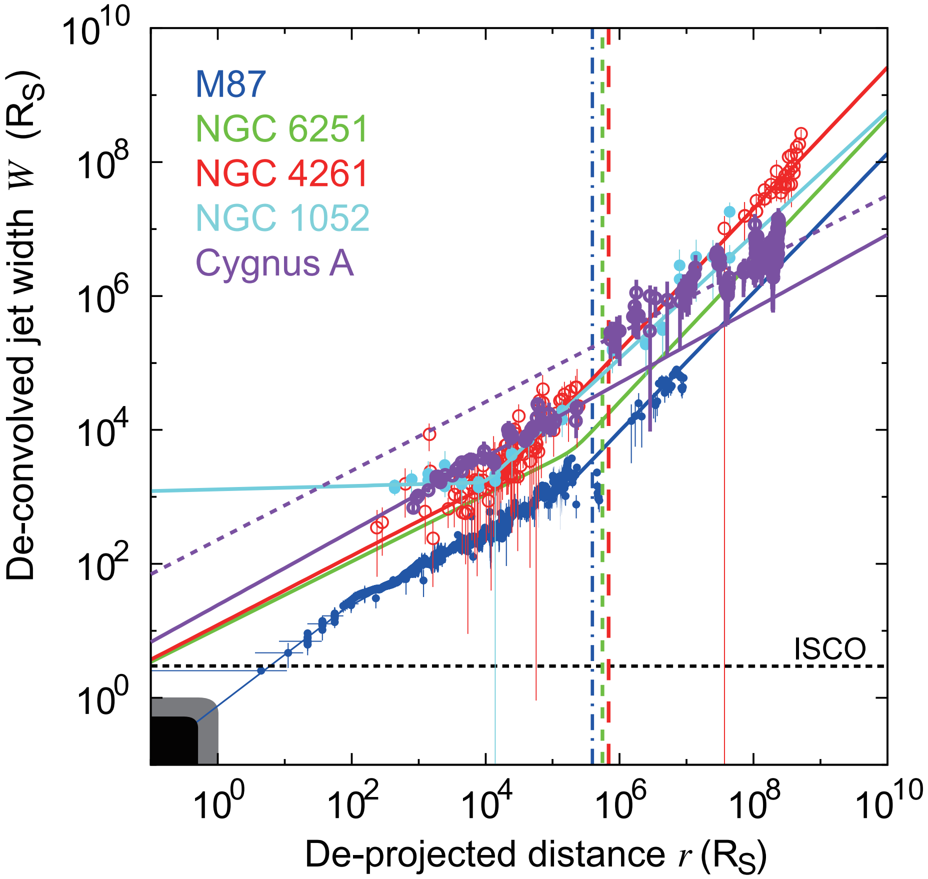

**Figure 5.10:** Comparison of jet structure among five objects. Color variations represent the objects; blue:M87, green: NGC 6251, red: NGC 4261, light blue: NGC 1052, purple: Cygnus A.

the pressure gradient of ambient gas is required to be $b < 2$, where the pressure radial profile $p_{\mathrm{ism}} \propto r^{-b}$ (Komissarov et al. 2009), to make an over-collimation with the power-law index of the jet-width profile $a < 0.5$. Nagai et al. (2014) discussed that the over-collimation in 3C 84 could be responsible for the ambient pressure gradient shallower.

The common property of NGC 1052 and 3C 84 as AGNs is that these nuclei are surrounded by the pc-scale plasma torus/disk causing strong free–free absorption. For 3C 84, non-detection of counter jet at low frequencies cannot be explained not only by the Doppler beaming effect but also by free-free absorption due to a plasma disk, as reported in Walker et al. (2000). On the other hand, for NGC 1052 Kameno et al. (2001) found the presence of a torus-like free–free absorber around the nucleus in addition to ambient absorbers, suggesting a transition from spherical radial accretion flow to rotational accretion orbits (see also Kameno et al. 2003, 2005; Sawada-Satoh et al. 2008). The physical size of the torus in NGC 1052 is estimated to be $\sim 0.5$ pc in radius (Kameno et al. 2001), corresponding to $\sim 3 \times 10^4 R_{\mathrm{S}}$; this is consistent with the locations of transition at $\sim 1 \times 10^4 R_{\mathrm{S}}$ in the jet-width profiles. Hence, weconsider that the external pressure by the plasma torus/disk is attributed to the observed over-collimation making cylindrical shapes in the innermost jets of NGC 1052, as well as 3C 84. After escaping the area of the plasma torus, at the outer region, the jets would become conically expanding in the much steeper profile in ambient medium of the host galaxy and/or become over-pressured by sufficient magnetic dissipation.

### 5.2.4 Black hole spin powered or disk driven?

The observational approach from the investigations of jet-width radial profile potentially provide us crucial evidence of the jet driving source. However, as shown in Figure 5.10, structural information is absent in the range of $10^0$–$10^2 R_{\mathrm{S}}$ or $-10^3 R_{\mathrm{S}}$ for NGC 4261, NGC 1052, and Cygnus A the present study has added. For M87 and NGC 6251 that the previous studies have investigated (Hada et al. 2013; Tseng et al. 2016), their jet driving sources also remain inconclusive. At close to the black hole in M87, a possible transition at $\sim 50 R_{\mathrm{S}}$ from the parabolic streamline with $W(r) \propto r^{0.58}$ to relatively conical one with $W(r) \propto r^{0.8}$ toward the upper stream is based on scarce data and an uncertain fit. Even with the nearest AGN, M87, it is not clear whether the jet is being driven by the black hole spin or the accretion disk. Although the present study has largely increased the number of jet-width profiles in this research field, the approach to the jet driving source with this technique has not achieved yet. To examine the jet width in $10^0$–$10^2 R_{\mathrm{S}}$ would require further angular resolutions of at higher frequencies.

### 5.2.5 Difference in Jet width

I found that the jet width of NGC 4261, NGC 1052, and Cygnus A is one order of magnitude thicker than M87 and NGC 6251. These two groups have a difference in their inclination angle. The thicker jets have larger inclination angle and slenders have smaller one. Thus, I investigated the correlation between jet width and inclination angle in Figure 5.11. It can be confirmed that the larger the inclination angle, the thicker the jet width. This phenomenon can be explained by using theoretical jet model called spine-sheath. The jet structure of Cygnus A can also be explained with the same model, so I will explain them together in Section 5.2.6.

### 5.2.6 Multi layered jet structure and Doppler beaming effect

For the discontinuity observed in the jet width profile of Cygnus A, it is necessary to explain the mechanism that causes that phenomenon. The radial distance of the discontinuity $\sim 5 \times 10^5$ $\mathrm{R_S}$ is close to the Bondi radius for Cygnus A, $0.078^{+0.165}_{-0.048}$ kpc (Fujita et al. 2016), corresponding to $\sim 3 \times 10^5$ $\mathrm{R_S}$. The transitions of jet-width profiles have also been discovered near the Bondi radii in M87 and NGC 6251 (Asada & Nakamura 2012; Tseng et al. 2016); relationship with changes in profiles of external pressures has been discussed in these cases. However, the case of Cygnus A where the power-law index does not change is quite different from these cases which transition from parabolic to conical streamlines. Additionally, note that the profile discontinuity occurs at the boundary between the VLBA and VLA observation ranges (Section 4.3.1).

Jumping only in width while maintaining parabolic shape requires more than one component for jet constitution. It is reminiscent of stratified jet with multi-layered flow (Ghisellini et al. 2005). We propose a scenario in kpc scales an outer layer jet are predominantly apparent and in pc scales a different inner layer is observed. At the VLBI scales, a limb-brightened structure in the upperstream of 2 mas in the both sides, suggesting the presence of a further inner layer in addition. That is, at least three layers are required for the jet. We argue that the combination of two effects as follows contributes to the selection of an observable jet layer at different radial scales.

The first effect is Doppler beaming/debeaming. Cygnus A is a highly inclined FR-II type radio galaxy; at least mildly relativistic flow would be consistent with the observed jet-to-counterjet surface brightness ratio (Krichbaum et al. 1998). The layer of high velocity flow disappears by Doppler Debeaming and the radiation from the later flow prevails. Our observations also indicate that the jet width of Cygnus A ($i < 74.5$; Boccardi et al. 2016b) is comparable with the NGC 4261 one (Nakahara et al. in press, $i$ =63 deg; Piner et al. 2001), which are significantly wider than those of M87 (Asada & Nakamura 2012, $i = 14$ deg; Wang & Zhou 2009) and NGC 6251

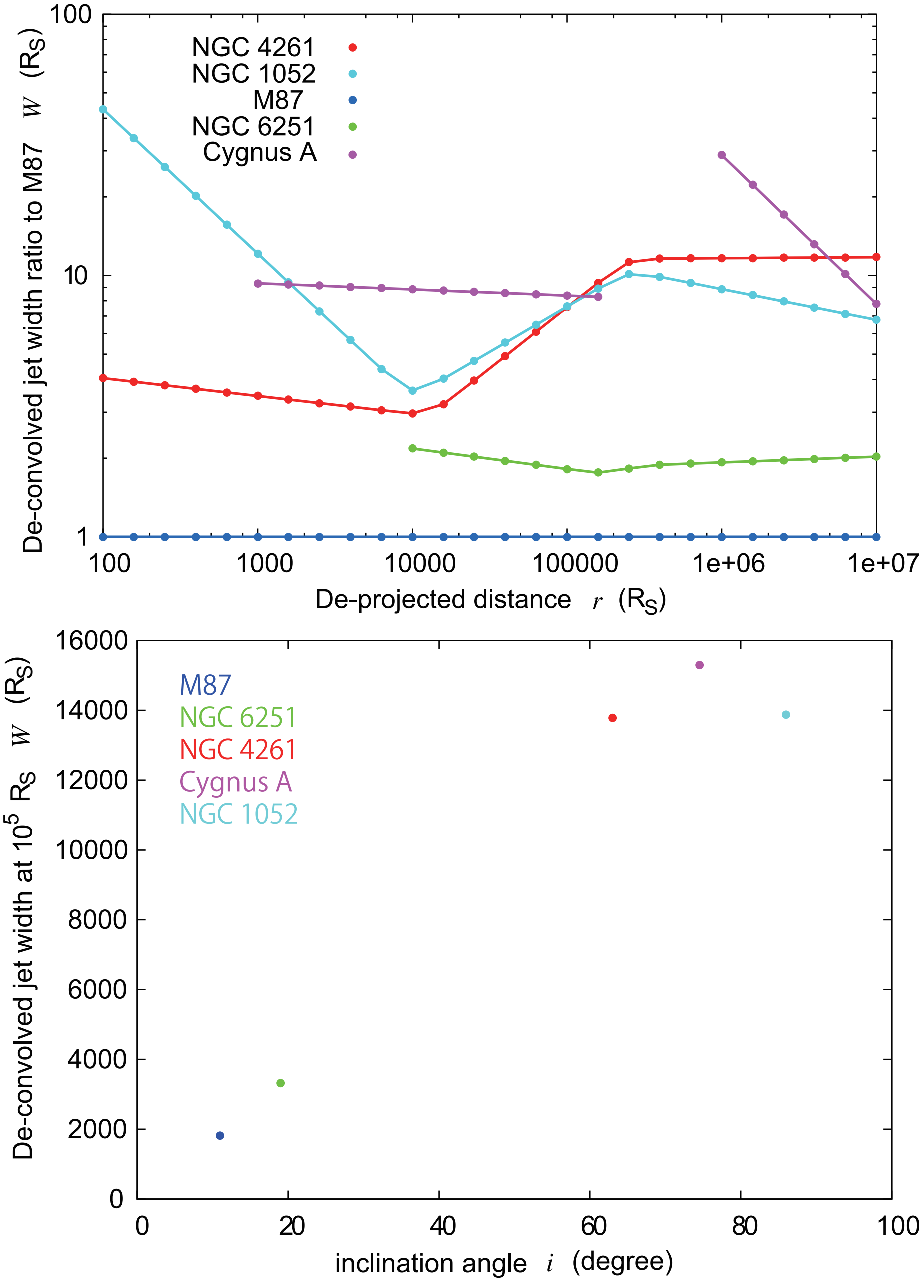

**Figure 5.11:** Relation between jet width and inclination angle. (Upper) Jet width ratio to M87. The horizontal axis shows de-projected distance from the core. The vertical axis shows Ratio of M87 jet width to each other objects. Color variation represents each objects; blue: M87, green: NGC 6251, red:NGC 4261, light blue: NGC 1052, purple: Cygnus A. (Down) The jet width values at $10^5 R_S$ in the above figure are extracted and displayed in the vertical axis. The horizontal axis shows inclination angle. Color variation is the same as the above figure's.

(Tseng et al. 2016, $i = 19$ deg; Tseng et al. 2016; Sudou et al. 2000) (I will present comprehensive comparisons elsewhere). Thus, highly inclined jets were measured to be wider. This observed trend conforms to the jet scenario with layered structure of high speed inner layer and slower outer layer.

The second effect can be attributed to the overwhelmingly different sensitivities to brightness in the VLBI and VLA images; the discontinuity was found at the boundary between the VLBI and the VLA observation regions. The VLBI and the VLA typically have brightness temperature sensitivities of $\sim 10^7$ K and $\sim 10^2$ K, respectively, which has a difference of $\sim 10^5$. The pc-scale jet were observed at a brightness temperature of the order of $\sim 10^8$ K typically, which can be assumed to be the inner fast layer. If the outer slow layer has a brightness temperature of $\sim 10^6$ K or less, this component can not be detected with the VLBI image. On the other hand, the flux contribution of slow layer could be prominent at kpc scale.

We claim this scenario in a more quantitative way. We calculated the relationship between the jet velocity of each layer and the expected brightness/flux density in the observer frame, in order to verify whether observed discontinuity can quantitatively be explained by the Doppler beaming effect and the resolution effect (Appendix A). Here we assume an inclination of $i = 74.5$ deg (Boccardi et al. 2016b), and the jet-width ratio of slow to fast layers $W_{\rm slow}/W_{\rm fast} = 6$ (Section 4.3.2), the intrinsic brightness ratio $T^{\rm slow}_{\rm Bint}/T^{\rm fast}_{\rm Bint} = 0.01$, and a spectral index of $\alpha = -0.7$. The calculation results are shown in Figure 5.13, and Figure 5.12 shows the schematic view of the jet. The parse scale is the region where the jet acceleration in the parabolic streamline has just begun. VLBI observations has revealed the velocity field with a gradual acceleration depending on radial distances from the nucleus in Cygnus A by proper motion measurements (Krichbaum et al. 1998; Bach et al. 2002). The innermost jets showed a changing bulk Lorentz factor of $\Gamma \approx 1.3$–$2.3$ with acceleration (Boccardi et al. 2016b). We assume the VLBI jets is a fast layer of the stratified jet. On the basis of Figure 5.13 (a), a bulk Lorentz factor of $\Gamma \sim 2$ for the fast layer implies a very small brightness ratio of the order of 0.01. This indicates that the slow layer cannot be detected in VLBI images with an image sensitivity of $\sim 10^7$ K, whereas the fast jets are in the order of $\sim 10^8$ K. Therefore, in this condition, it is likely that only the emissions from the fast layer have been imaged in VLBI images for the pc-scale jets of Cygnus A. On the other hand, at kpc scales, the jets have potentially been accelerated significantly through the parabolic streamline. Figure 5.13 (b), the expected flux ratio of the slow layer to the fast layer, shows that if the Lorentz factor in the fast layer exceeds $\sim 10$ the slow layer predominantly contributes to the observed flux density. This result can be ascribable to Doppler deboosting on the fast layer of highly inclined jet, in addition to a larger emitting surface of the slow layer. Hence, the jet width at kpc scales should be observed wider than that at pc scales using VLBIs. At the

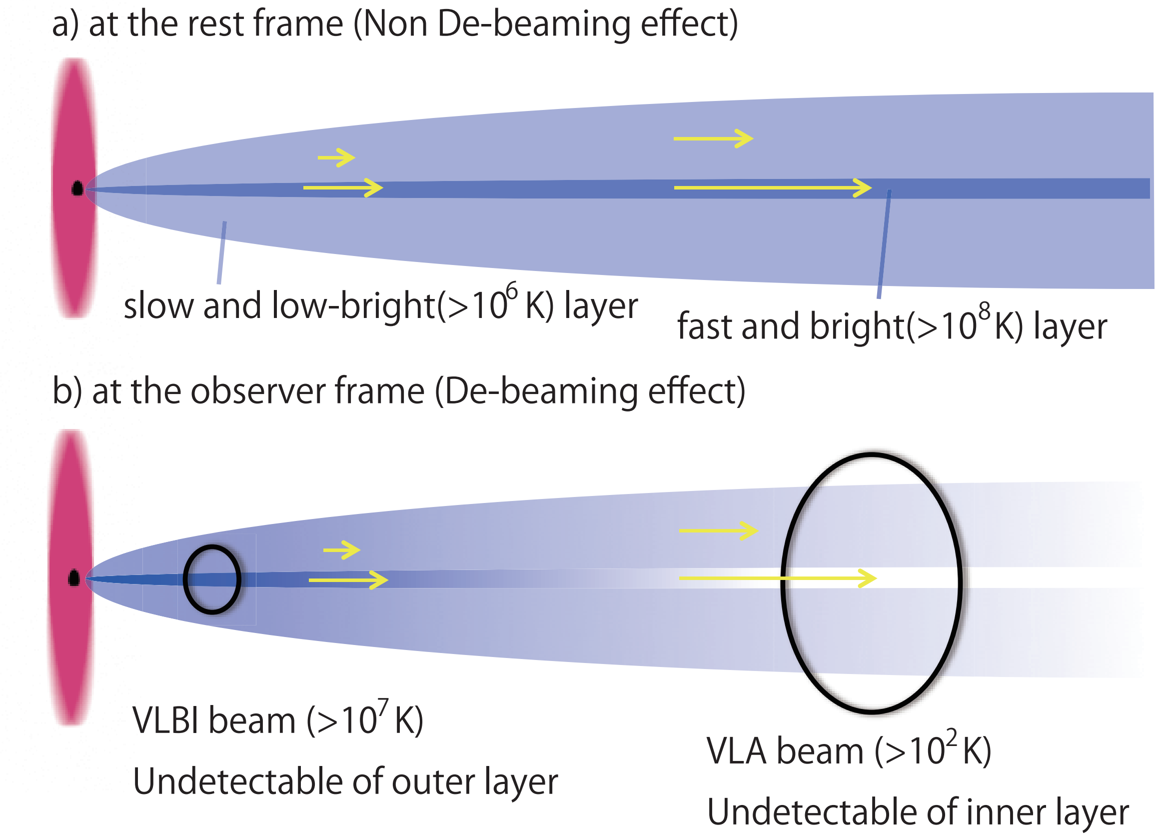

**Figure 5.12:** The schematic view of the multi-layered jet. I assume the initial condition of the jet: a) the outer layer is a slow and low-brightness ($< 10^6$ K) flow and the inner layer is a fast and high-brightness ($> 10^8$ K) flow at the rest frame. b) expected appearance of the Cygnus A jet at the observer frame. The inclination angle of Cygnus A is $\sim 74.5°$. The inner layer is still bright at the VLBI scale because the jet is not so accelarated, while it gets dim at the VLA scale due to the Doppler de-beaming effect.

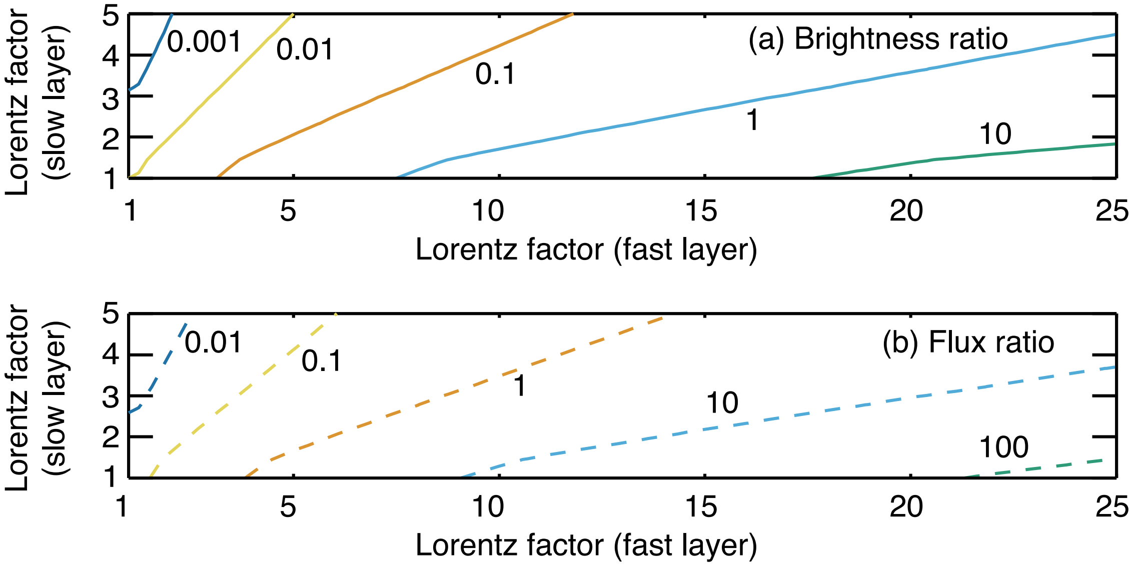

**Figure 5.13:** Contour maps of brightness ratio and flux ratio of slow layer to fast layer depending on Lorentz factors. We assume the intrinsic brightness ratio $T_{\rm Bint}^{\rm slow}/T_{\rm Bint}^{\rm fast} = 0.01$ and an inclination of 74.5 deg. (a) Expected brightness ratio $T_{\rm Bobs}^{\rm slow}/T_{\rm Bobs}^{\rm fast}$ at the observer frame. (b) Expected flux ratio $F_{\rm obs}^{\rm slow}/F_{\rm obs}^{\rm fast}$ at the observer frame. The jet-width ratio $W_{\rm slow}/W_{\rm fast}$ is set to 6.

same time, it is evidence that the kpc scale jet is sufficiently accelerated to $\Gamma = 10$ or higher, which is consistent with the fact that the parabolic shape continues up to this radial scale. Furthermore, a slightly wider jet width in the counter jets, which is revealed by our study (Figure 4.6), can also be explained with this framework. The Doppler deboosting affects more strongly, resulting that the outer layer becomes relatively more significant and a wider jet width would be apparent in the observer frame in the counter side.

# Chapter 6

# Conclusion: comprehensive picture of jet evolution over $10^1$–$10^9 R_S$

The observational study in this doctoral thesis focuses on the radial profile of jet width at the radial distances beyond the sphere of gravitational influence of the central black holes (typically $\sim 10^5 R_\mathrm{S}$ as Bondi radii) from the Schwarzschild scale. I illustrate here comprehensive picture of jet evolution over $10^1$–$10^9 R_S$ on the basis of the three nearby AGNs (NGC 4261, NGC 1052, and Cygnus A) that were investigated by the present study in addition to M87 and NGC 6251 that were reported by the previous studies by the other authors.

Transitions from parabolic to conical streamlines of jets were found in all the four FR I. This discovery suggests that the jet acceleration mechanism by collimation plays a universal role in FR-I AGNs. However, note that the transition in the NGC 4261 jet was found at $\sim 10^4 R_\mathrm{S}$, which does not coincide with the Bondi radius, unlike the cases of M87 and NGC 6251. To establish the theoretical picture for magnetized jets collimated by external pressure, the radial profile of pressure distribution in the core region of host galaxy should be estimated more precisely on the basis of higher angular resolutions in X-rays.

One FR-II AGN was included in the sample, and showed a unique property in the jet width profile. No transition was found throughout the radial distances ranging from $\sim 10^3$ to $10^9 R_\mathrm{S}$. A parabolic shape maintains up to this large scale. It is noteworthy that an apparent discontinuity by a jump roughly one order of magnitude in jet width. The location of the discontinuity coincides with the boundary of VLBI observational scale and VLA one. This surprising property can be explained by the combination of Doppler-debeaming effect and the limited sensitivities of telescopes in the framework of the multi-layered structure in a stratified jet scenario for this highly inclined AGN.

The framework of the stratified jet can also understand another discovery that the scale factor of jet width among AGNs is apparently correlated with inclination angle. Doppler-beaming/debeaming effect can explain well this phenomenon if the high-brightness inner layers are accelerated in streamlines and dominated by outer layer flows, which are slower and not so deboosted. Degree of this effect is primarily determined by viewing angle of jets. I consider it is a reason why the jet widths of NGC 4261, NGC 1052, and Cygnus A are globally wider than those of M87 and NGC 6251.

The present study additionally focused on counter jets by adding AGNs with two-sided jets to the sample for the first time. Almost perfect symmetry in terms of the radial profiles of jet width has been confirmed for all the two-sided AGN sample, which consists of NGC 4261, NGC 1052, and Cygnus A. This property suggests a universal mechanism in which the collimation and expansion of the magnetized jet is globally regulated by the pressure profile in the host galaxies and intragalactic medium. To verify the universality, a larger number of sample is required to investigate.

As a new attempt in this field of research, this PhD thesis estimated the development of physical parameters over a very wide range in the NGC 4261 jet. This estimation was made possible by combining the measurement of radiation profile with that of jet width profile. The radial profile of radiation along the jet includes two transitions at $\sim 10^6 R_\mathrm{S}$ in addition to at $10^4 R_\mathrm{S}$ that coincides with the transition found in the jet-width profile. Under the assumption of equipartition condition in synchrotron plasma, I showed the physical jet conditions in terms of synchrotron luminosity per unit volume (synchrotron emissivity), synchrotron luminosity per unit length, strength of magnetic field, jet pressure, and magnetic energy per unit length. I found that the magnetic energy in the jet was consumed through parabolic and conical streamlines (in which the magnetic energy are probably used for jet bulk acceleration); subsequently, the kinetic energy of the accelerated jet was converted again to a magnetic field (presumably by deceleration in the jet flow) at the kpc scale and dissipated as synchrotron radiation. The jets magnetic pressure is eventually consistent with the ambient pressure of intragalactic medium at a large scale. The detailed investigation for the NGC 4261 jet provide us more comprehensive understanding of the physical evolution of jets throughout from the Schwarzschild scale to the intragalactic scale.

# Chapter 7

# Future prospects

- The research method of jet using "jet width" and "radiation" profiles developed in this research is powerful. However, the latter has been applied to only one sample yet. I will increase the number of examples of measuring the physical parameters of jet by using the research method using the combination.
- Correlation of "jet width" vs. "Inclination" is a relationship between fundamental parameters of AGNs. It is an amazing discovery in this field. It is required to extend the number of samples from 5 to $\sim 10$ objects to confirm the universality of this phenomenon.
- There was a surprising discovery of the jump in the jet width profile in Cygnus A. It is the only a sample of FR-II type jet, so I will increase the number of FR-II samples to confirm whether that phenomenon is common in FR-II jets or not.
- This research suggested that the structural transition of the FR-I jets occurs on the scale of $\sim 10^4$–$10^6 R_\mathrm{s}$. Next, we need to find out what in this characteristic distance appears this phenomenon. The location of structural transition is close to the Bondi radii or the boundary of the sphere of gravitational influence; the relevance of these radii should be examined.
- In order to investigate more upstream structure of the jet, VLBI data obtained at higher frequencies by VLBI observations, such as the Event Horizon Telescope (EHT), the balloon-borne VLBI or space-VLBI are necessary.
- I made the first discovery of interstellar broadening associated with an extragalactic center (NGC 1052). I would like to investigate that phenomenon can be universally found in other objects that are shrouded by a high density plasma torus such like 3C 84.

# Acknowledgments

I owe this thesis to many people on supports, suggestions and helps.

Firstly, I acknowledge to Yasuhiro Murata, my supervisor, who has guided and encouraged me to write this doctor thesis. I feel myself fortunate to be given his valuable advice and knowledge about astrophysics and observation equipment. I am very grateful for Akihiro Doi, who provided much advice throughout writing of this thesis. I have learned a lot of things from his strict attitude for deriving and treating scientific results. I wish to acknowledge to Kazuhiro Hada, who taught me principles of techniques on data analysis.

Many thanks for collaborators, especially Masanori Nakamura, who always gave me helpful comments and discussion. We are grateful to C.C. Chueng, S. Sawada-Satoh, and S. Kameno who kindly offered us the data. We also acknowledge M. Birkinshaw, D. M. Worrall, H. Nakanishi, and M. Honma for helpful advices for this study.

The VLBA and VLA are operated by the National Radio Astronomy Observatory, which is a facility of the National Science Foundation operated under cooperative agreement by Associated Universities, Inc.

This study was partially supported by the Sasakawa Scientific Research Grant from The Japan Science Society and by Grants-in-Aid for Scientific Research (B) (24340042, AD) from the Japan Society for the Promotion of Science (JSPS).

The authors gratefully acknowledge the VSOP Project, which is led by the Japanese Institute of Space and Astronautical Science in cooperation with many organizations and radio telescopes around the world.

We have made extensive use of the VLA, VLBA, the VLA archive, NVSS and FIRST data of the National Radio Astronomy Observatory (NRAO) that is a facility of the National Science Foundation operated under cooperative agreement by Associated Universities, Inc. This research has made use of the NASA/IPAC extragalactic database (NED), which is operated by the Jet Propulsion Laboratory, Caltech, under contract with NASA.

And I would like to thank colleagues and friends. Finally, I would acknowledge my father, mother and dog Taisuke for their great support since my birth.

# Appendix A

# Doppler beaming effect

A Lorentz factor and a Doppler factor are defined as

$$\Gamma \equiv \frac{1}{\sqrt{1-\beta^2}}, \tag{A.1}$$

$$\delta \equiv \frac{1}{\Gamma(1-\beta\cos i)}, \tag{A.2}$$

where $\beta \equiv v/c$ ($v$ and $c$ are the speeds of the source and light, respectively), $i$ is the jet viewing angle, which is the angle between the direction of the source velocity and our line of sight (Ghisellini et al. 1993, Appendix B).

Assuming the spectral index $\alpha$, where $S_\nu \propto \nu^{+\alpha}$, $S_\nu$ is the flux density at the frequency $\nu$, the brightness in a continuous jet in the observer frame is expected to be boosted from that in the rest frame by a factor of $\delta^p$, where $p = 2 - \alpha$ (Ghisellini et al. 1993); note that when considering the flux density instead of the brightness in a jet blob $q = 3 - \alpha$ is applied (Rybicki & Lightman 1979). For Cyngus A's jets, weapply $p = 2 - \alpha$ and $\alpha = -0.7$.

For stratified jets in Cygnus A, we consider the ratio of brightness temperatures of a slow layer to a fast layer. Given the intrinsic brightness ratio $T_{\rm Bint}^{\rm slow}/T_{\rm Bint}^{\rm fast}$, the expected brightness ratio in the observer frame is

$$\frac{T_{\rm Bobs}^{\rm slow}}{T_{\rm Bobs}^{\rm fast}} = \frac{T_{\rm Bint}^{\rm slow}}{T_{\rm Bint}^{\rm fast}}\frac{\delta_{\rm slow}^{p}}{\delta_{\rm fast}^{p}} \tag{A.3}$$

$$= \frac{T_{\rm Bint}^{\rm slow}}{T_{\rm Bint}^{\rm fast}}\left(\frac{\Gamma_{\rm slow}-\sqrt{\Gamma_{\rm slow}^2-1}\cos i}{\Gamma_{\rm fast}-\sqrt{\Gamma_{\rm fast}^2-1}\cos i}\right)^{-p}. \tag{A.4}$$

Next, we consider the ratio of flux densities of a slow layer to a fast layer. The flux density from a jet with the deconvolved transverse width $W$ is expected to be

$S_\nu = T_\mathrm{B} W \theta \delta^p$, where $\theta$ is the spatial resolution along the jet axis. Then, the expected flux ratio in the observer frame is

$$\frac{S_\mathrm{obs}^\mathrm{slow}}{S_\mathrm{obs}^\mathrm{fast}} = \frac{T_\mathrm{Bint}^\mathrm{slow}}{T_\mathrm{Bint}^\mathrm{fast}} \frac{W_\mathrm{slow}}{W_\mathrm{fast}} \frac{\theta}{\theta} \frac{\delta_\mathrm{slow}^p}{\delta_\mathrm{fast}^p} \tag{A.5}$$

$$= \frac{W_\mathrm{slow}}{W_\mathrm{fast}} \frac{T_\mathrm{Bobs}^\mathrm{slow}}{T_\mathrm{Bobs}^\mathrm{fast}}. \tag{A.6}$$

# Appendix B

# The error estimate of a broken power-law fit

In order to present the range of robustness in broken power-law fitting, an error estimate based on the principle of error propagation was derived and superimposed on Figures 2.16, 2.20, 3.15, and 5.6.

The fit function with a broken power-law is defined as

$$f(r) = f_0 \, 2^{\frac{a_{\mathrm{u}}-a_{\mathrm{d}}}{s}} \left(\frac{r}{r_{\mathrm{b}}}\right)^{a_{\mathrm{u}}} \left(1 + \left(\frac{r}{r_{\mathrm{b}}}\right)^{s}\right)^{\frac{a_{\mathrm{d}}-a_{\mathrm{u}}}{s}} . \tag{B.1}$$

Note the parameter of sharpness $s$ is fix to 10 throughout this thesis, and no fitting error is considered. The error estimate of Eq. (B.1) can be generated by

$$\langle \delta f \rangle = \sqrt{\left(\frac{\partial f}{\partial f_0}\delta f_0\right)^2 + \left(\frac{\partial f}{\partial a_{\mathrm{u}}}\delta a_{\mathrm{u}}\right)^2 + \left(\frac{\partial f}{\partial a_{\mathrm{d}}}\delta a_{\mathrm{d}}\right)^2 + \left(\frac{\partial f}{\partial r_{\mathrm{b}}}\delta r_{\mathrm{b}}\right)^2}, \tag{B.2}$$

where $\delta f_0$, $\delta a_{\mathrm{u}}$, $\delta a_{\mathrm{d}}$, and $\delta r_{\mathrm{b}}$ are the $1\sigma$-error components for the determined parameters of $f_0$, $a_{\mathrm{u}}$, $a_{\mathrm{d}}$, and $r_{\mathrm{b}}$, respectively. This error estimate is also depending on $r$. As a result, the uncertainty in the two dimensional plot of (r, f(r)) can be described by the area sandwiched between $f(r) \pm \langle \delta f \rangle$.

# Appendix C

# The resolution limit

The practical spatial resolution is determined with the dependence of signal-to-noise ratio. The present study in this thesis and the previous studies by other authors (Tseng et al. 2016; Boccardi et al. 2016b) have sliced intensity pixels every approximately one-fifth of the synthesized beam size as independent measurements.

The practical spatial resolution was discussed in details by Lobanov (2005); for VLBI cases the lower limit of practical spatial resolution is expected to be

$$\theta_{\rm lim} = 2^{2-\beta/2}\theta_{\rm synth}\left(\frac{\ln 2}{\pi}\ln\left(\frac{SNR}{SNR-1}\right)\right)^{1/2}, \tag{C.1}$$

where $\theta_{\rm synth}$ is the half-power beam width of synthesized beam, $\beta$ is the power-law index of weighting function for visibilities sampled in the spatial frequency domain for interferometry. The case of uniform weighting ($\beta = 0$) is similar to the result obtained for filled aperture telescopes, and adopted in the present study and the previous studies. This formula approaches asymptotically to $SNR^{-1/2}$ proportionality at $SNR > 3$.

AGN studies using VLBIs are performed on data with $SNR > 100$ generally. However, calibration accuracy in visibility amplitude is always limited to $\sim 5\%$ typically in the case of the VLBA antennas. This leads quasi-ramdom error by the combining of ten VLBA antenna in addition to a systematic error to a flux scaling factor. Hence, $SNR$ would be limited to $\sim 20$. Eq. (C.1) suggests $\theta_{\rm lim}/\theta_{\rm synth} \sim 0.21$, i.e., approximately one-fifth of the synthesized beam. Note that self-calibration procedure used in calibration for VLBI data can reduce the residual errors relatively among antennas. Hence, this amplitude-error-limited spatial resolution is potentially on the conservative side. On the other hand, thermal noise possibly dominates the amplitude calibration error in image regions with weak emissions largely separated from the nucleus. Therefore, the adopted sampling rate of one-fifth of the synthesized beam size should be considered as a representative value.

# REFERENCES

Allen, S. W., Dunn, R. J. H., Fabian, A. C., Taylor, G. B., & Reynolds, C. S. 2006, *MNRAS*, 372, 21

Asada, K., Kameno, S., Shen, Z.-Q., Horiuchi, S., Gabuzda, D. C., & Inoue, M. 2006, *PASJ*, 58, 261

Asada, K., & Nakamura, M. 2012, *ApJL*, 745, L28

Asada, K., Nakamura, M., Doi, A., Nagai, H., & Inoue, M. 2014, *ApJL*, 781, L2

Bach, U. 2004, PhD thesis, Rheinischen Friedrich-Wilhelms-Universität Bonn

Bach, U., Krichbaum, T. P., Alef, W., Witzel, A., & Zensus, J. A. 2002, in Proceedings of the 6th EVN Symposium, ed. E. Ros, R. W. Porcas, A. P. Lobanov, & J. A. Zensus, 155

Baczko, A.-K., et al. 2016, *A&A*, 593, A47

Balmaverde, B., Baldi, R. D., & Capetti, A. 2008, *A&A*, 486, 119

Bartel, N., Sorathia, B., Bietenholz, M. F., Carilli, C. L., & Diamond, P. 1995, Proceedings of the National Academy of Science, 92, 11371

Bettoni, D., Falomo, R., Fasano, G., & Govoni, F. 2003, *A&A*, 399, 869

Biretta, J. A., Sparks, W. B., & Macchetto, F. 1999, *ApJ*, 520, 621

Birkinshaw, M., & Davies, R. L. 1985, *ApJ*, 291, 32

Black, A. R. S., Baum, S. A., Leahy, J. P., Perley, R. A., Riley, J. M., & Scheuer, P. A. G. 1992, *MNRAS*, 256, 186

Blandford, R. D., & Königl, A. 1979, *ApJ*, 232, 34

Blandford, R. D., & Rees, M. J. 1974, *MNRAS*, 169, 395

Blandford, R. D., & Znajek, R. L. 1977, *MNRAS*, 179, 433

Boccardi, B., Krichbaum, T. P., Bach, U., Bremer, M., & Zensus, J. A. 2016a, *A&A*, 588, L9

Boccardi, B., Krichbaum, T. P., Bach, U., Mertens, F., Ros, E., Alef, W., & Zensus, J. A. 2016b, *A&A*, 585, A33

Bondi, H. 1952, *MNRAS*, 112, 195

Bower, G. C., Goss, W. M., Falcke, H., Backer, D. C., & Lithwick, Y. 2006, *ApJL*, 648, L127

Carilli, C. L., Bartel, N., & Linfield, R. P. 1991, *AJ*, 102, 1691

Carilli, C. L., & Barthel, P. D. 1996, *A&A Rev.*, 7, 1

Chatterjee, R., et al. 2011, *ApJ*, 734, 43

Chon, G., Böhringer, H., Krause, M., & Trümper, J. 2012, *A&A*, 545, L3

Claussen, M. J., Diamond, P. J., Braatz, J. A., Wilson, A. S., & Henkel, C. 1998, *ApJL*, 500, L129

Denicoló, G., Terlevich, R., Terlevich, E., Forbes, D. A., Terlevich, A., & Carrasco, L. 2005, *MNRAS*, 356, 1440

Doeleman, S. S., Weintroub, J., Rogers, A. E. E., et al. 2008, *Nature*, 455, 78

Fanaroff, B. L., & Riley, J. M. 1974, *MNRAS*, 167, 31P

Ferrarese, L., Ford, H. C., & Jaffe, W. 1996, *ApJ*, 470, 444

Ferrarese, L., & Ford, H. C. 1999, *ApJ*, 515, 583

Fomalont, E. B. 1999, in Astronomical Society of the Pacific Conference Series, Vol. 180, Synthesis Imaging in Radio Astronomy II, ed. G. B. Taylor, C. L. Carilli, & R. A. Perley, 301

Fujita, Y., Kawakatu, N., & Shlosman, I. 2016, *PASJ*, 68, 26

Gebhardt, K., & Thomas, J. 2009, *ApJ*, 700, 1690

Ghisellini, G., Padovani, P., Celotti, A., & Maraschi, L. 1993, *ApJ*, 407, 65

Ghisellini, G., Tavecchio, F., & Chiaberge, M. 2005, *A&A*, 432, 401

Ghisellini, G., Tavecchio, F., Maraschi, L., Celotti, A., & Sbarrato, T. 2014, *Nature*, 515, 376

Hada, K., Doi, A., Kino, M., Nagai, H., Hagiwara, Y., & Kawaguchi, N. 2011, *Nature*, 477, 185

Hada, K., et al. 2013, *ApJ*, 775, 70

—. 2017, *PASJ*, 69, 71

Haga, T., Doi, A., Murata, Y., Sudou, H., Kameno, S., & Hada, K. 2015, *ApJ*, 807, 15

Heyvaerts, J., & Norman, C. 1989, *ApJ*, 347, 1055

Hirabayashi, H., et al. 2000, *PASJ*, 52, 955

Hofmann, F., Sanders, J. S., Nandra, K., Clerc, N., & Gaspari, M. 2016, *A&A*, 585, A130

Homan, D. C., Lister, M. L., Kovalev, Y. Y., Pushkarev, A. B., Savolainen, T., Kellermann, K. I., Richards, J. L., & Ros, E. 2015, *ApJ*, 798, 134

Inoue, Y., & Tanaka, Y. T. 2016, *ApJ*, 828, 13

Inoue, Y., Doi, A., Tanaka, Y. T., Sikora, M., & Madejski, G. M. 2017, *ApJ*, 840, 46

Isobe, N., & Koyama, S. 2015, *PASJ*, 67, 77

Jones, D. L., Wehrle, A. E., Meier, D. L., & Piner, B. G. 2000, *ApJ*, 534, 165

Jones, D. L., Wrobel, J. M., & Shaffer, D. B. 1984, *ApJ*, 276, 480

Kadler, M., Ros, E., Lobanov, A. P., Falcke, H., & Zensus, J. A. 2004, *A&A*, 426, 481

Kameno, S., Nakai, N., Sawada-Satoh, S., Sato, N., & Haba, A. 2005, *ApJ*, 620, 145

Kameno, S., Inoue, M., Wajima, K., Sawada-Satoh, S., & Shen, Z.-Q. 2003, *PASA*, 20, 134

Kameno, S., Sawada-Satoh, S., Inoue, M., Shen, Z.-Q., & Wajima, K. 2001, *PASJ*, 53, 169

Kolokythas, K., O'Sullivan, E., Giacintucci, S., et al. 2015, *MNRAS*, 450, 1732

Komissarov, S. S., Vlahakis, N., Königl, A., & Barkov, M. V. 2009, *MNRAS*, 394, 1182

Konigl, A. 1981, *ApJ*, 243, 700

Kovalev, Y. Y., Lobanov, A. P., Pushkarev, A. B., & Zensus, J. A. 2008, *A&A*, 483, 759

Krichbaum, T. P., Alef, W., Witzel, A., Zensus, J. A., Booth, R. S., Greve, A., & Rogers, A. E. E. 1998, *A&A*, 329, 873

Leahy, J. P., Black, A. R. S., Dennett-Thorpe, J., Hardcastle, M. J., Komissarov, S., Perley, R. A., Riley, J. M., & Scheuer, P. A. G. 1997, *MNRAS*, 291, 20

Lister, M. L., Aller, M. F., Aller, H. D., et al. 2013, *AJ*, 146, 120

Lazio, T. J. W., & Cordes, J. M. 1998, *ApJ*, 505, 715

Lobanov, A. P. 1998, *A&A*, 330, 79

—. 2005, ArXiv Astrophysics e-prints

Macchetto, F., Marconi, A., Axon, D. J., et al. 1997, *ApJ*, 489, 579

McKinney, J. C. 2006, *MNRAS*, 368, 1561

Mertens, F., Lobanov, A. P., Walker, R. C., & Hardee, P. E. 2016, *A&A*, 595, A54

Meyer, E. T., Sparks, W. B., Biretta, J. A., Anderson, J., Sohn, S. T., van der Marel, R. P., Norman, C., & Nakamura, M. 2013, *ApJL*, 774, L21

Nagai, H., et al. 2014, *ApJ*, 785, 53

Nakahara, S., Doi, A., Murata, Y., Hada, K., Nakamura, M., & Asada, K. 2016, Galaxies, 4, 80

—. in press, *ApJ*

Nakahara, S., Doi, A., Murata, Y., Nakamura, M., Hada, K., & Asada, K. in submitted, *ApJ*

Nakamura, M., & Asada, K. 2013, *ApJ*, 775, 118

O'Dea, C. P. 1998, *PASP*, 110, 493

O'Sullivan, E., Giacintucci, S., David, L. P., Gitti, M., Vrtilek, J. M., Raychaudhury, S., & Ponman, T. J. 2011, *ApJ*, 735, 11

Owen, F. N., Ledlow, M. J., Morrison, G. E., & Hill, J. M. 1997, *ApJL*, 488, L15

Pacholczyk, A. G. 1970, Radio astrophysics. Nonthermal processes in galactic and extragalactic sources

Perley, R. A., Dreher, J. W., & Cowan, J. J. 1984, *ApJL*, 285, L35

Perlman, E. S., et al. 2011, *ApJ*, 743, 119

Piner, B. G., Jones, D. L., & Wehrle, A. E. 2001, *AJ*, 122, 2954

Pjanka, P., Zdziarski, A. A., & Sikora, M. 2017, *MNRAS*, 465, 3506

Reynolds, C. S., & Fabian, A. C. 1996, *MNRAS*, 278, 479

Rybicki, G. B., & Lightman, A. P. 1979, Radiative processes in astrophysics (New York, Wiley-Interscience)

Sawada-Satoh, S., Kameno, S., Nakamura, K., Namikawa, D., Shibata, K. M., & Inoue, M. 2008, *ApJ*, 680, 191

Schneider, D. P., et al. 2010, *AJ*, 139, 2360

Smith, D. A., Wilson, A. S., Arnaud, K. A., Terashima, Y., & Young, A. J. 2002, *ApJ*, 565, 195

Sol, H., Pelletier, G., & Asseo, E. 1989, *MNRAS*, 237, 411

Steenbrugge, K. C., & Blundell, K. M. 2008, *MNRAS*, 388, 1457

Sudou, H., Taniguchi, Y., Ohyama, Y., Kameno, S., Sawada-Satoh, S., Inoue, M., Kaburaki, O., & Sasao, T. 2000, *PASJ*, 52, 989

Suzuki, K., et al. 2012, *ApJ*, 746, 140

Tadhunter, C., Marconi, A., Axon, D., Wills, K., Robinson, T. G., & Jackson, N. 2003, *MNRAS*, 342, 861

Tonry, J. L., Blakeslee, J. P., Ajhar, E. A., & Dressler, A. 2000, *ApJ*, 530, 625

Tseng, C.-Y., Asada, K., Nakamura, M., Pu, H.-Y., Algaba, J.-C., & Lo, W.-P. 2016, *ApJ*, 833, 288

Vermeulen, R. C., Ros, E., Kellermann, K. I., et al. 2003, *A&A*, 401, 113

Walker, R. C., Dhawan, V., Romney, J. D., Kellermann, K. I., & Vermeulen, R. C. 2000, *ApJ*, 530, 233

Walsh, J. L., Barth, A. J., Ho, L. C., & Sarzi, M. 2013, *ApJ*, 770, 86

Wang, C.-C., & Zhou, H.-Y. 2009, *MNRAS*, 395, 301

Woo, J.-H., & Urry, C. M. 2002, *ApJ*, 579, 530

Wrobel, J. M., & Heeschen, D. S. 1984, *ApJ*, 287, 41